

**HIGH THERMAL
CONDUCTIVITY CATALYSTS
FOR THE CO-WGS
PROCESS INTENSIFICATION**

Domenico Pisano



Unione Europea



*Ministero dell'Istruzione,
dell'Università e della Ricerca*



UNIVERSITÀ DEGLI
STUDI DI SALERNO

FONDO SOCIALE EUROPEO
Programma Operativo Nazionale 2000/2006
“Ricerca Scientifica, Sviluppo Tecnologico, Alta Formazione”
Regioni dell’Obiettivo 1 – Misura III.4
“Formazione superiore ed universitaria”

Department of Chemical and Food Engineering

*Ph.D. Course in Chemical Engineering
(IV Cycle-New Series)*

**HIGH THERMAL CONDUCTIVITY
CATALYSTS FOR THE CO-WGS
PROCESS INTENSIFICATION**

Supervisor

Prof. Vincenzo Palma

Ph.D. student

Domenico Pisano

Scientific Referees

Prof. Enrico Tronconi

Prof. Gianpiero Groppi

Ph.D. Course Coordinator

Prof. Paolo Ciambelli

List of papers on International Journals

- Palma V., Pisano D., Martino M., Ricca A., Ciambelli P., **Comparative Studies of Low Temperature Water Gas Shift Reaction over Platinum Based Catalysts**, *Chemical Engineering Transaction* 39 (2014), 31-36.
- Palma V., Pisano D., Martino M., Ricca A., Ciambelli P., **Catalysts for the intensification of the Water Gas Shift process**, *Springer Proceedings in Energy*, 112-117.
- Palma V., Pisano D., Martino M., Ricca A., Ciambelli P., **High thermal conductivity structured carriers for catalytic processes intensification**, *Chemical Engineering Transaction* 43 (2015), 47-52.

Summary

INDEX OF TABLES XV

ABSTRACT.....XVII

CHAPTER I. INTRODUCTION: PROCESS

INTENSIFICATION IN HYDROGEN PRODUCTION.

THE USE OF THE STRUCTURED CATALYSTS 1

I.1 Fuel Cells2

I.1.1 Proton Exchange Membrane Fuel Cells3

I.2 Hydrogen production.....4

I.2.1 Water Gas Shift.....5

I.2.1.1 HTS catalyst..... 6

I.2.1.2 LTS catalyst 6

I.2.2 Limitations of the Water Gas Shift process6

***I.3 The process intensification of the Water Gas Shift:
an improvement of the catalytic phase7***

***I.3.1 High thermal conductivity structured catalysts for
the Water Gas Shift process intensification.....8***

CHAPTER II. STATE OF THE ART..... 11

II.1 Conventional catalyst for LT-WGS.....11

II.1.1 New catalysts for LT-WGS.....12

II.2 Active species.....12

II.2.1 Noble metals.....12

II.2.2 Non noble metals.....16

II.3 Chemical support17

II.4 Structured carrier.....20

<i>II.5 Washcoat formulation</i>	<i>25</i>
CHAPTER III. STRUCTURED CARRIERS: HEAT TRANSFER STUDY. EXPERIMENTAL	29
<i>III.1 Structured carriers properties.....</i>	<i>29</i>
<i>III.2 Heat transfer tests</i>	<i>29</i>
<i>III.3 Modeling of the system</i>	<i>30</i>
CHAPTER IV. CATALYTIC POWDERS: EXPERIMENTAL	33
<i>IV.1 Preparation of the catalysts in powder form</i>	<i>33</i>
<i>IV.1.1 Impregnation.....</i>	<i>34</i>
<i>IV.1. 2 Calcination</i>	<i>34</i>
<i>IV.2 Characterization of the catalysts in powder form .</i>	<i>35</i>
<i>IV.2.1 Thermo Gravimetric Analysis and Mass Spectrometry (TG-MS)</i>	<i>35</i>
<i>IV.2.2 XRD powder diffraction.....</i>	<i>37</i>
<i>IV.2.2.1 Bragg's Law</i>	<i>39</i>
<i>IV.2.2.2 Scherrer's Equation.....</i>	<i>41</i>
<i>IV.2.3 Determination of the specific surface area (SSA)</i>	<i>43</i>
<i>IV.2.4 Electron Microscopy.....</i>	<i>46</i>
<i>IV.2.4.1 Electron matter interactions</i>	<i>47</i>
<i>IV.2.4.2 Electrons exploited in Transmission Electron Microscopy (TEM).....</i>	<i>49</i>
<i>IV.2.6 Temperature Programmed Reduction (TPR)</i>	<i>50</i>
<i>IV.2.7 Raman Spectroscopy.....</i>	<i>51</i>
<i>IV.3 Water Gas Shift (WGS) tests</i>	<i>57</i>
<i>IV.3.1 Activity and Selectivity tests</i>	<i>57</i>
<i>IV.4 Laboratory plant used for the activity tests</i>	<i>58</i>

IV.4.1 Feed section	58
IV.4.2 Reaction section	59
IV.4.2.1 Electrical oven.....	59
IV.4.2.2 Stainless steel tubular reactor.....	61
IV.4.3 Analysis section.....	61
IV.5 Tests made on the more active catalyst.....	62
CHAPTER V. HEAT TRANSFER TESTS: CHOICE OF THE BEST STRUCTURED CARRIER	65
V.1 Heat transfer tests results: thermal profiles	65
V.2 Mathematical Model.....	67
CHAPTER VI. CHOICE OF THE CATALYTIC PHASE: CHARACTERIZATION AND WGS TESTS RESULTS	73
VI.1 Characterization results.....	73
VI.1.1 Specific surface area (SSA).....	73
VI.1.2 X-Ray Diffraction (XRD)	74
VI.1.3 Raman spectra.....	77
VI.1.4 Temperature Programmed Reduction (TPR) results	79
VI.2 Initial screening: WGS activity and selectivity tests	82
VI.3 1%Pt/CeO ₂ -ZrO ₂ : performances by increasing space velocity (GHSV test) and preliminary stability test.	86
CHAPTER VII. DEPOSITION OF THE ACTIVE PHASES ON THE STRUCTURED CARRIER, CHARACTERIZATION AND TESTS ON THE STRUCTURED CATALYSTS.....	89

VII.1 Preparation of the Washcoat.....	89
VII.1.1 Formulation of the Washcoat.....	91
VII.1.2 Characterization of the Ce-Zr washcoat.....	92
VII.2 WGS test on the Ce-Zr washcoat in powder form, catalyzed with platinum	93
VII.3 Formulation, characterization and testing of the new Alumina covered ceria washcoat.....	95
VII.4 Preparation of the structured catalyst.....	96
VII.5 Samples characterization.....	97
VII.5.1 Investigation on the washcoat deposition	98
VII.5.2 Characterization of the catalysts.....	100
VII.6 Water Gas Shift activity tests: comparison between powder and structured catalyst.....	103
VII.7 Stability of the structured foam catalyst	106
VII.8 Influence of the structured carrier on the performances of the WGS process in a “quasi-adiabatic” system	108
VII.8.1 Development of the “quasi-adiabatic” system	108
VII.8.2 WGS reaction in the “quasi-adiabatic” system: influence of the foams and foams density comparison	109
VII.9 Study on the influence of the foam geometry on the backdiffusion of the heat of reaction.....	110
VII.9.1 Activity and selectivity tests on aluminum foams with constant density and different porosity	110

<i>VII.9.2 WGS reaction in the “quasi-adiabatic” system: influence of the geometric parameters (porosity) of the foams</i>	<i>112</i>
CHAPTER VIII. CFD MODELING OF THE WGS ADIABATIC SYSTEM.....	117
<i>VIII.1 Modeling of the system: CAD and geometry</i>	<i>118</i>
<i>VIII.2 Fluid-dynamic modeling</i>	<i>120</i>
<i>VIII.3 Finite element modeling of the adiabatic reactor</i>	<i>122</i>
<i>VIII.3.1 Modeling of the adiabatic reactor: powder catalyst results.....</i>	<i>125</i>
<i>VIII.3.2 Modeling of the adiabatic reactor: structured foam catalyst results</i>	<i>128</i>
<i>VIII.4 Validation of the adiabatic reactor model: Parametric Sweep.....</i>	<i>131</i>
<i>VIII.5 Comparison between the performances of the two reactor systems in view of a process intensification</i>	<i>132</i>
CHAPTER IX. CONCLUSIONS.....	137

Index of Figures

<i>Figure 1 Main fuels and applications of Fuel Cells (EU Commission, 2003).....</i>	<i>2</i>
<i>Figure 2 Operating of a Proton Exchange Membrane Fuel Cell (Institution Smithsonian, 2008)</i>	<i>4</i>
<i>Figure 3 Deactivation test of the a) Pt/CeO₂ sol-gel, b) Au/CeO₂ coprecipitation, and c) Au/Fe₂O₃ (Luengnaruemitchai A., 2003).....</i>	<i>14</i>
<i>Figure 4 CO conversion over the noble metal catalysts and commercial HTS catalysts (Lim S., 2009)</i>	<i>15</i>
<i>Figure 5 Water-gas-shift reactivity over several ceria-based catalysts (Li Y., 2000).....</i>	<i>16</i>
<i>Figure 6 The importance of cerium oxide for WGS process (Buitrago R., 2012)</i>	<i>19</i>
<i>Figure 7 Dispersions of one phase into a second one. Each phase can be in one of the three states of matter (Banhart J., 2001).....</i>	<i>21</i>
<i>Figure 8 Pore structure of aluminium foamed by adding TiH₂ (Banhart J., 2001).....</i>	<i>21</i>
<i>Figure 9 Mechanic structure made by metallic foam (Banhart J., 2001).....</i>	<i>22</i>
<i>Figure 10 Sh vs Re_{max} logarithmic plot. Overall correlation of mass-transfer data for ceramic and metallic foams. The solid line represents (Groppi G., 2007).....</i>	<i>24</i>
<i>Figure 11 SEM image of the SiC/Al₂O₃ based foam support (Palma V., 2009)</i>	<i>24</i>
<i>Figure 12 Particle size distribution of the catalyst powders for washcoating: as supplied (dash-dotted line); after 3 h of milling in nitric acid (pH) 5; dashed line); after 3 h of milling in citric acid (pH) 4; dotted line); and after 3 h of milling in citric acid (pH) 6; continuous line). (González-Velasco J. R., 2003)</i>	<i>25</i>

<i>Figure 13 Schematic representation of the heat exchange model</i>	<i>31</i>
<i>Figure 14 Gas (a) and solid (b) phase balance detailed scheme.....</i>	<i>31</i>
<i>Figure 15 TG and DTG curves</i>	<i>37</i>
<i>Figure 16 Geometry for interference of a wave scattered from two planes separated by a spacing, d. The dashed lines are parallel to the crests or troughs of the incident and diffracted wavefronts. The important path length difference for the two rays is the sum of the two dark segments.....</i>	<i>39</i>
<i>Figure 17 Diffraction plate of XRD</i>	<i>42</i>
<i>Figure 18 Typically XRD spectrum.....</i>	<i>43</i>
<i>Figure 19 Signals generated when a high-energy beam of electrons interacts with a thin specimen.....</i>	<i>48</i>
<i>Figure 20 General scheme of a) SEM and b) TEM instrumentations</i>	<i>48</i>
<i>Figure 21 Generalized description of the three main imaging modes in TEM.....</i>	<i>50</i>
<i>Figure 22 Curve Concentration-Temperature-Time obtained by a TPR</i>	<i>50</i>
<i>Figure 23 The electromagnetic spectrum on the wavelength scale in meters</i>	<i>53</i>
<i>Figure 24 Diagram of the Rayleigh and Raman scattering processes. The lowest energy vibrational state m is shown at the foot with states of increasing energy above it. Both the low energy (upward arrows) and the scattered energy (downward arrows) have much larger energies than the energy of a vibration.....</i>	<i>54</i>
<i>Figure 25 Stokes and anti-Stokes scattering for cyclohexane. To show the weak anti- Stokes spectrum, the y-axis has been extended in the inset</i>	<i>54</i>
<i>Figure 26 Infrared and Raman spectra of benzoic acid. The top trace is infrared absorption given in % transmission (%T) so that the lower</i>	

the transmission value the greater the absorption. The lower trace is Raman scattering and the higher the peak the greater the scattering 56

Figure 27 Experimental set-up..... 58

Figure 28 Oven used in experimental set-up..... 59

Figure 29 Temperature profile along the empty reactor..... 60

Figure 30 Reacting system 61

Figure 31 Mass spectrometer..... 62

Figure 32 Solid temperature (operating conditions: $T_{oven} = 200^{\circ}\text{C}$, $Q_{tot} = 2.4 \text{ l/min}$)..... 65

Figure 33 Gas temperature (operating conditions: $T_{oven} = 400^{\circ}\text{C}$, $Q_{tot} = 2.4 \text{ l/min}$)..... 66

Figure 34 ERG Duocel foam, model optimization (operating conditions: $T_{oven} = 200^{\circ}\text{C}$, $Q_{tot} = 1.2 \text{ l/min}$)..... 68

Figure 35 ERG Duocel foam, model optimization (operating conditions: $T_{oven} = 200^{\circ}\text{C}$, $Q_{tot} = 2.4 \text{ l/min}$)..... 68

Figure 36 ERG Duocel foam, model optimization (operating conditions: $T_{oven} = 200^{\circ}\text{C}$, $Q_{tot} = 3.6 \text{ l/min}$)..... 69

Figure 37 ERG Duocel foam, model optimization (operating conditions: $T_{oven} = 400^{\circ}\text{C}$, $Q_{tot} = 1.2 \text{ l/min}$)..... 69

Figure 38 ERG Duocel foam, model optimization (operating conditions: $T_{oven} = 400^{\circ}\text{C}$, $Q_{tot} = 2.4 \text{ l/min}$)..... 70

Figure 39 ERG Duocel foam, model optimization (operating conditions: $T_{oven} = 400^{\circ}\text{C}$, $Q_{tot} = 3.6 \text{ l/min}$)..... 70

Figure 40 ERG Duocel foam, thermal conductivity coefficient (k) and gas phase heat transfer coefficient (h_g) as function of oven temperature..... 71

<i>Figure 41 ERG Duocel foam, thermal conductivity coefficient (k) and gas phase heat transfer coefficient (hg) as function of volumetric gas flow rate</i>	<i>71</i>
<i>Figure 42 Estimated model parameters, comparison between the foam samples.....</i>	<i>72</i>
<i>Figure 43 SSA (m²/g) as fuction of CeO₂ amount.....</i>	<i>74</i>
<i>Figure 44 Diffraction spectrum of 1%Pt/CeO₂ sample</i>	<i>75</i>
<i>Figure 45 Diffraction spectrum of 1%Pt/CeO₂-ZrO₂ sample</i>	<i>75</i>
<i>Figure 46 Diffraction spectrum of CeO₂ and CeO₂-ZrO₂ sample.....</i>	<i>76</i>
<i>Figure 47 Raman spectrum of 1%Pt/CeO₂ sample.....</i>	<i>77</i>
<i>Figure 48 Raman spectrum of CeO₂-ZrO₂ sample</i>	<i>78</i>
<i>Figure 49 Raman spectrum of 1%Pt/14%CeO₂/γAl₂O₃ sample.....</i>	<i>79</i>
<i>Figure 50 Raman spectrum of 1%Pt/CeO₂-ZrO₂ sample.....</i>	<i>79</i>
<i>Figure 51 TPR profile of 1%Pt/CeO₂-ZrO₂ sample.....</i>	<i>80</i>
<i>Figure 52 Magnitude of peak obtained from the deconvolution elaboration</i>	<i>81</i>
<i>Figure 53 Comparison between the platinum reduction peak of the three catalysts (a: PtCeZr; b: PtCe; c: Pt14CeAl).....</i>	<i>82</i>
<i>Figure 54 WGS tests: dry molar composition at the outlet of the reactor for 1%Pt/CeO₂ catalyst</i>	<i>83</i>
<i>Figure 55 WGS tests: dry molar composition at the outlet of the reactor for 1%Pt/CeO₂-ZrO₂</i>	<i>83</i>
<i>Figure 56 Composition of methane at the outlet of the reactor for 1%Pt/CeO₂-ZrO₂.....</i>	<i>84</i>
<i>Figure 57 WGS tests: dry molar composition at the outlet of the reactor for 1%Pt/14%CeO₂/Al₂O₃ catalyst.....</i>	<i>84</i>

<i>Figure 58 Comparison between the three investigated samples in terms of CO conversion as function of temperature.....</i>	85
<i>Figure 59 Effect of space velocity on PtCeZr catalyst</i>	87
<i>Figure 60 Stability test on PtCeZr (80 hours).....</i>	88
<i>Figure 61 Experimental result obtaining using platinum chloride as precursor</i>	90
<i>Figure 62 Aluminum foam after dipping in platinum chloride solution</i>	90
<i>Figure 63 Experimental result obtaining using amino platinum nitrate as precursor.....</i>	91
<i>Figure 64 Dip-coating procedure.....</i>	92
<i>Figure 65 Mechanical stability of Ce-Zr washcoat on aluminum foam</i>	92
<i>Figure 66 Activity and selectivity tests of 1%Pt/CeZr as function of reactor temperature.....</i>	94
<i>Figure 67 TPR profile of 1%Pt/CeO₂-ZrO₂ washcoat</i>	94
<i>Figure 68 Comparison of activity and selectivity tests of 1%Pt/CeZr washcoat and 1%Pt/20%CeO₂ Alumina washcoat as function of reactor temperature.....</i>	96
<i>Figure 69 Imaging from optical microscopy of the alumina washcoat</i>	98
<i>Figure 70 Washcoat weight loss after ultrasonic treatment: behavior during time.....</i>	99
<i>Figure 71 SEM of the structured washcoated sample. Magnitude: 28X</i>	99
<i>Figure 72 SEM/EDX of the structured catalyst. In red, the mapping of the Alumina washcoat, in yellow the Ceria support and in light blue the Platinum.....</i>	100

<i>Figure 73 XRD pattern of the powder samples, obtained by the washcoat precursors (pseudoboehmite and γ-Alumina), followed by the washcoat, ceria/washcoat and 1% Pt/ceria/washcoat (fresh and exhausted) catalysts</i>	102
<i>Figure 74 Raman shift of the 20%CeO₂/Al₂O₃ and 1%Pt/20%CeO₂/Al₂O₃ samples</i>	103
<i>Figure 75 WGS activity of the structured catalyst (aluminum foam: 40 PPI, rel. dens.: 6-8%). Temperature dependence of molar fraction of the components (based on a dry mixture). CO inlet molar concentration: 8 %; H₂O/CO ratio: 3.75; N₂ balance; WHSV = 1.2 h⁻¹</i>	104
<i>Figure 76 Influence of the Aluminum foam (40 PPI, rel. dens.: 6-8%) on the CO conversion. CO inlet molar concentration: 8 %; H₂O/CO ratio: 3.75; N₂ balance; WHSV = 1.2 h⁻¹</i>	105
<i>Figure 77 Stability test on the W.Ce/Pt (s) structured catalyst: experimental data and mathematical elaboration</i>	106
<i>Figure 78 X-Ray Diffraction of the exhausted structured catalyst, compared to the fresh catalyst.</i>	108
<i>Figure 79 CO conversion versus temperature; comparison between W.Ce/ Pt(p), W.Ce/Pt(s) and W.Ce/Pt(s+). Nearly adiabatic conditions (reactor diameter, D: 0.17 m; L/D: 5.2; CO molar concentration at the reactor inlet: 8%; water / CO ratio: 3.75; N₂ balance; linear flow velocity: 18.2 cm * s⁻¹; gas inlet temperature: 259°C).</i>	109
<i>Figure 80 Activity and selectivity tests on aluminum foams with constant density and different porosity</i>	111
<i>Figure 81 WGS activity of the structured catalyst (aluminum foam: 40 PPI, rel. dens.: 10-12%). Temperature dependence of molar fraction of the components (based on a dry mixture). CO inlet molar concentration: 8 %; H₂O/CO ratio: 3.75; N₂ balance; WHSV = 1.2 h⁻¹</i>	112

<i>Figure 82 CO conversion versus temperature; comparison between 40 PPI, 20 PPI and 10 PPI foams. Relative density: 10-12% for all foams.....</i>	<i>113</i>
<i>Figure 83 Unit cell for the circular intersection (Bhattacharya A., 2002).....</i>	<i>114</i>
<i>Figure 84 Simplified geometry of the real system</i>	<i>119</i>
<i>Figure 85 Fluid dynamics simulation (FREE AND POROUS MEDIA FLOW).....</i>	<i>121</i>
<i>Figure 86 Fluid dynamics simulation couple of hollow cylinders before and after the porous domain</i>	<i>122</i>
<i>Figure 87 Simplified geometry for modelling the adiabatic system. 123</i>	
<i>Figure 88 Mass balance 2D simulation, with regards to the CO (powder catalyst).....</i>	<i>126</i>
<i>Figure 89 powder catalyst simulation: hydrogen concentration</i>	<i>127</i>
<i>Figure 90 Surface plot of temperature: simulation of the powder catalyst.....</i>	<i>127</i>
<i>Figure 91 Temperature profile: simulation of the powder catalyst . 128</i>	
<i>Figure 92 CO molar fraction inside the foam (2D plot)</i>	<i>128</i>
<i>Figure 93 Aluminum foam effect: redistribution of the heat flux.....</i>	<i>129</i>
<i>Figure 94 temperature profile: inner and foam section.....</i>	<i>129</i>
<i>Figure 95 Comparison between the conductivity flux of the catalysts in powder form and structured on foam</i>	<i>130</i>
<i>Figure 96 CO conversion along the foam length with different inlet CO molar fraction (inlet $T=473K$).....</i>	<i>131</i>
<i>Figure 97 Temperature profile along the axial coordinate with different inlet temperature ($y_{COin}=0.08$).....</i>	<i>132</i>

<i>Figure 98 COMSOL simulation: comparison between foam and powder ($T_{in} = 200^{\circ}\text{C}$; contact time: 214 ms).....</i>	<i>133</i>
<i>Figure 99 COMSOL simulation: comparison between foam and powder ($T_{in} = 200^{\circ}\text{C}$; contact time: 107 ms).....</i>	<i>133</i>
<i>Figure 100 COMSOL simulation: comparison between foam and powder ($T_{in} = 220^{\circ}\text{C}$; contact time: 214 ms).....</i>	<i>134</i>
<i>Figure 101 COMSOL simulation: comparison between foam and powder ($T_{in} = 220^{\circ}\text{C}$; contact time: 107 ms).....</i>	<i>134</i>

Index of Tables

<i>Table 1 Geometric Properties of the Ceramic Foam and of Metallic Foams (Groppi G., 2007).....</i>	<i>23</i>
<i>Table 2 TiO₂ Washcoat Stability without Binders after Ultrasonic Vibration (uv), Thermal Shock (ts), and Abrasion (a)a (González Carlos A., 2007)</i>	<i>26</i>
<i>Table 3 Effect of Binders on TiO₂ and Pd/TiO₂ Washcoat Stability after Ultrasonic Vibration (uv), Thermal Shock (ts), and Abrasion (a)a (González Carlos A., 2007).....</i>	<i>26</i>
<i>Table 4 Composition and geometric properties of the foams.....</i>	<i>29</i>
<i>Table 5 Heat transfer tests: operating conditions.....</i>	<i>30</i>
<i>Table 6 Scanned Masses.....</i>	<i>62</i>
<i>Table 7 Parametric optimization of the heat transfer model (volumetric flow rate: 2.4 Ndm³/min).....</i>	<i>67</i>
<i>Table 8 Catalysts characterization: EDXRF Pt content, Specific Surface Area, average crystallites size, TPR H₂ uptake.....</i>	<i>73</i>
<i>Table 9 Crystallite size from Scherrer equation.....</i>	<i>76</i>
<i>Table 10 Main peak of TPR profile</i>	<i>80</i>
<i>Table 11 Hydrogen uptake experimentally measured.....</i>	<i>81</i>
<i>Table 12 BET characterization</i>	<i>93</i>
<i>Table 13 Nominal loadings and the specific surface areas of the samples</i>	<i>101</i>
<i>Table 14 Crystallites size from Scherrer equation.....</i>	<i>102</i>
<i>Table 15 Mainly geometrical parameter of metal foam.....</i>	<i>114</i>
<i>Table 16 Foams thermal conductivity</i>	<i>115</i>

Table 17 Diffusion coefficients magnitude of the reactants and products of the WGS reaction 126

Abstract

Today, the increasingly serious lack of resources and the obsolescence of the plants present on the whole planet led to develop new ways that go beyond “traditional” chemical engineering. The research is now focusing on novel equipment and techniques that potentially could change the concept of chemical plants and lead to compact, safe, energy-efficient, and environment-friendly sustainable processes. These developments share a common focus on “process intensification” — an approach that has truly emerged in the past few years as a special and interesting discipline of chemical engineering, because of the reasons enounced above.

Process intensification tends its aim to the reduction of the total costs (fixed and operating) in an industrial plant. This “saving” in economic terms is possible not only by making a minimization of the equipment’s volume, but it’s also related to both chemical and physical aspects of an industrial process.

The main targets of a process intensification are:

1. Improved control of reactor kinetics giving higher selectivity/reduced waste products.
2. Higher energy efficiency.
3. Equipment compactness
4. Reduced capital costs.
5. Reduced inventory/improved intrinsic safety/fast response times.

In order to reach all of these targets, it must be considered that transport phenomena play a very important role for the process intensification of an industrial reactor. Also improvements in environmental impact is another aspect that is constantly faced today, regarding all the processes in which there is the need of eliminating a dangerous chemical species. Among the others, a possible candidate for process intensification is represented by the CO Water Gas Shift process (WGS). It is the first purification stage of a hydrogen production plant, and involves the conversion of CO in CO₂, while at the same time there is an increase in H₂ yield in syngas. Moreover, the WGS increases also the CO₂ concentration in the gas phase, making easier

Abstract

its separation in the CO₂ adsorption unit, and providing a H₂/N₂ mixtures with the appropriate ratio for the production of an important chemical product, such as ammonia.

The WGS is an exothermic reaction, thermodynamically favored at low temperature, however kinetic limitations make it convenient to work with a two-stage process, i.e. two different catalytic systems: a first stage (HTS), carried out in the temperature range 350-500°C, where the most of the CO conversion is obtained (but thermodynamic limitations effect the theoretically reachable conversion); a second stage (LTS) carried out in the temperature range of 180-300°C, with slow kinetics (the thermodynamic conditions allow to obtain very low CO concentration, less than 10 ppm).

Although this type of configuration is very effective, it shows several disadvantages: as a first, the global system kinetics is very slow, requiring a high catalyst volume, that in turn results in long activation time; moreover, the presence of the inter-cooling unit increases not only the energy requirements of the process, but also the plant cost itself; furthermore, the LTS catalyst shows pyrophoricity, resulting not able to sustain frequent start up and shut down stages, and then not suitable for mobile fuel cell applications.

Definitely, the actual WGS plant configuration would be of course the biggest unity of an integrated fuel processor. For these reasons, a process intensification is needed. Considering a conventional adiabatic reactor, the exothermicity and the equilibrium characteristics of the WGS reaction, together with the catalysts performances, reflects negatively on the CO conversion, lowering the reaction rate at the inlet of the catalytic bed, where the temperature is low, and limiting the very high conversion values at the outlet, where the temperature is high. So, a process intensification for this type of reaction should account for a modification both of the catalytic phase and the catalyst bed thermal profile. In order to reach the first target, it is necessary to find a good catalytic formulation that is able to be efficient in the low temperature range. Moreover, by considering the influence of the heat transport on the whole system, the use of a high conductive catalyst could play a crucial role, with the possibility of redistributing the heat of reaction along the catalytic bed to obtain a flatter thermal profile with a lower outlet temperature and, consequently, a higher CO conversion.

The aim of this PhD thesis was to investigate the influence of the catalyst thermal properties on the Water Gas Shift (WGS) process, by using a structured carrier with high thermal conductivity. The research line was followed in order to verify if it is possible to increase the backdiffusion of the reaction heat throughout the structured catalyst bed, modifying the temperature profile, obtaining, with respect to a typical packed bed adiabatic reactor, a higher temperature at the inlet section and a lowered temperature at the outlet bed section, overcoming respectively, the kinetic and thermodynamic limits, achieving so an increased CO conversion.

Accordingly, this approach would ensure that a conventional double staged WGS reactors with intermediate heat exchange could be replaced with a single WGS reactor, characterized by a "quasi isothermal" temperature profile.

In this context, during the PhD project different phases have been followed to reach the intended objective.

1. CHOICE OF THE STRUCTURED CARRIER

In order to reach the desired heat transfer properties, metal foams were chosen as structured carriers. They are open-cell structures that may be fabricated in a variety of shapes from a wide range of materials, and they exhibit very high porosities with good interconnectivity. These characteristics result in a lower pressure drop than that observed with packed beds and high convection in the tortuous pores, which, in turn, enhances mass and heat transfer. Moreover, they may be also easily coated with high-surface-area catalytic components, using specific procedures and techniques.

In general, in addition to the intrinsic bulk thermal conductivity of the selected material, two main parameters can influence the overall heat transfer coefficient of the structured carrier: the void fraction (or porosity) and the pore density (PPI). In particular, the void fraction is related to the amount of solid material and the pore density to the three-dimensional structure of the catalyst carrier. Moreover, it is important to keep in mind that for a catalytic process also the pressure drops must be limited, so highly porous foams may help to control this parameter.

In order to find an efficient open cell foam for the purposes of this PhD project, the heat transfer through different structured metal foams was investigated. The thermal properties, in particular the thermal conductivity and the gas phase heat transfer coefficient of the structured supports were estimated by means of a mathematical model, developed on the basis of heat transfer models accounted for honeycomb monoliths. An experimental set up was built, including an oven for heating the whole system at different temperatures, a quartz tube in which the metal foam was inserted, and a set of thermocouples to measure temperature along the carrier. The experimental results were used to optimize the mathematical model and validate it, and the thermal properties estimated were used as basis for a comparison between the carriers and the choice of the best one in terms of heat transfer.

2. CHOICE OF THE CATALYTIC PHASES

The literature research revealed that reducible oxides supported platinum based catalysts are today the best choice for obtaining a highly active and efficient catalytic system for the WGS reaction. These types of catalysts, instead of gold ones, are more stable and, if high dispersed on a reducible oxide, can prevent phenomena such as sintering of the active metal particles.

Abstract

On the basis of this review, different platinum based catalysts, supported on ceria, ceria-zirconia and ceria-alumina were prepared, through the wet impregnation method, followed by drying at 120°C and calcination in muffle. A wide characterization of the samples was done, including the specific surface area estimation (BET method), the XRF and XRD analysis, the use of the Raman shift and the study on the reducibility properties of the samples, through the technique of the temperature programmed reduction (TPR). The Water Gas Shift tests were made by fixing the operative conditions, in order to have a benchmark for this initial screening. The CO concentration was set to 5%, water at 25% and helium balance, as inert component. These activity and selectivity tests were made at atmospheric pressure, in a range of temperature between 150°C and 400°C, with a gas hourly space velocity of 5000 h⁻¹. All the samples were reduced to particles with a size between 180 and 355 nm. The aim of this experimental campaign was to find a good and efficient catalytic formulation, active in a very low temperature range.

The best catalyst, from those investigated, was also tested by increasing the space velocity of one order of magnitude and by verifying its durability, in order to investigate about possible critical issue to be corrected.

3. DEPOSITION OF THE CATALYTIC PHASES ON THE STRUCTURED CARRIER

In order to anchor the catalytic phases to the structured carrier, it is necessary to formulate a good washcoat. A washcoat is a chemical support precursor that in catalysis is used to disperse the active metals over a wide surface area. Washcoat materials must form a rough and porous surface, which greatly increases the surface area compared to the smooth surface of the bare structured carrier. This in turn maximizes the catalytically active surface available to the reactants.

So, the washcoat was formulated on the basis of what enounced above. The catalyst preparation was divided into three stages. All these stages were followed by drying at 120°C and calcination at 450°C for 3 hours. Firstly, the washcoat was anchored to the foam surface by using the dip-coating procedure. Then, chemical support was added to the washcoat by the wet impregnation method. Finally, the sample was impregnated with a solution of the platinum precursor. The same catalyst formulation was also prepared in powder form, and employed as reference. The stability of the washcoat on the foam surface was tested via sonication, to verify the adhesion of the chemical species on the structured support. The specific surface area (SSA) was determined by the BET method. The Scanning Electron Microscope (SEM) was used to study the morphology of the foams and to check the washcoat distribution on the surface of the foam. It was possible to estimate the pores average diameter and the fibers diameter, and it was also verified that the washcoating procedure led to a homogeneous deposition on the

surface of the structured carrier. The temperature programmed reduction (TPR) was performed in a stainless steel tube with an internal diameter of 22 mm. A 5% H₂/N₂ gas mixture (flow rate: 1000 Ncm³/min) was fed to the reactor, and temperature was raised up to 400°C with a heating rate of 10°C/min. The WGS catalytic tests were performed at atmospheric pressure, in typical conditions for the LTS process (a temperature range of 200-400°C). The reacting mixture consisted of 8% CO, 30% H₂O and N₂ balance. The catalysts activity was tested in the same reactor as the TPR. The gas hourly space velocity (GHSV) was set up to 10000 h⁻¹.

4. DEVELOPMENT OF A “QUASI” ADIABATIC SYSTEM: COMPARISON BETWEEN PACKED BED AND STRUCTURED FOAM CATALYST

An important phase of the PhD was dedicated to the development of a “quasi” adiabatic system, in order to exploit the high thermal conduction of the structured catalyst, prepared in the previous phase, with respect to a conventional packed bed catalyst.

In order to evaluate the influence of the thermal transport properties of the foams on the WGS reaction, a laboratory system able to limit the thermal dispersions was set up. This target was reached by increasing the total flow rate, keeping constant the L/D ratio of the structured foam catalyst. The experimental set up was used to drive a WGS reaction in the following conditions: inlet T = 260 °C, P = 1 atm, CO molar fraction = 8 vol%, H₂O molar fraction = 30 vol%, N₂ balance, WHSV = 2.4 gCO/gcat/h, linear flow velocity = 18.2 cm/s. In order to compare the performances of the different samples, two thermocouples were installed, one at the inlet section of the catalyst and the other one at the outlet section, while the CO conversion was continuously monitored with the aid of an ABB-NDIR specific analyzer.

After making a comparison between the performances of a foam catalyst with those of a packed bed catalyst, the developed experimental set up was used to perform different WGS tests on different types of foam. The aim of these tests was to investigate how the void fraction and the pore density can influence the heat transfer, and so the performances of the structured catalysts.

5. MODELING OF THE WGS ADIABATIC REACTOR

In order to validate the results obtained by the tests made with the “quasi” adiabatic system, the model of the adiabatic reactor was developed with the aid of the finite element software COMSOL Multiphysics 5.0 (License number: No.13073437,00-0f-fe-0a-73-34). The comparison has been done between the structured foam catalyst and a conventional packed bed adiabatic reactor. The process has been modeled coupling transport phenomena and reaction kinetics. The reactor model was implemented exclusively with the CFD.

Abstract

A simplified geometry of the real system was built. By assuming no dependence of the transport parameters with the tangential coordinate, it was possible to reduce the volume domain to $\frac{1}{4}$ of the real one. In particular, the simulated geometry was built as follows. The gas stream flows axially, along the z-coordinate, through the reactor (internal diameter of 22 mm, thickness of 2.5 mm). The catalytic zone was put in the middle of the reactor (catalyst diameter of 16.5 mm). The length of the catalytic zone was set to 88 mm, while the total length of the reactor was 400 mm.

The use of COMSOL confirmed what obtained from the experimental results, by demonstrating that, inside the structured catalyst, there is a backdiffusion of the heat of reaction with a more efficient catalyst that is able to achieve higher CO conversion; in particular, by operating in specific conditions ($T_{in} = 220^{\circ}\text{C}$) it is possible to lower the adiabatic ΔT from 80°C and a CO conversion of 88% (powder case) to an adiabatic “quasi isothermal” ΔT of only 8°C with a CO conversion of 99% (structured catalyst case). These results exploit the high thermal properties of the structured foam catalyst in view of an intensification of the Water Gas Shift process.

The developed model will be the basis for the design of an industrial reactor, where the catalyzed structured foam technology may be applied.

Chapter I. Introduction: process intensification in hydrogen production. The use of the structured catalysts

Nowadays, energy security is a major issue. Fossil fuels, particularly crude oil, is confined to a few areas of the world and its supply is governed by political, economic and social factors. These factors cooperate to force volatile, often high fuel prices while, at the same time, environmental policy is demanding a reduction in greenhouse gases and toxic emissions.

So, all these topics, together with others such as the depletion of fossil fuels in the next years, encourage the research towards other energy models, both renewable and sustainable. Many renewable energy sources have been proposed during this last 20 years, like solar and wind energy, but they could not be a good solution because linked to specific, alternating and unstable sites.

In this scenario, hydrogen arises as an energy vector that can fulfil all the requirements (EU Commission, 2003) It is considered the least pollutant fuel, because its combustion generates substantially water vapor, and, in some circumstances, only small quantities of NO_x (Sun J., 2004). In addition, hydrogen has the highest energy content per mass unit: in fact, the yield in terms of energy is 122 kJ/g, more than 2.75 times higher than any other fuel.

To make good use of hydrogen, the large-scale production of this substance is essential (Barreto L, 2003). It is mainly used as a raw material in the chemical industry, such as in the production of ammonia and in methanol synthesis, as well as in many refinery processes. It is also widely used as a transport fuel in the so called "hydrogen cars", which allow to have a zero emissions vehicle (Koniczny A, 2008) furthermore, it can also be used in fuel cells (Fuel Cells, FCS) for the production of electricity in stationary or mobile applications (Levin D.B., 2004). On a sociological viewpoint, hydrogen and fuel cells could meet, in a unique way, people's concerns about security of energy supply and problems related to climate

change, bringing to a new conceptual idea in respect of energy production all over the world.

I.1 Fuel Cells

Due to the increasing attention towards the emissions from the internal combustion engines, fuel cell (FC) technology is now standing out as a “clean” alternative to decrease the automotive pollution. FC are currently undergoing rapid development both for stationary and mobile applications. In particular, fuel cells could replace the internal combustion engines in cars, trucks, buses, etc. while meeting the most stringent emission regulations. In the same way, they may be used for power generation in stationary industrial or domestic applications. In Figure 1 all possible fuel cell’s applications, together with fuels employed, are summarized.

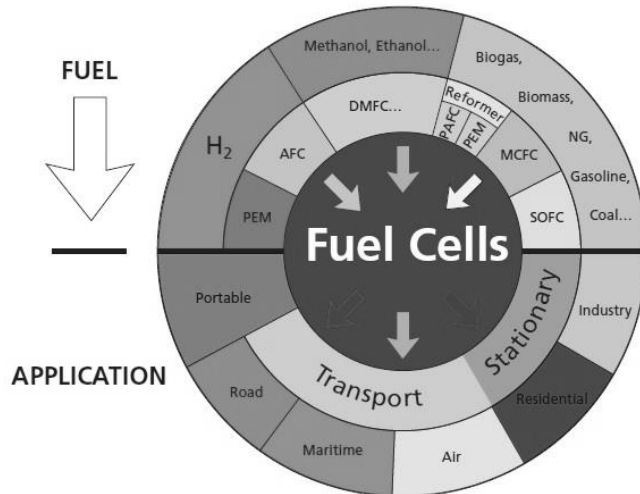


Figure 1 Main fuels and applications of Fuel Cells (EU Commission, 2003)

In fuel cells, in place of a combustion, an electrochemical process occurs, in which, by combining hydrogen and oxygen, water, electricity and heat are generated at the same time. For this reason, it is possible to achieve a higher energy conversion efficiency than conventional engines combustion, since there are no limitations of Carnot's theorem (de la Piscina P.R., 2008 and Li Y., 2000). Other benefits are the extreme variety of installed power (from a few kW to about 100 MW) and the minimum noise during the operation (Ni M., 2007) .

Fuel cells are different from batteries, in that they require a constant source of fuel and oxygen/air to sustain the chemical reaction; however, fuel cells can produce electricity continually for as long as these inputs are supplied. Briefly, fuel cell consists of an electrolyte and two electrodes; the latter is oxidized at the anode while an oxidant (oxygen from the air) is

simultaneously reduced at the cathode (Vaidya D., 2006). Every fuel cell also has an electrolyte, which carries electrically charged particles from one electrode to the other, and a catalyst, which speeds the reactions at the electrodes. The electrolyte plays a key role. It must permit only the appropriate ions to pass between the anode and cathode. If free electrons or other substances could travel through the electrolyte, they would disrupt the chemical reaction. As the main difference among fuel cell types is the electrolyte, fuel cells are classified by the type of electrolyte they use. We distinguish:

- AFCs (Alkaline Fuel Cells);
- MCFCs (Molten Carbonate Fuel Cells);
- SOFCs (Solid Oxide Fuel Cells);
- PAFCs (Phosphoric Acid Fuel Cells);
- PEMFCs (Proton Exchange Membrane Fuel Cells).

In the majority of current applications, Proton Exchange Membrane Fuel Cell (PEMFC) technology is employed.

1.1.1 Proton Exchange Membrane Fuel Cells

The proton exchange membrane FC (PEM-FC) is today considered one of the most suitable technology for mobile and automotive application, due to its high power density, mechanical robustness, low weight, compactness, long stack life, fast start-up, dynamic response characteristics (Galletti C., 2009). In the archetypical hydrogen–oxide proton exchange membrane fuel cell design, a proton-conducting polymer membrane (the electrolyte) separates the anode and cathode sides (Dupuis A.C., 2011). This was called a "solid polymer electrolyte fuel cell" (SPEFC) in the early 1970s, before the proton exchange mechanism was well-understood.

On the anode side, hydrogen diffuses to the anode catalyst where it later dissociates into protons and electrons. These protons often react with oxidants causing them to become what are commonly referred to as multi-facilitated proton membranes. The protons are conducted through the membrane to the cathode, but the electrons are forced to travel in an external circuit (supplying power) because the membrane is electrically insulating. On the cathode catalyst, oxygen molecules react with the electrons (which have traveled through the external circuit) and protons to form water.

In addition to this pure hydrogen type, there are hydrocarbon fuels for fuel cells, including diesel, methanol and chemical hydrides. The waste products with these types of fuel are carbon dioxide and water. In Figure 2 there is a schematic explanation of how a PEM-FC works.

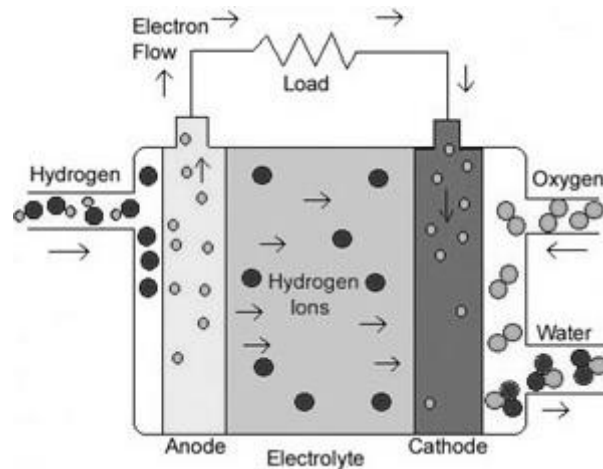


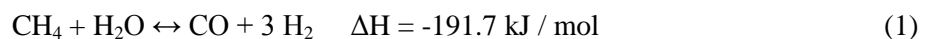
Figure 2 Operating of a Proton Exchange Membrane Fuel Cell (Institution Smithsonian, 2008)

I.2 Hydrogen production

Hydrogen is the ideal fuel for PEM Fuel Cells, because it offers some advantages: low operating temperature (so, low energy consumption), high current density, satisfactory efficiency and truly “zero emissions” (Ghenciu A.F., 2002). Although hydrogen is the most abundant element on the Earth, it cannot be found as a single element, and it is necessary to synthesize it from H₂-containing compounds. Fuel processing is the most convenient method of supplying hydrogen in the absence of a suitable infrastructure for hydrogen.

The current world production of hydrogen amounts to 5.1011 Nm³ per year (Kapdan I.K., 2006). Today, the cheapest way to produce it is by using oil or other fossil fuels. In fact, approximately 97% of hydrogen is obtained from fossil fuels, while only 3% is obtained by electrolysis of water (Kotay S. M., 2008). The main methods for producing hydrogen are: water electrolysis, coal gasification, partial oxidation reactions (PO) and steam reforming (SR) (Balat M., 2008).

In conventional plants, hydrogen is produced by steam reforming of methane and other hydrocarbons. The reforming of natural gas provides more than 50% of hydrogen (Chen Z., 2004). It consists in reacting methane (CH₄) and steam (H₂O) at a temperature in the range 700-1100°C, to produce syngas (a mixture essentially consisting of carbon monoxide, carbon dioxide and hydrogen), according to the reaction:



The heat required to activate the reaction is generally provided burning part of the methane. The reaction is favored at low pressures, however,

sometimes it is performed at high pressure (20 atm), since H₂ becomes a more marketable product. The produced mixture is known as synthesis gas, often used directly for the production of methanol, ammonia and other related compounds.

Hydrogen can also be produced through the auto-thermal reforming reaction (ATR), a reaction that combines the features of SR and PO. In this case the feedstock is mixed with oxygen and steam with very well defined O₂ and Steam to Carbon ratios. At the reactor inlet section, partial combustion reactions take place, followed by methane steam reforming reaction and shift conversion to equilibrium over the catalyst bed. In the section of the reactor in which partial oxidation reaction takes place, the temperature is about 1200°C. The operating pressures vary in the range 20-60 atm. The hydrogen yield is higher than the partial oxidation and lower than steam reforming, but this system does not require a hot source for providing heat (Moharana M.K., 2011) because the overall reaction is exothermic, resulting in high outlet temperatures, typically higher than 950°C.

So, after the reforming stage the gas stream is composed mainly by carbon monoxide, hydrogen and unreacted steam. However, the carbon monoxide formed by the reforming reaction needs to be completely converted both because it poisons the platinum electrodes, worsening the fuel-cell performances, both because it is more convenient to convert CO to CO₂ and H₂ in the Water gas shift (WGS) reactor, and then easily eliminate CO₂.

1.2.1 Water Gas Shift

The water-gas shift (WGS) reaction is a reversible, exothermic reaction in which carbon monoxide reacts with steam to produce hydrogen and carbon dioxide:



So, it not only reduces the CO concentration, (Luengnaruemitchai A., 2003) but simultaneously increases the H₂ concentration.

This reaction is most favored if in large excess of steam. Furthermore, since the reaction is exothermic, the formation of the products is favored at low temperatures, while the balance is shifted toward the reactants at high temperatures. However, even if the equilibrium favors the formation of the products at low temperature, the kinetics is faster at high temperatures.

Since at high temperatures CO conversion is limited by the thermodynamic equilibrium, while at low temperatures the system is limited by the intrinsic lower reaction rate, normally two steps of WGS are industrially used: at high temperature HT-WGS step followed by a low temperature LT-WGS one.

Chapter I

The initial HTS takes advantage of the high reaction rates, but is thermodynamically limited, which results in incomplete conversion of carbon monoxide with a 2-4% vol. of CO concentration at the reactor outlet. To shift the equilibrium toward hydrogen production, a subsequent low temperature shift reactor is employed to produce a carbon monoxide exit composition of less than 1% (Navarro R.M., 2007). The transition from the HTS to the LTS reactors necessitates an intermediate cooling stage. Due to the different reaction conditions, different catalysts must be employed at each stage to ensure optimal activity. The commercial HTS catalyst is the iron oxide–chromium oxide catalyst and the LTS catalyst is a copper-based catalyst (Callaghan C.A., 2006). This necessitates the removal of the sulphur compounds prior to the LTS reactor by a guard bed in order to protect the copper catalyst. Conversely, the iron used in the HTS reaction is generally more robust and resistant toward poisoning by sulphur compounds. While both the HTS and LTS catalysts are commercially available, their specific composition varies based on vendor.

1.2.1.1 HTS catalyst

The typical composition of commercial HTS catalyst has been reported as 74.2% Fe₂O₃, 10.0% Cr₂O₃, 0.2% MgO (remaining percentage attributed to volatile components) (Newsome D. S., 1980). The chromium acts to stabilize the iron oxide and prevents sintering. The operation of HTS catalysts occurs within the temperature range of 310°C to 450°C. The temperature increases along the length of the reactor due to the exothermic nature of the reaction. As such, the inlet temperature is maintained at 350°C to prevent the exit temperature from exceeding 550°C. Industrial reactors operate at a range from atmospheric pressure to 8375 kPa.

1.2.1.2 LTS catalyst

The typical composition of commercial LTS catalyst has been reported as 32-33% CuO, 34-53% ZnO, 15-33% Al₂O₃ (Callaghan C.A., 2006). The active catalytic species is CuO. The function of ZnO is to provide structural support as well as prevent the poisoning of copper by sulphur. The Al₂O₃ prevents dispersion and pellet shrinkage. The LTS shift reactor operates at a range of 200°C to 250°C. Low reaction temperatures must be maintained due to the susceptibility of copper to thermal sintering. These lower temperatures also reduce the occurrence of side reactions that are observed in the case of the HTS.

1.2.2 Limitations of the Water Gas Shift process

Currently, the Water Gas Shift is a two-stage process that exploits the excellent kinetics in the HTS and a favorable thermodynamic equilibrium at

LTS stage; however, the use of two different catalytic systems, the need of two separate reactors or two separate zone of the reactor, and above the others the need for an intercooling, make it the ideal candidate to a massive intensification. The exothermicity of the WGS reflects negatively on the conversion rate of the CO, limiting the reaction rate at the inlet of the catalytic bed, where the temperature is low, and disfavoring the approach to the thermodynamic equilibrium at the outlet, where the temperature is high.

I.3 The process intensification of the Water Gas Shift: an improvement of the catalytic phase

Process intensification is conceived as a way to optimize fixed and operating costs in an industrial plant. It is not only related to a reduction of the size of equipment, but also to the change of the production method, by enhancing both chemical that physical aspects of the process.

The strategy of the process intensification was conceived in the late 1970's as a philosophy of capital development, with the aim of achieving a cost savings; the idea was that if a reduction of the plant size does not compromise the output performance, a significant reduction in the costs of the plant would have occurred (Reay D., 2008). Nowadays the process intensification is related not only to the design of equipment of significantly reduced size but, more specifically, to the change of production methods which allow a better control of the kinetics of the reactors, improvements in activity and selectivity, improvements in energy efficiency, improvements in safety and environmental impact. More in general the process intensification strategy can be divided into two main areas, the process intensifying equipment and the process intensifying methods, the first one deals with the design of new reactors configurations for what concerns the mixing and the heat and mass transfer (Palma V., 2009), the second deals with the integration of reactions, separations, heat exchanges or phase transitions and new process-control methods (Pouransani N., 2014). In this context, the best example of a process that would benefit most from an intensification is, of course, the Water Gas Shift. Up to now, the Water Gas Shift is a two-stage process that exploits the excellent kinetics in the HTS and a favorable thermodynamic equilibrium at LTS stage; however, the use of two different catalytic systems, the need of two separate reactors or two separate zone of the reactor, and above the others the need for an intercooling, make it the ideal candidate to a massive intensification. The exothermicity of the WGS reflects negatively on the conversion rate of the CO, limiting the reaction rate at the inlet of the catalytic bed, where the temperature is low, and disfavoring the approach to the thermodynamic equilibrium at the outlet, where the temperature is high. From previous paragraph considerations, it is clear that the process intensification has to be targeted to a modification of

Chapter I

the thermal profile along the catalytic bed. This could be done by enhancing the heat conduction along the catalytic bed, which would improve the overall reaction rate, by allowing a flat temperature profile and a better approach to the equilibrium composition with a single catalytic bed. In this context, the thermal conductivity of the catalytic materials plays a crucial role: the required catalyst should show not only high activity and selectivity but also high thermal stability and conductivity, low pressure drop and enhanced heat transfer (Palma V., 2009). An interesting alternative to the traditional catalysts is represented by structured ones; in this case it is possible to exploit both the thermal conductivity of a metal structures such as open cell foams and the activity of a catalytic formulation in powder form, by coupling the two parts by means of a coating.

1.3.1 High thermal conductivity structured catalysts for the Water

Gas Shift process intensification

Structured catalysts are composed of three components:

- Structured Carrier;
- Washcoat: porous material layer deposited on the structured carrier, which act as chemical support for the active element;
- Active Catalytic Species.

The structured carrier and the washcoat must possess high thermal and mechanical stability and ensure a high dispersion of the active species, preventing any sintering phenomena.

The structured catalysts are generally prepared from structured carriers as honeycomb monoliths and open cells foams, both of ceramic material that metal. They are also very flexible, because they allow easy passage of scale.

Structured catalysts are not widely used in catalysis. Their main application is in reduction of gaseous pollutants coming out from motor vehicles and stationary sources. Actually, they could be used also in many other fields of catalysis, to multiply the types of reactions of industrial interest. In particular, using them in low temperature water gas shift reaction, taking advantage from their ability to influence heat and mass transfer (especially if they are highly conductive), can lead to really improved performances in terms of CO conversion.

This PhD is included in a national project, called PRIN. In the frame of the project the research unit UNISA will study innovative structured catalysts for process intensification of CO purification stage by water gas shift reaction. To this purpose several very interesting structured supports such as honeycomb monoliths, open cells foams, and knitted wires, can be used.

In particular, new structured catalysts will be developed which, through synergic actions aiming to a heat redistribution along the catalytic bed, such

as the use of supports with high thermal conductivity and a different gas flow geometry across the catalytic bed, allow to achieve a flattening of the temperature profile that corresponds to a greatly improved overall performance of the CO conversion stage. Indeed it is worth to note that though nowadays it is well known the fundamental role of material and heat transfer properties in controlling the investigated catalytic process performances, there is a lack of knowledge in the literature, in particular for the most innovative structures, such as open cells foams. Thus, it is necessary to carry out a fundamental study aiming to the development of engineering correlations for the modelling and optimization of the structured catalysts design and reactor performances improvement.

On the basis of the literature review on heat transfer in foams monoliths, it was highlighted that two parameters effect on overall heat transfer coefficient: the void fraction (or porosity) and the pore density (PPI), in addition to the bulk thermal conductivity, of course. The effect of pore density on heat transfer coefficient seems to be conflicting in several papers, since in some cases it increases with pore density, in other cases it decreases. Some predicting expressions reported the dependence of Nusselt number from pore density (PPI), and underlined that it in a first range it quickly increased with PPI value, in the second range the increasing is less evident (Bartolomew C.H., 2006) The special trend, that define a “critical PPI value”, is more evident for foam samples with higher diameters (> 0.010 m). A predictive expression of foam thermal conductivity was proposed by Bhattacharia et al .(Bhattacharya A., 2002), in which the effective thermal conductivity of foam samples was evaluated.

The planned activity includes the analysis of the heat transfer in the structured supports, the preparation and characterization of specific innovative catalysts for the water gas shift reaction, the deposition of these catalysts on the most promising structured supports. Furthermore, catalytic activity preliminary tests for prepared catalytic systems will be carried out.

Chapter II. State of the art

II.1 Conventional catalyst for LT-WGS

A conventional catalyst for LT-WGS is based on copper oxide and zinc oxide supported on alumina. Copper has always been very active in LTS; the problem was related to sintering phenomena, but its use with ZnO supported on Alumina allowed to obtain a very active and stable catalyst. The main problems linked with the conventional LTS catalyst are the sulphide and chloride presences. Due to these two substances, within 6-12 months the catalyst completely deactivates, and the deactivation starts even at the beginning of the operations.

The preparation of LTS catalyst plays an important role for the activity of the final catalyst, mainly the nature of the mixture of precursors and its evolution during the preparation steps. Uchida et al. (Uchida H., 1967) have tested different combinations of catalysts prepared by co-precipitation with hydroxides, carbonates and hydroxy-carbonates as precursors, and assessing their activity and stability. The maximum activity is obtained for a ratio Cu/Zn equal to 0.4 and the method of preparation is very important. Copper is the real active species as compared with zinc. Petrini et al. (Petrini G., 1983) have noted that the most active catalysts can be prepared by adding aluminum hydroxide during the precipitation of copper and zinc. They thus revealed that the reaction rate depends strongly on the content of metallic copper and that the dispersion of the metallic copper and the catalytic activity depend on the amount of hydrotalcite present in the precipitate (the higher the hydrotalcite, the more active is the catalyst).

It has already disclaimed that in LTS catalyst the sintering of the copper grains may occur. Usually, the sintering takes place when the catalyst is heated up to a temperature higher than 300°C. The alumina tends to slow this phenomenon. Between 250 and 300°C, the small clusters combine to give agglomerates on the support. So, we can assume that the main active sites of the catalyst are attributable to the small copper crystals.

II.1.1 New catalysts for LT-WGS

As it has been already disclaimed, the conventional LTS catalyst has got two main problems: it is pyrophoric, i.e. it doesn't withstand continuous start-up and shut down, as occurs in mobile applications such as PEM-FC, and it is not resistant to chloride and sulfide, which are poisons. So, it is desirable to find a LTS catalyst that allows to overcome these problems. Moreover, another important issue for the future is the development of a single stage LT-WGS. So, it is another crucial point to pursue.

During the last years there have been many researches on this topic, trying to develop a new low temperature water gas shift catalyst. In particular, many active species, such as noble metals (but also non-noble metals) and many kinds of supports have been tested. Here a brief state of the art on LTS catalysts is reported.

II.2 Active species

II.2.1 Noble metals

Platinum, gold and other precious metals have long been studied. They have a high activity in WGS below 250°C. Metals have been studied such as platinum, rhodium, ruthenium, gold and palladium on partially reducible oxides such as ceria, zirconia, titania. The reaction rate for these catalysts is near zero order for CO, and this is an advantage for conducting the reaction to equilibrium using the minimum amount of catalyst, if compared with the standard catalyst for LTS. Basinska et al. (Basinska A., 2006) compared the activity of a series of noble metals (Pt, Rh, Ru, Pd and Ir) supported on Fe₂O₃; they noticed that the presence of a noble metal promoted the support reduction at low temperatures, bringing to a higher activity. Among the others, Rh and especially Ru were the most active species with iron oxides as support.

Panagiotopoulou et al. (Panagiotopoulou P., 2006) saw that the activity of these catalysts depends strongly on the interaction between the active species and the support. According to them platinum catalysts are generally more active than Ru, Rh, and Pd, and exhibit significantly higher activity when supported on "reducible" rather than on "irreducible" oxides. When noble metals are dispersed on "reducible" oxides, such as CeO₂ and TiO₂, the apparent activation energy of the reaction does not depend on the nature of the metallic phase but only on the nature of the support. In contrast, E_a differs from one metal to another when supported on an irreducible oxide, such as Al₂O₃, indicating that a different reaction mechanism is operable.

The presence of a noble metal, especially when supported on a reducible metal oxide, such as ceria, is very important for the activity of the catalyst. This was demonstrated by Hilaire et al. (Hilaire S., 2004), who measured

WGS reaction rate on Pd/ceria, Ni/ceria, Fe/ceria, Co/ceria and Pd/silica. Pd and Ni showed the highest activities, and Pd/ceria was much more active than Pd/silica, demonstrating a cooperative effect between palladium and ceria, which is very important also in the reaction mechanism, due to its reducibility.

Sometimes the addition of another active species can give a positive effect. This was investigated by Sato et al. (Sato Y., 2006), who studied the addition of Re on supported titania catalysts Pt, Pd and Ir based. They observed different manners of enhancement effect: the formation of bimetallic surface clusters in the case of Pt and Pd and anchoring of nanoparticles by highly dispersed Re in the case of Ir. The enhancement effect was accepted as an acceleration of the WGS reaction velocity via a faster activation of water.

One of the most active noble metals for water gas shift is gold. Fu et al. (Fu Q., 2003) prepared, characterized and tested a gold based supported ceria catalyst with various Au loadings. They established that gold/ceria is active for the shift in the range 150-350°C. Its activity at low temperatures was explained by the improvement of the OSC of ceria, making easier the water adsorption and re-oxidation of support. However, they observed that in order to carry this action, gold crystallites had to be very small (nm). But the catalytic activity of gold catalysts depends not only on the dispersion of gold nanoparticles, but also on the state and the structure of the support. About this, Tabakova et al. (Tabakova T., 2000) that gold catalysts on well crystallized supports have a higher catalytic activity in comparison with the samples on amorphous supports, principally due to a reduction in pore volume. In particular, they established that the best supports were ferric oxide and zirconia.

The big problem of gold catalysts for WGS is that the crystals can easily undergo sintering phenomena during the reaction, making a deactivation of the catalyst. This was studied by Andreeva et al. (Andreeva D., 2007), on a gold/ceria catalyst. They observed that the addition of alumina as a co-support gives a more stable catalyst, because sintering is inhibited, but simultaneously there is a slight decrease in activity.

Boaro et al. (Boaro M., 2009) compared the performances of Pt based and Au based catalysts on zirconia, with a nominal active species loading of 4%. They concluded that under these conditions the gold based catalyst is more active. Furthermore, they assert that the support play a secondary role and the main reason for activity is the dimension of metal crystallites.

Another comparison between gold and platinum was made by Luengnaruemitchai et al. (Luengnaruemitchai A., 2003), who found that 1%Pt/CeO₂ was more active than gold based catalysts, especially when the feed ratio is increased. Moreover, catalytic activity and stability tests showed that activity of the gold-containing catalysts was decreasing during the

Chapter II

catalytic tests, while the platinum based catalysts remained more stable (Figure 3).

A Pt/TiO₂ catalyst was studied by Iida et al. (Iida H., 2003); they investigated the influence of the platinum precursor on the activity of the catalyst. As a result, it was found that the Pt/TiO₂ catalysts prepared from H₂PtCl₆*6H₂O and Pt(C₅H₇O₂)₂ had relatively high catalytic activities.

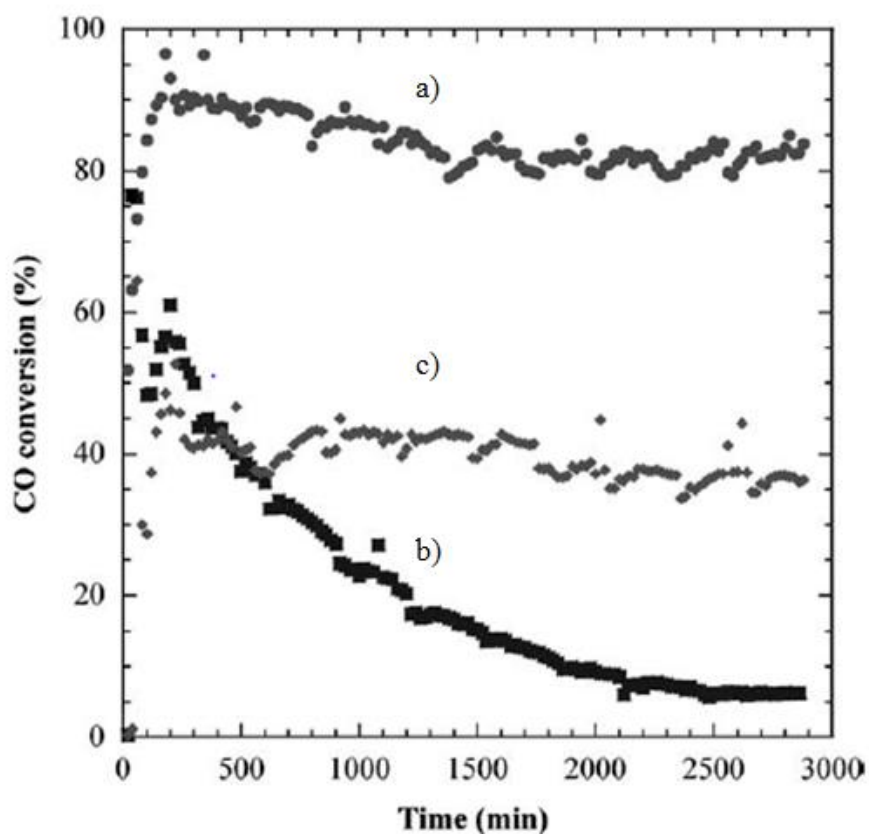


Figure 3 Deactivation test of the a) Pt/CeO₂ sol-gel, b) Au/CeO₂ coprecipitation, and c) Au/Fe₂O₃ (Luengnaruemitchai A., 2003)

Furthermore, it was found that there was a linear relationship between catalytic activity and Pt dispersion.

The pyrophoricity of a platinum based catalyst was studied by Kam et al. (Kam R., 2010) comparing it with the conventional LTS catalyst. No pyrophoricity was observed for any of the Pt-based catalysts; however, sintering of the metallic phase in Pt/TiO₂ and Pt/ZrO₂ persisted, leading to a decrease in activity. In contrast, Pt/CeO₂ was the only catalyst which retained its activity, displaying no loss in specific surface area or metal dispersion.

Lim et al. (Lim S., 2009) studied a ceria/zirconia supported platinum catalyst, varying the platinum loading. They found that even for 1% of platinum loading there is a very high level of activity (Figure 4). They also study the mechanism of the shift reaction, calculating an effectiveness factor and speculating an egg-shell morphology of the catalyst.

About the reaction mechanism, in one view C–H bond breaking of the formate has been proposed to be the rate-limiting step of the low temperature water-gas shift. This step could be fastened by the incorporation of a promoter into the catalyst.

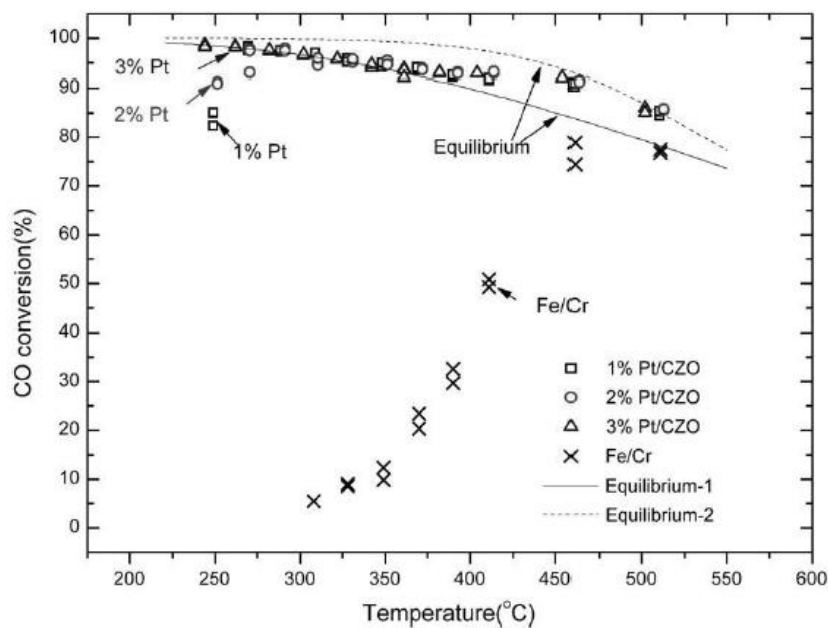


Figure 4 CO conversion over the noble metal catalysts and commercial HTS catalysts (Lim S., 2009)

This was studied by Pigos et al. (Pigos J. M., 2007), who suggested the use of sodium as a promoter to enhance the reaction rate; they verify their hypothesis by characterization with DRIFTS, and saw that sodium produced a weakness of the C–H bonds of the formate on the surface of the catalyst, and so, made the mechanism faster.

One of the main problem related to the application of noble metals as active species of a LTS catalyst is deactivation of the catalyst. In most of the cases this is due to sintering of metal crystals. One way to avoid this is by an appropriate preparation method. Wang et al. (Wang Y., 2012) prepared a silica encapsulating platinum for a core shell. They observed the poor activity of this catalyst, and investigated the addition of alkali metals as promoters, such as sodium. In conclusion, they obtained a good active

Chapter II

catalyst with also a very good stability. The problem of this result could just be the preparation method, which is very very difficult.

Xu et al. (Xu W., 2012) examined three catalysts platinum and ruthenium based, evaluating the benefits eventually deriving from a Pt/Ru alloy. All the catalysts tested displayed a good WGS activity, but the Pt/Ru alloy catalyst revealed a better selectivity to hydrogen than the only Ru based one. Moreover, a substantial amount of formate was formed during the reaction in the monometallic catalysts, but this is not the case in the alloy catalyst, revealing that formate is only a spectator in these types of catalysts.

II.2.2 Non noble metals

As noble metals have the main problem of being expensive, there are in literature also many works about water gas shift using non-noble metal based catalysts. Obviously, the active species loading in these catalysts can be greater than noble metal based ones, for two reasons: the first is the one already disclaimed, and the other is that non-noble metal catalysts are generally less active than noble metal ones. So, this is a crucial point. The most non-noble metal based catalysts studied for water gas shift are: nickel, cobalt, iron and copper.

Li et al. (Li Y., 2000) reported a study on the activity of a Cu-Ni catalyst on ceria, with La as dopant. Both Cu and Ni increased the reducibility of ceria. The authors recorded an improved activity of the catalyst adding copper and nickel, and they also study the reaction kinetics, obtaining very low activation energies (Figure 5).

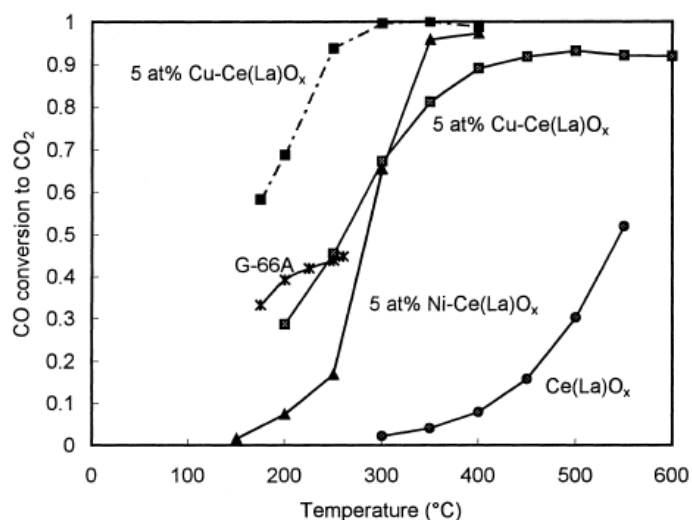


Figure 5 Water-gas-shift reactivity over several ceria-based catalysts (Li Y., 2000)

A problem to deal with in the WGS is to suppress methanation reaction. Lin et al. (Lin J.-H., 2010) prepared a bimetallic catalyst copper and nickel based and characterized it with XRD, TPR and other conventional techniques. They found that there was a formation of a solid solution between copper and nickel, and this brought to an improved activity of the catalyst with respect to a normal bimetallic catalyst. Moreover, they also stated that the presence of copper avoid the methanation reaction, while nickel is the main responsible for the activation of the shift reaction.

Another important active species for the WGS is iron, often used in combination with copper. Bao et al. (Bao Z., 2012) prepared catalysts with different Fe/Cu molar ratios and evaluated their activity in a hydrogen rich atmosphere. The results suggested that the optimal Fe/Cu ratio of the catalyst was 1:1, while an excess in copper results in lower activity. They concluded that copper not only acts as an active role for the WGS, but it also conducts as an electronic promoter at higher temperatures.

Knapp et al. (Knapp R., 2010) studied a catalyst based on Cu nanoparticles on alumina, coated with a thin film of 1-butyl-2,3-dimethylimidazolium trifluoromethane sulfonate (BDiMIm). They found that catalysts coated with ionic liquid showed a higher turnover frequency for the water-gas shift reaction at low temperatures compared to uncoated catalysts and to the best commercial systems, because this gives a higher water concentration near the active sites and the sorption strength of CO is reduced.

Another species used in WGS is Yttrium. She et al. (She Y., 2009) investigated the effects of the addition of this element to a supported ceria copper based catalyst. They obtained the best performances with a 2%wt loading of yttrium, and from the characterization of the samples they indicated that the addition of yttrium could lead to an increase in oxygen vacancies in ceria, which gives an improved OSC and, so, a faster TOF.

De la Osa et al. (de la Osa A.R., 2012) performed a high pressure WGS over a commercial non-sulfide CoMo catalyst, using an industrial coal-derived syngas feed. Despite non-sulfide CoMo catalysts have been widely considered as non-active for WGS reaction, a surprisingly high CO conversion comparable to that attained by the sulfide one, was displayed by this catalyst in the range of conditions studied. However, non-sulfide CoMo catalyst still resulted in lower conversion values if compared with pre-sulfide one.

II.3 Chemical support

In general, the support plays often a crucial role in low temperature water gas shift, because its interaction with the active species is the main important point of the catalyst. There are many types of support that are commonly used in literature for LTS. They can be reducible, as in the case of ceria,

Chapter II

zirconia or titania, or irreducible, like alumina, silica and so on. Sometimes, the choice of a type of support rather than another one can depend also on the active species. This is really true for Panagiotopoulou et al (Panagiotopoulou P., 2006), who found that the turnover frequency (TOF) of CO conversion didn't depend on metal loading, dispersion or crystallite size, but strongly on the nature of the metal oxide carrier. In particular, catalytic activity of Pt and Ru catalysts, was 1-2 orders of magnitude higher when supported on "reducible" (TiO_2 , CeO_2 , La_2O_3 , and YSZ) rather than on "irreducible" (Al_2O_3 , MgO , and SiO_2) metal oxides. They also concluded that catalytic activity of dispersed Pt did not depend on the structural and morphological characteristics of CeO_2 , such as specific surface area or primary crystallite size.

Sometimes doping a catalyst with an appropriate material can be useful. Zhang et al. (Zhang Y., 2012) investigated the addition of ceria and K_2O on traditional Co-Mo/ Al_2O_3 catalysts. The characterization results revealed that CeO_2 addition mainly produced an electronic effect and aided to disperse the active ingredient. At the same time, the synergistic effect between Ce and K contributed to the catalytic activity. The doped catalyst exhibited higher catalytic activity and selectivity.

Another role that a support can have is to make the catalyst more stable. Andreeva et al. (Andreeva D., 2007) in two subsequent works studied the interaction between ceria and alumina in aurum based catalysts for LTS. They found that, although the activity slightly decreased, the addition of alumina promoted a more stable catalyst, and made it good for lots of practical applications.

The same studies were made by Azzam et al. (Azzam K.G., 2007); among the catalysts studied, Pt/ TiO_2 was the most active. Pt/ CeO_2 deactivated with time due to the formation of stable carbonate on the ceria surface. Sintering of Pt was found to be the cause of Pt/ TiO_2 deactivation. They also tried to use mixed oxides as support, but no improvement in terms of activity was registered, only a little enhancement of the red-ox properties.

Kalamaras et al. (Kalamaras C. M., 2009) studied the kinetic mechanism on a Pt/ TiO_2 catalyst. They determined that there is the formation of formate and carbonate on the surface of the support, but these reaction intermediates were considered only as spectators. They also found that oxygen vacancies of titania can play a crucial role in the reaction mechanism of WGS.

Another technique that is commonly used in the preparation of WGS catalysts is to employ mixed oxides. Liang et al. (Liang H., 2009) prepared a ceria modified Pt/ TiO_2 by wet impregnation method. Addition of ceria led to improvement of catalytic activity. TPR and HRTEM results showed that the interaction existed between ceria and titanium oxide and addition of ceria promoted the reducibility of platinum oxide and TiO_2 on the interface of platinum and TiO_2 particles, which contributed to high activity of the ceria modified catalyst.

An important study was made by Panagiotopoulou et al (Panagiotopoulou P., 2006). They investigated the effect of primary particle size of titania on the reducibility of a Pt/TiO₂ catalyst. They conducted their experiments on four different commercial types of titania, and registered a decrease of the WGS activity with increasing of the crystallite size of the support. They also registered a better reducibility for the samples with the smallest particle size. So, they concluded that it is necessary that titania, if used as a support for LTS, had small crystallites to have a high conversion and a good stability of the catalyst.

Si-modified Pt/CeO₂ catalysts were prepared for a water-gas shift (WGS) reaction and the effects of this silica addition on the textural and structural characteristics, reducibility and WGS reaction performance of Pt/CeO₂ were investigated by Hwang et al. (Hwang K.-R., 2011). The high specific surface area of silica contributed to help the ceria particles dispersion and enhanced the reducibility of ceria, together with the dispersion of platinum crystals. The addition of Si to ceria improved the catalytic performance for the WGS reaction, in spite of its irreducible nature.

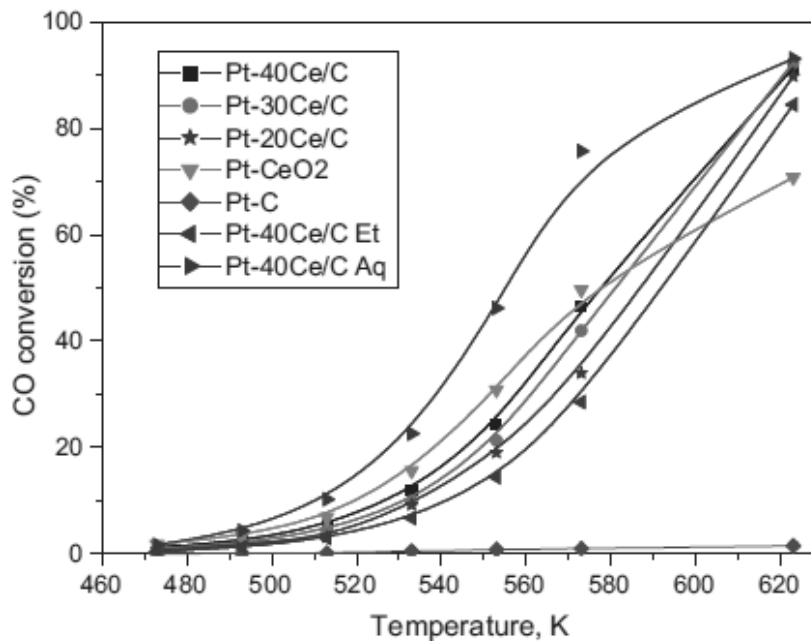


Figure 6 The importance of cerium oxide for WGS process (Buitrago R., 2012)

Buitrago et al. (Buitrago R., 2012) demonstrated the importance of ceria in WGS. They prepared various platinum based catalyst supported on ceria, the latter dispersed on an activated carbon surface, at different weight loading. This was done to slightly increase the specific surface area with a

Chapter II

less amount of ceria. Pt/C was also prepared as reference. Results showed the best performances for the catalyst with 40% of ceria, while Pt/C was not active at all, demonstrating the importance of cerium oxide for the activity of a WGS catalyst (Figure 6).

One of the most important properties of ceria is the so-called Oxygen Storage Capacity, i.e. the oxygen mobility through the support bulk. This property depends on ceria crystalline structure, so it can be improved by modifying this structure. One of the way to do this is to add another reducible oxide, such as zirconia, in order to obtain a new crystalline structure of the whole support. This was studied by Galletti et al. (Galletti C., 2009). They investigated a way to improve WGS conversion by modifying the ceria support. Zirconia, which is reducible, and Alumina, which is not reducible, were used to prove this. Results showed that, under a realistic reformat stream (containing also carbon dioxide and hydrogen), the catalyst with the zirconia reached the equilibrium conversion at 400°C, while the alumina one did not reach the equilibrium. This was attributed just on the improved OSC of ceria by adding zirconia.

Another important study on the activity of a ceria-zirconia solid solution was made by Petkovich et al. (Petkovich N. D., 2011) . They prepared two catalysts ceria and zirconia based; the first showed quite clearly two distinct phases (ceria and zirconia), while the other was one phase, a ceria-zirconia solid solution. They tested these two catalysts in the water splitting for hydrogen production, to see if there were changes in OSC. As a matter of fact, they found that the solid solution catalyst showed better activity and faster production rates, sign of an improved Oxygen Storage Capacity.

II.4 Structured carrier

The carrier plays an important role in low temperature process. Infact, the use of bed formed by random particles lead to important pressure drops, that is not useful when the gas flow rate is high. On the contrary, ceramic honeycomb the most used carrier for the LTS exhibit very low pressure drop so, the interest for this support increase in the last years. However, the operation with this type of configuration is problematic because of their poorer mass transfer, their lower thermal inertial and poor flexibility in the application where is necessary an irregular geometry. So, for avoid this limitation is necessary to find a carrier of high porosity mettalic foam seams to be a good solution.

(Banhart J., 2001) in his work describe different method for built different type of foam. In his work various manufacturing processes are classified according to the state of matter in which the metal is processed — solid, liquid, gaseous or ionised Figure 7. Liquid metal can be foamed directly by injecting gas or gas-releasing blowing agents, or by producing supersaturated metal–gas solutions Figure 8. Indirect methods include

investment casting, the use of space holding filler materials or melting of powder compacts which contain a blowing agent. If inert gas is entrapped in powder compacts, a subsequent heat treatment can produce cellular metals even in the solid state. The same holds for various sintering methods, metal powder slurry foaming, or extrusion and sintering of polymer/powder mixtures. Finally, electro-deposition or metal vapor deposition also allow for the production of highly porous metallic structures.

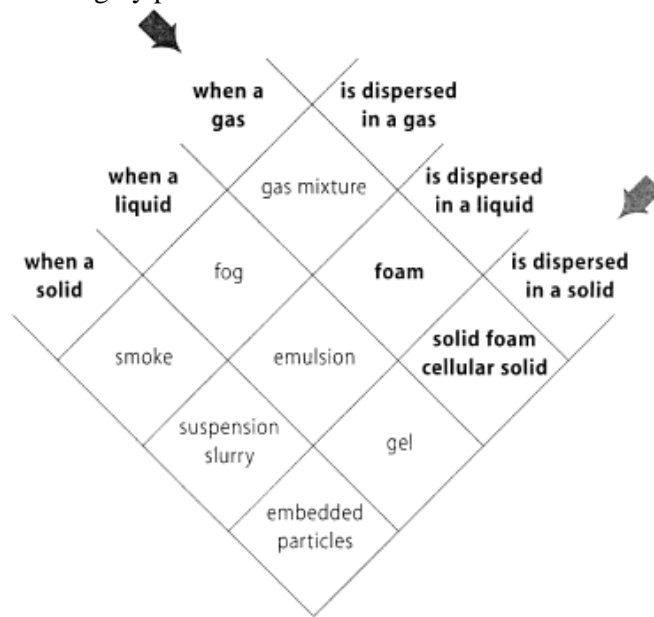


Figure 7 Dispersions of one phase into a second one. Each phase can be in one of the three states of matter (Banhart J., 2001)

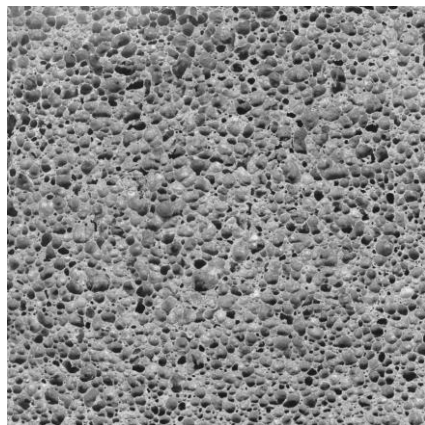


Figure 8 Pore structure of aluminium foamed by adding TiH_2 (Banhart J., 2001)

Chapter II

With this material it is possible to obtain different types of geometry which is able to fit any reactor configuration Figure 9.



Figure 9 Mechanic structure made by metallic foam (Banhart J., 2001)

The application of the foam was firstly explored for increase heat transfer.

(Lua T.J., 1998). explored the use of open-celled metal foams as compact heat exchangers, exploiting convective cooling. Moreover, they developed a model that take into account cell size and density of foam lead to the design of optimum foam structures that would maximize heat transfer per unit pumping power. Only in the last years grow up the interest in the application for the catalytic process. Thompson et al. (2013) (Thompson C.R., 2013)) explorer the performance of a silicon carbide foam supported palladium catalyst ($\text{Pd}/\beta\text{-SiC}$) in a reverse flow reactor for the abatement of methane in diluted streams. They compare the performance of catalyst structured on different carrier, Raschig rings, honeycomb monoliths and foams of equivalent geometry. Comparing the results for different superficial velocities (0.25–1.5 m/s) in terms of transport properties and performance, they concluding that honeycomb monolithic beds are the most appropriate configuration for these devices. A detailed study of different types of foams applicable as carrier in a CO combustion tests was realize in by (Groppi G., 2007). The different carrier was covered by $\text{Pd}/\gamma\text{-Al}_2\text{O}_3$ washcoated.

Table 1 Geometric Properties of the Ceramic Foam and of Metallic Foams (Groppi G., 2007)

material	pore size a (mm) measured	void fraction ϵ (%) measured	cell density (ppi) estimated	strut diameter d_s (mm)		specific area S_v (m ⁻¹) estimated
				estimated	measured	
α -Al ₂ O ₃	3.1	83.6	8.2	0.82	0.84	802
FeCrAlloy	4.3	94.5	5.9	0.66	0.73	336
FeCrAlloy	2.0	93.7	12.5	0.33	0.29	761
FeCrAlloy	1.7	93.2	15.3	0.28	0.23	962

In particular, they developed a correlation for gas/solid mass-transfer coefficients in metallic and ceramic foams. A simple cubic-cell model consisting of a framework of connected struts was preferred to an analogy with packed beds to approximate the complex cellular structure of the foams. Accordingly, in the analysis of mass-transfer data, the strut diameter was adopted as the reference length in dimensionless parameters. Also, the interstitial velocity, u_{\max} , was identified as a more adequate flow parameter than the superficial velocity, which emphasizes the analogy with heat transfer in flow across bundles of tubes. Following this approach, a generalized correlation was obtained that nicely fits the mass-transfer data of both ceramic and metallic foams (Figure 10), covering a range of void fractions from 0.84 to 0.95 and a range of Re_{\max} values from 15 to 200.

$$Sh = 0.91 Re_{\max}^{0.43} \cdot Sc^{1/3} \quad (3)$$

The resulting equation (3) is able to unify mass-transfer coefficients evaluated on foams with different pore densities and void fractions by adopting the interstitial velocity as the flow parameter according to a well-established engineering approach. Considering the Colburn analogy, it is also in excellent agreement with independent gas/solid heat-transfer measurements in foams performed at a different scale using completely different experimental methods, which lends confidence to its physical consistency. The correlation in 3 permits the evaluation, on an extended basis, of the mass-transfer properties of metallic and ceramic foams as catalyst supports, thus opening the way to the engineering design of foam-based catalytic systems for fast, diffusion-limited processes; it further allows a rational comparison with alternative, more conventional catalyst supports such as pellets and honeycomb monoliths

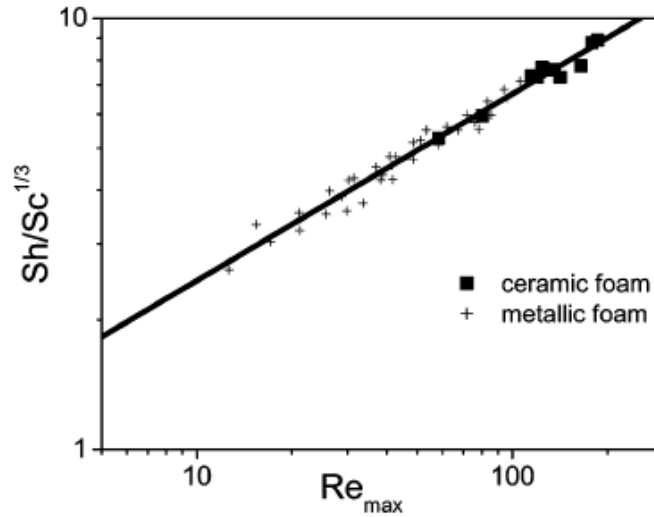


Figure 10 Sh vs Re_{max} logarithmic plot. Overall correlation of mass-transfer data for ceramic and metallic foams. The solid line represents (Groppi G., 2007)

(Palma V., 2009) for the intensification of WGS process operated a comparison between different reactor configurations. The flexibility of the SiC/Al₂O₃ foam Figure 11 carrier allowed to develop a radial reactor, which could not have been realized with other structured carriers, like honeycomb.

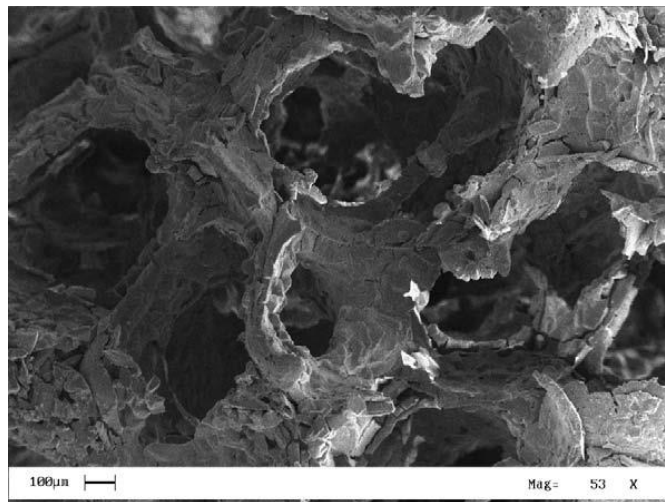


Figure 11 SEM image of the SiC/Al₂O₃ based foam support (Palma V., 2009)

The comparison revealed that the radial configuration led to higher hydrogen yield, and the use of a structured foam catalyst allowed to operate at high space velocities with relatively low pressure drops.

II.5 Washcoat formulation

For guarantee a good dispersion of the active phase on carrier it is necessary to find a chemical species that have good affinity both with carrier and with the active phase. The chemical species is called washcoat. It is a porous, high surface area layer bonded to the surface of the support. The main function of the washcoat is to provide high surface area needed for the dispersion of catalytic metals. Additionally, the washcoat can physically separate and prevent undesired reactions between components of a complex catalytic system. The exact role of the washcoat clearly very important for many aspects of the catalyst activity and durabilit is not always understood or explained. Washcoat materials include inorganic base metal oxides such as Al_2O_3 (aluminum oxide or alumina), SiO_2 , TiO_2 , CeO_2 , ZrO_2 , V_2O_5 , La_2O_3 and zeolites. Some of them are used as catalyst carriers, others are added to the washcoat as promoters or stabilizers, still others exhibit catalytic activity of their own.

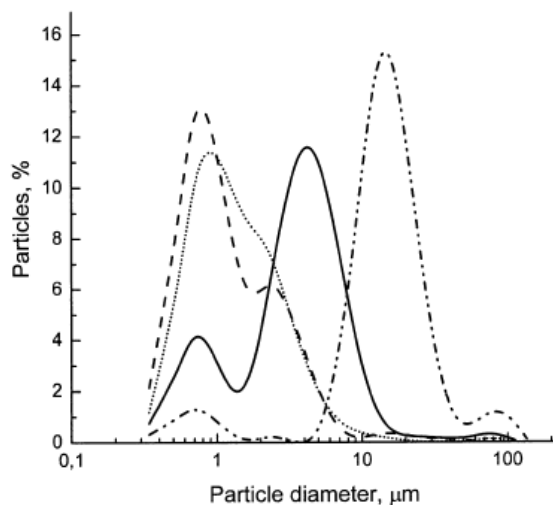


Figure 12 Particle size distribution of the catalyst powders for washcoating: as supplied (dash-dotted line); after 3 h of milling in nitric acid (pH) 5; dashed line); after 3 h of milling in citric acid (pH) 4; dotted line); and after 3 h of milling in citric acid (pH) 6; continuous line). (González-Velasco J. R., 2003)

Different parameter can influence the dispersion of catalytic active phase on support (González-Velasco J. R., 2003) studied the effect of pH on the dispersion of active phase in aqueous solution. They found that the particle

Chapter II

size decrease at lower pH, and a nitric acid solution provides smaller particles than a citric acid solution. To achieve an adequate washcoating of the material, the slurry should be composed of particles below 10 mm in diameter. Besides the particle size distribution, it is also important to stabilize the slurry in an acidic medium. Although the pH, in the studied range, affected the particle size distribution obtained during wet grinding of the slurry, no effect on washcoating was observed provided that the particles in the slurry were small enough.

Table 2 TiO₂ Washcoat Stability without Binders after Ultrasonic Vibration (uv), Thermal Shock (ts), and Abrasion (a) (González Carlos A., 2007)

washcoat	wt losses uv (%)	wt losses after uv, ts, a (%)	wt diff (%)
TiO ₂ (H) without milling	4.6	8.2	3.6
TiO ₂ (sg) without milling	5.0	11.5	6.5
TiO ₂ (H) milled	0.7	1.2	0.5
TiO ₂ (sg) milled	1.4	2.2	0.8

^a H, Hombikat; sg, sol-gel.

Table 3 Effect of Binders on TiO₂ and Pd/TiO₂ Washcoat Stability after Ultrasonic Vibration (uv), Thermal Shock (ts), and Abrasion (a) (González Carlos A., 2007)

(binder)-washcoat	wt losses uv (%)	wt losses after uv, ts, a (%)	wt diff (%)
(Al ₂ O ₃ s)-TiO ₂ (H) ^b	3.6	8.2	4.6
(TiO ₂ A)-TiO ₂ (H) ^b	2.3	7.2	4.9
(TiO ₂ sg-pH 9)-TiO ₂ (H) ^b	10.0	15.8	5.8
(Al ₂ O ₃ s)-TiO ₂ (H) ^c	2.3	2.4	0.1
(TiO ₂ sg-pH 9)-TiO ₂ (H) ^c	12.4	13.6	1.2
(TiO ₂ sg-pH 3)-TiO ₂ (H) ^c	4.1	4.2	0.1
Pd/TiO ₂ (sg) ^d	3.5	4	0.5
(Al ₂ O ₃ s)-Pd/TiO ₂ (sg) ^d	1.2	1.2	0.0
Pd/TiO ₂ (H) ^d	2.3	3.0	0.7
(Al ₂ O ₃ s)-Pd/TiO ₂ (H) ^d	0.3	0.3	0.0

^a H, Hombikat; s, sol; A, Aldrich; sg, sol-gel. ^b Minimonolith submerged in slurries prepared with binders of (Al₂O₃ s), (TiO₂ A) or (TiO₂ sg-pH 9) before being submerged in TiO₂ (H) slurries without milling. ^c Minimonolith submerged in mixtures of slurries with binders and TiO₂ (H) without milling. ^d Minimonolith submerged onto both slurries of milled Pd/TiO₂ (Hombikat or sol-gel) and milled mixtures of binders and Pd/TiO₂ slurries.

More significant was the effect of the nature of the acid used to reduce the pH in the slurry solution: nitric acid, compared to citric acid, produced a quicker washcoating uptake, even for almost identical particle size

distributions in the slurry. Fine particles of around 1 μm and a pH of 5 obtained by the addition of nitric acid to the slurry solution were chosen to prepare the optimum washcoated monolithic catalyst. In this way, a good adherence of the catalyst to the cordierite substrate up to 30 wt % after 16 subsequent immersions was achieved.

(González Carlos A., 2007) studied the influences of different parameter on the washcoat adhesion through different resistance tests (Ultrasonic Vibration (uv), Thermal Shock (ts), and Abrasion (a)^a). The authors conclude that the washcoats prepared with fine particles (submitted to milling operations) are more tightly supported on cordierite honeycomb and mechanical stability does not depend on the TiO_2 type (Table 2 and Table 3).

Chapter III. Structured carriers: heat transfer study. Experimental

III.1 Structured carriers properties

For the purposes of this work, four different types of foams were purchased: in particular, three metallic foams (ferritic foam, FeCr Alloy foam and Aluminum foam), and an Alumina foam. The main geometric properties of these structured carriers are available in Table 4.

Table 4 Composition and geometric properties of the foams

Sample name	Material Code	Composition	Porosity (pores per inch, PPI)	Void fraction (%)
Vesuvius	AL92	100% Alumina	65	85
Belarus	Fe-FeO _x	Fe-FeO _x	20	92
Fraunhofer	FeCr Alloy	Stainless steel	30	93
ERG Duocel	AlFoam	Aluminum	40	88

While all foams were chosen in order to have almost the same void fraction, the PPI value of each sample change, in particular from a minimum value of 20 relative to the ferritic foam up to 65 PPI of the Alumina foam. This choice was made in order to study also if the tortuosity of the material can enhance significantly the heat transfer. On the other hand, the tortuosity of the system could also increase the pressure drop; for this last phenomenon, see Section 4.

III.2 Heat transfer tests

In order to perform the heat transfer tests all the foams have been cut and shaped appropriately to obtain cylindrical monoliths. Several thermocouples were inserted at equidistant points of the foam to be able to measure both the temperature of the foam itself that the temperature of the gas. The monolith

Chapter III

was then surrounded by a heat-expanding pad, to avoid by-pass phenomena, and placed inside a quartz tube.

The quartz tube had an internal diameter of 23 mm; this was placed in an electrical oven in order to assure a uniform temperature on the external surface of the reactor. A cold nitrogen stream was sent in the reactor, by varying the volumetric flow rate and the temperature of the furnace. The main test parameters were reported in Table 5.

Table 5 Heat transfer tests: operating conditions

Condition	Value
Tube internal diameter	23 mm
Oven temperature	200 – 600 °C
Volumetric flow rate	1.2-3.6 Ndm ³ /min
Foam diameter	15 mm

These tests were made by varying oven temperature and volumetric gas flow rate, in order to optimize and validate the mathematical model, which is explained in more details in Section III.3. The temperature data of all tests were continuously recorded by the device Multicon CMC-141, purchased by Simex.

III.3 Modeling of the system

The heat transfer mathematical model was developed starting by the system energy balance (4), inspired by what reported in the literature by Hayes et al. (1997):

$$IN - OUT + GEN = ACC \quad (4)$$

The whole model takes into account the following assumptions:

- No chemical reactions (GEN=0)
- Steady state conditions (ACC=0)
- Negligible radial thermal profile, both in gas and in solid phase
- No radiative phenomena.

With regard to the modeling of the gas flowing through the foam, it has been imagined that the two phases are a sort of continuum, so that the whole system can be seen as an annular cylinder of foam surrounding the gas phase. In Figure 13 a schematic representation of the model is displayed.

So, starting from the assumptions available above, the gas phase and solid phase balances were performed. It has been used a differential element both in the gas phase and in the solid phase, with a length of Δz , by considering all the incoming and outgoing heat flows, as assumed. A detailed scheme of the two-phases balance is shown in Figure 14

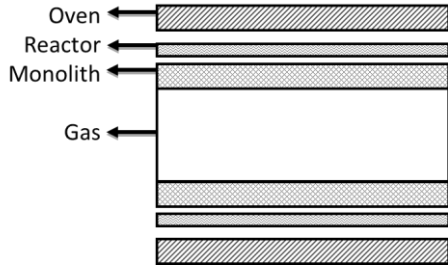


Figure 13 Schematic representation of the heat exchange model

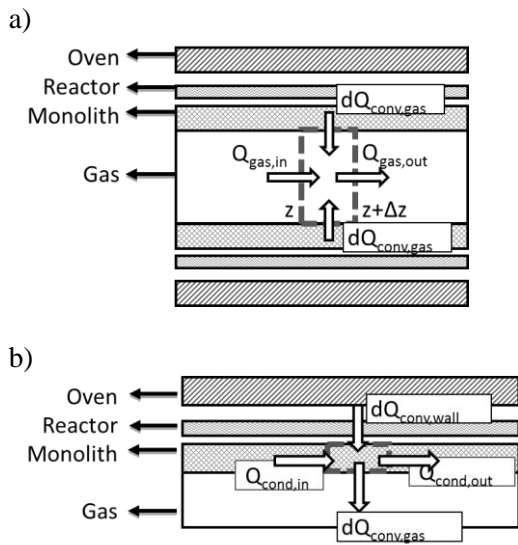


Figure 14 Gas (a) and solid (b) phase balance detailed scheme

By processing and rearranging the two balances, two differential equations can be obtained (5 and 6):

$$\frac{dT_g}{dz} = \frac{h_g \cdot \pi \cdot D \cdot \varepsilon}{F \cdot c_p} (T - T_g) \quad (5)$$

$$\frac{d^2T}{dz^2} = 4 \frac{\varepsilon}{1 - \varepsilon} \frac{h_g}{kD} \left[(T - T_g) - \frac{h}{h_g - h} (T_{ov} - T) \right] \quad (6)$$

with the appropriate boundary conditions (7 and 8):

$$T_g(z = 0) = T_g^0 \quad (7)$$

Chapter III

$$k \cdot \left[\frac{dT}{dz} \right]_{z=0} = k \cdot \left[\frac{dT}{dz} \right]_{z=L} = 0 \quad (8)$$

Symbols in the equations: T_g : gas temperature; z = axial coordinate; h_g : solid-gas heat transfer coefficient; D : foam diameter; ε : foam's void fraction; F : mass flow rate; c_p : nitrogen heat capacity; T : solid temperature; k : material thermal conductivity; h : global heat transfer coefficient; T_{ov} : oven temperature; L : foam monolith length.

This differential model was then discretized and processed in Microsoft Excel™, solving it by means of finding the optimum value of the two parameters h_g (gas phase heat exchange coefficient) and k (material thermal conductivity), through the least squares method.

Chapter IV. Catalytic powders: Experimental

IV.1 Preparation of the catalysts in powder form

The catalysts used in the water gas shift tests were prepared in the PROCEED laboratory, Industrial Chemistry and Catalysis, Department of Industrial Engineering, University of Salerno.

These samples are based on Pt supported on cerium oxide (IV), or on a ceria-zirconia solid solution. Then, a Pt catalyst supported on Alumina, covered with ceria, was also prepared. The amount of 14% was chosen in order to obtain a ceria monolayer on alumina support; this was done to study a catalyst with less amount of rare earth. In particular, the used samples are the following:

- 1% Pt/CeO₂
- 1% Pt/CeO₂-ZrO₂
- 1% Pt/14%CeO₂/Al₂O₃

Where the percentages are by weight.

The addition of the active species was conducted, through the method of wet impregnation, on a support previously subjected to calcination in a muffle at 600°C for 3h.

The CeO₂ and CeO₂/ZrO₂ (57.4 %w/w of ceria) supports were provided by Rhodia, the γ -Al₂O₃ by Sasol while the 14CeAl (14 %w/w of Ce in CeO₂/ γ -Al₂O₃) was prepared by the method indicated below; the PtCl₄ (\geq 99.9 % trace metals basis) and Ce(NO₃)₃·6H₂O (99.99 trace metals basis) were supplied from Sigma-Aldich.

The 1 % Pt/CeO₂ (PtCe) and 1 % Pt/CeO₂/ZrO₂ (PtCeZr) catalysts, both containing 1 %w/w of Platinum, were prepared by impregnation of the support with an aqueous solution of the proper amount of PtCl₄, and the mixture was stirred at the boiling point until evaporation occurred. The resulting solid was dried in an oven at 393 K for 3 h and then calcined at 873 K for 3 h.

In the case of 1%Pt/14%CeO₂/Al₂O₃, Basically, the amount of active species was maintained intact, while the support was modified by adding a

Chapter IV

large quantity of alumina to ceria. The choice of alumina was made not only because it is a very diffuse compound in the world, but also because it guarantees a high specific surface value of the final catalyst. Another choice was made on the quantity of ceria. This refers to the acid properties of alumina. In fact, it is well known from the literature that alumina is not a good support for WGS reaction, because it generates a not so stable catalyst. In fact in the conventional LTS catalyst, zinc is used not only to promote copper, but also to enhance the stability of the catalyst. So, it was decided to use a proper amount of ceria in order to cover the alumina surface and avoid deactivation.

So, the 14CeAl was prepared by impregnation of γ -Al₂O₃ with 4 equimolar aliquots of a water solution of Ce(NO₃)₃·6H₂O. In each impregnation the mixture was stirred at the boiling point until evaporation of the water occurred, the resulting solid was dried in an oven at 393 K for 3 h and then calcined at 673 K for 9 h.

The precursor of platinum was a solution of platinum nitrate, prepared by the method of (Vasilchenko D., 2013). The 1 % Pt/14CeAl (Pt14CeAl) was prepared by impregnation of 14CeAl with the proper amount of the platinum nitrate solution and the mixture was stirred at the boiling point until evaporation occurred; the resulting solid was dried in an oven at 393 K for 3 h and then calcined at 673 K for 6 h.

IV.1.1 Impregnation

The impregnation method involves the dispersion of the powder of the support in a solution of the active phase precursor. The supports used are cerium oxide (Rhodia) and a mixed support based on ceria and zirconia (Rhodia, cerium content: 57.4% by weight), while the Pt salt precursor of the active species used for the impregnation is the platinum chloride (PtCl₄, Aldrich). A quantity of salt, dependent on the load of the desired metal, is dissolved in a beaker containing distilled water in large excess compared to the solubility of the salt itself; dissolution takes place on a plate, stirred at room temperature. The support is then added to the clear solution, on a stirred plate, at 250°C. The sample, once the solvent is evaporated, is put in an oven at 120°C overnight, and finally calcined in a muffle at 600°C for 3h.

IV.1.2 Calcination

The calcination is a heating in air which involves some modifications, both chemical and structural, to the catalyst; in particular, the removal of the not linked water, water lattice and other compounds present in the precursor salts that are not useful to catalysis.

At the end of calcination, the catalyst will suffer a loss of weight, changes in the porous structure and the size of the crystals by sintering, the

generation of the active phase and the stabilization of the mechanical properties. The main aim of the calcination step is the transformation into oxides of all species in the formulation of the catalyst.

The conditions for the calcination of the samples used in this work were established on the basis of the results of thermal gravimetric, literature, and the reaction temperature. The calcination was carried out by placing the catalyst in a muffle; treatment foresaw a programmed temperature (heating rate, 10°C/min) up to a temperature of 600°C, followed by a stage of isotherm at 600°C for 3h.

IV.2 Characterization of the catalysts in powder form

All the catalysts were characterized with different techniques, in order to evaluate the wellness of the preparation method and to study the chemical and physical properties of the samples. The techniques used in this work are as follows:

- Thermo-Gravimetric Analysis (TGA) and Mass Spectrometry (MS)
- X-Ray Diffraction (XRD)
- Determination of the Specific Surface Area (SSA)
- Electron microscopy
- Temperature Programmed Reduction (TPR)
- Raman Spectroscopy.

IV.2.1 Thermo Gravimetric Analysis and Mass Spectrometry (TG-MS)

The thermo-gravimetric analysis is continuously recording the variations of the mass of a sample as a function of temperature in a controlled atmosphere, inert (nitrogen flow), reducing (hydrogen flow) or in the air. With this technique it is possible to identify any processes of decomposition and dehydration, with consequent reduction of the mass (Reagent → Product + Gas) or oxidation, with relative mass increases (Reagent + Gas → Product).

A thermo-gravimetric curve is obtained, which shows three quantities as a function of temperature:

- the change in mass, as an absolute value or percentage
- the first derivative of the weight in time (DTG), which provides information on the kinetics of the process
- the heat flux, which reveals its endothermic or exothermic nature.

The equipment used for the thermo gravimetric analysis is often coupled with a mass spectrometer, in order to analyze and distinguish any species released from the sample during the undergone treatment. Since the furnace is at atmospheric pressure, while the analysis system operates in vacuum

Chapter IV

conditions (10^{-7} atm), a quartz capillary, the internal diameter of 100 microns, is used to allow the passage of gases between the two devices .

The mass spectrometer works for separating a mixture of ions according to their mass/charge ratio (m/z), generally via magnetic fields. Obviously, the molecules of the species present in the stream must be ionised; this is obtained by bombarding them with an electron beam energy, emitted from a known resistance tungsten incandescent yield.

In order to have an indication of the decomposition reactions that occur during the test, the data of weight loss and temperature variation are compared with the species detected by the mass spectrometer. In this way, the type and amount of substances lost from the sample, as well as the exothermicity or endothermicity of the reactions are measured.

The apparatus used were a TGAQ500 thermogravimetric analyzer (TA Instruments) and a SDTQ600 simultaneous DSC/TGA (TA Instruments). Both analyzers can be coupled to a Pfeiffer Vacuum Benchtop Thermostar mass spectrometer (MS).

TGAQ500 measures weight changes in a material as a function of temperature. The system works in a temperature range of 20-1000 °C, and weight variation resolution is 0.1 µg . The sample, loaded in a crucible made of platinum and connected to the balance arm by a small hook, is progressively heated in the oven. A thermocouple controls the oven temperature and a second thermocouple reads the sample temperature. Sample pan loading and furnace movement are totally automated and there is a touch screen data display to change operating parameters. Typically measurements are carried out with 20 mg of sample in chromatographic air flow (60 Ncc/min) with a heating rate of 10 °C/min in the temperature range of 20- 800 °C (Figure 15).

The results are displayed as TG curves showing the mass variations as functions of temperature or time, and DTG curves showing the conversion rate (mass loss percentage per unit time) as functions of temperature or time.

Figure 15 contains the typical trends of the TG and DTG curves. SDTQ600 provides a simultaneous measurement of weight change (TGA) and heat flow (DSC) on the same sample from ambient to 1500 °C. It features a proven horizontal dual beam design with automatic beam growth compensation, and the ability to analyze two TGA samples simultaneously. DSC heat flow data is dynamically normalized using the instantaneous sample weight at any given temperature. The sample is loaded in a crucible made of alumina and heated in the horizontal oven. There are two thermocouples to control the oven temperature and the sample temperature. Measurements are carried out with about 30 mg of sample in chromatographic air flow (100 Ncc/min) with a heating rate of 10 °C/min in the temperature range of 20- 800 °C.

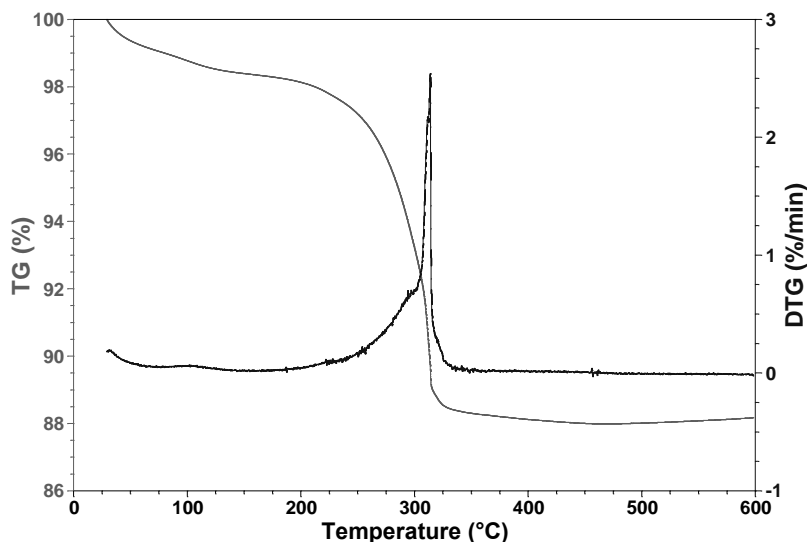


Figure 15 TG and DTG curves

Pfeiffer Vacuum Benchtop Thermostar mass spectrometer can measure the gas evolved from thermal analyzers up to 300 AMU. The evolved gases are introduced into a heated quartz capillary, which is extremely fine, in order to produce the necessary high vacuum, when the evolved gases enter the mass spectrometer. The heated capillary is necessary in order to prevent condensation of the hot gases on cold surfaces. The analysis of gases is performed by a very high sensitive quadrupole mass detector. The necessary high vacuum is obtained through 2 stages of vacuum pumps that are integrated into a compact housing. First stage is a rotary pump; second stage is a turbo molecular pump.

Both systems, the Mass Spectrometer and the Thermal Balance, are connected to a common PC for data acquisition.

IV.2.2 XRD powder diffraction

Materials are made of atoms. Knowledge of how atoms are arranged into crystal structures and microstructures is the foundation on which we build our understanding of the synthesis, structure and properties of materials. There are many techniques for measuring chemical compositions of materials, and methods based on inner-shell electron spectroscopies are covered in this book. The larger emphasis of the book is on measuring spatial arrangements of atoms in the range from 10^{-8} to 10^{-4} cm, bridging from the unit cell of the crystal to the microstructure of the material. There are many different methods for measuring structure across this wide range of distances, but the more powerful experimental techniques involve diffraction.

Chapter IV

To date, most of our knowledge about the spatial arrangements of atoms in materials has been gained from diffraction experiments. In a diffraction experiment, an incident wave is directed into a material and a detector is typically moved about to record the directions and intensities of the outgoing diffracted waves. “Coherent scattering” preserves the precision of wave periodicity. Constructive or destructive interference then occurs along different directions as scattered waves are emitted by atoms of different types and positions.

The X-ray diffraction is an analytical technique, non-destructive, for the identification of the crystalline phases present in a solid material or powder.

X-rays are electromagnetic waves with a wavelength of the order of 0.1 nm, comparable to the atomic distances in crystals.

There is a profound geometrical relationship between the directions of waves that interfere constructively, which comprise the “diffraction pattern,” and the crystal structure of the material. The diffraction pattern is a spectrum of real space periodicities in a material. Atomic periodicities with long repeat distances cause diffraction at small angles, while short repeat distances (as from small interplanar spacings) cause diffraction at high angles.

It is not hard to appreciate that diffraction experiments are useful for determining the crystal structures of materials. Much more information about a material is contained in its diffraction pattern, however. Crystals with precise periodicities over long distances have sharp and clear diffraction peaks. Crystals with defects (such as impurities, dislocations, planar faults, internal strains, or small precipitates) are less precisely periodic in their atomic arrangements, but they still have distinct diffraction peaks. Their diffraction peaks are broadened, distorted, and weakened, however, and “diffraction lineshape analysis” is an important method for studying crystal defects. Diffraction experiments are also used to study the structure of amorphous materials, even though their diffraction patterns lack sharp diffraction peaks. In a diffraction experiment, the incident waves must have wavelengths comparable to the spacings between atoms. Three types of waves have proved useful for these experiments. X-ray diffraction (XRD), conceived by von Laue and the Braggs, was the first. The oscillating electric field of an incident x-ray moves the atomic electrons and their accelerations generate an outgoing wave. In electron diffraction, originating with Davisson and Germer, the charge of the incident electron interacts with the positively-charged core of the atom, generating an outgoing electron wavefunction.

In neutron diffraction, pioneered by Shull, the incident neutron wavefunction interacts with nuclei or unpaired electron spins. These three diffraction processes involve very different physical mechanisms, so they often provide complementary information about atomic arrangements in materials. Nobel prizes in physics (1914, 1915, 1937, 1994) attest to their

importance. As much as possible, we will emphasize the similarities of these three diffraction methods, with the first similarity being Bragg's law.

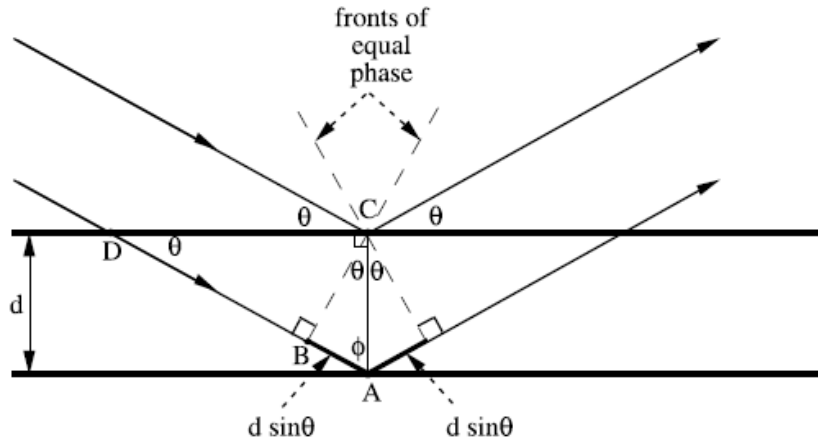


Figure 16 Geometry for interference of a wave scattered from two planes separated by a spacing, d . The dashed lines are parallel to the crests or troughs of the incident and diffracted wavefronts. The important path length difference for the two rays is the sum of the two dark segments

IV.2.2.1 Bragg's Law

Figure 16 is the construction needed to derive Bragg's law. The angle of incidence of the two parallel rays is θ . You can prove that the small angle in the little triangle is equal to θ by showing that the two right triangles, ABC and ACD, are similar. (Hint: Look at the shared angle of $\phi = \pi/2 - \theta$).

The interplanar spacing, d , sets the difference in path length for the ray scattered from the top plane and the ray scattered from the bottom plane. Figure 16 shows that this difference in path lengths is $2d \sin \theta$. Constructive wave interference (and hence strong diffraction) occurs when the difference in path length for the top and bottom rays is equal to one wavelength, λ :

$$2d \sin \theta = \lambda. \quad (9)$$

The right hand side is sometimes multiplied by an integer, n , since this condition also provides constructive interference. Our convention, however, sets $n = 1$. When there is a path length difference of $n\lambda$ between adjacent planes, we change d (even though this new d may not correspond to a real interatomic distance). For example, when our diffracting planes are (100) cube faces, and then we speak of a (200) diffraction from planes separated by $d_{200} = (d_{100})/2$.

$$2d_{100} \sin \theta = 2\lambda \quad (10)$$

Chapter IV

A diffraction pattern from a material typically contains many distinct peaks, each corresponding to a different interplanar spacing, d . For cubic crystals with lattice parameter a_0 , the interplanar spacings, d_{hkl} , of planes labeled by Miller indices (hkl) are:

$$d_{hkl} = \frac{a_0}{\sqrt{h^2 + k^2 + l^2}} \quad (11)$$

(as can be proved by the definition of Miller indices and the 3D Pythagorean theorem). From Bragg's law (9) we find that the (hkl) diffraction peak occurs at the measured angle $2\theta_{hkl}$:

$$2\theta_{hkl} = 2 \arcsin \left(\frac{\lambda \sqrt{h^2 + k^2 + l^2}}{2a_0} \right) \quad (12)$$

There are often many individual crystals of random orientation in the sample, so all possible Bragg diffractions can be observed in the "powder pattern." There is a convention for labeling, or "indexing," the different Bragg peaks in a powder diffraction pattern using the numbers (hkl) . An example of an indexed diffraction pattern. The intensities of the different diffraction peaks vary widely, and are zero for some combinations of h , k , and l . For this example of polycrystalline silicon, notice the absence of all combinations of h , k , and l that are mixtures of even and odd integers, and the absence of all even integer combinations whose sum is not divisible by 4. One important use of x-ray powder diffractometry is for identifying unknown crystals in a sample. The idea is to match the positions and the intensities of the peaks in the observed diffraction pattern to a known pattern of peaks from a standard sample or from a calculation. There should be a one-to-one correspondence between the observed peaks and the indexed peaks in the candidate diffraction pattern. For a simple diffraction pattern, it is usually possible to guess the crystal structure with the help of the charts in. This tentative indexing still needs to be checked. To do so, the θ -angles of the diffraction peaks are obtained, and used with (9) to obtain the interplanar spacing for each diffraction peak. For cubic crystals it is then possible to use (11) to convert each interplanar spacing into a lattice parameter, a_0 . (Non-cubic crystals usually require an iterative refinement of lattice parameters and angles.) The indexing is consistent if all peaks provide the same lattice parameter(s).

For crystals of low symmetry and with more than several atoms per unit cell, it becomes increasingly impractical to index a diffraction pattern by hand. An old and reliable approach is "fingerprinting." The International Centre for Diffraction Data, ICDD, maintains a database of diffraction patterns from hundreds of thousands of inorganic and organic materials. For each material the data fields include the observed interplanar spacings for all

observed diffraction peaks, their relative intensities, and their hkl indexing. Software packages are available to identify peaks in the experimental diffraction pattern, and then search the ICDD database to find candidate materials. Computerized searches for pattern matches are particularly valuable when the sample contains a mixture of unknown crystalline phases. The task of indexing a diffraction pattern is helped with information about chemical compositions and candidate crystal structures. For example, candidate phases can be identified with handbooks of phase diagrams, and their diffraction patterns found in the ICDD database.

When the sample contains multiple phases, there can be ambiguity in assigning a diffraction peak to a specific diffraction pattern, and there can be overlaps of peaks from different patterns. A computerized match of full patterns often proves helpful in such cases. Nevertheless, sometimes it is easy to distinguish individual diffraction patterns. The diffraction pattern in was measured to determine if the surface of a glass-forming alloy had crystallized. The amorphous phase has two very broad peaks centered at $2\theta = 38^\circ$ and 74° . Sharp diffraction peaks from crystalline phases are easily distinguished. Although this crystalline diffraction pattern has not been indexed, the measurement was useful for showing that the solidification conditions were inadequate for obtaining a fully amorphous solid.

Another approach to structure determination by powder diffractometry is to calculate diffraction patterns from candidate crystal structures, and compare them to the measured diffraction patterns. Central to calculating a diffraction which are characteristic of each crystal structure.

Simple diffraction patterns can be calculated with a hand calculator, but structure factors for materials with more complicated unit cells require computer software. The most straightforward software packages take input files of atom positions, atom types, and x-ray wavelength, and return calculated positions and intensities of powder diffraction peaks. In an important extension of this approach, some features of the crystal structure, e.g., lattice parameters, are treated as adjustable parameters.

These parameters are adjusted or “refined” as the software finds the best fit between the calculated and measured diffraction patterns.

IV.2.2.2 Scherrer's Equation

Depending on how the atoms are arranged in space, then X-rays are diffracted by the crystal structure and give rise to maximums and minimums (intensity), due to interference phenomena, detected by a suitable detector. The trend of the measured intensity obtained varying the theta angle, or the distance d , is known as Diffraction Spectrum. It provides useful information on the composition and the crystal size of the sample. For a non-crystalline substance a spectrum consisting of a single pulled aside peak is obtained, confirming the suitability of this technique not to characterize amorphous

Chapter IV

materials. Regarding the quantitative analysis, to determine the average crystallite size, the Scherrer relationship is used:

$$D = k \cdot \frac{\beta}{\cos \varphi \cdot L} \quad (13)$$

where β is the peak width at half height, k is a constant (usually between 0.87 and 1) and L is the average linear dimension mediated in volume.

The instrument used for the X-ray diffraction in this work is a micro diffractometer, able to investigate areas of the order of some tens of microns and, therefore, applicable to measurements on small amounts of sample.

The operating principle of the instrument is based on the emission of electrons which are accelerated in accordance with a voltage difference. The electrons reach a copper target, which, excited, emits electromagnetic radiation with a wavelength in the field of X-rays, which are channelled through a collimator on the sample. The specimen has the possibility to move through axial rotation around the base of the structure (angle ω) or the angular rotation (angle φ), to send the rays on different points of the area investigated, mediating the measurement. The diffracted rays are collected on the plate, from which it is possible to obtain the diffraction plate.

The catalysts, previously calcined, were analyzed by exposing them for 10 minutes to X-ray beam and imposing a rotation to the sample holder. The results are obtained in the form of plate (Figure 17) which is subsequently processed in such a way as to obtain the classic diffractogram (Figure 18), which shows the intensity as a function of the 2θ angle.

The spectra were obtained in the 2θ range between 20° and 80° , using a radiation of wavelength λ equal to 1.54060 \AA .

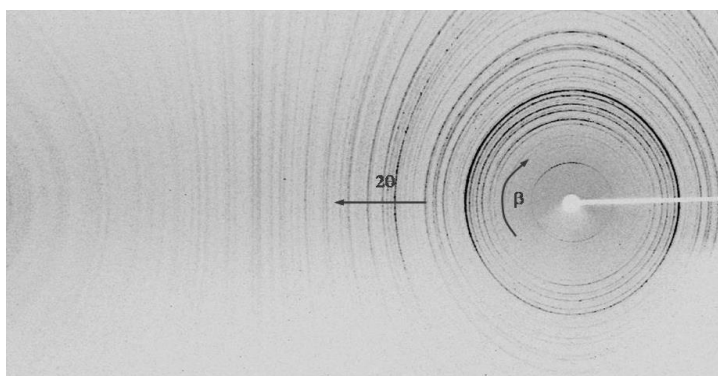


Figure 17 Diffraction plate of XRD

This technique has been used for the fresh samples but also for the samples post-test, in order to analyze the potential effect of the reaction on the crystallite size and the species present. The limit of the analysis carried out lies in the difficulty of identifying compounds present in very low

percentages (below 5%), since the intensity of the peaks is proportional to the concentration, and identify substances well dispersed in the solid bulk, because the diffraction, to be well amplified, must include a fairly extensive area.

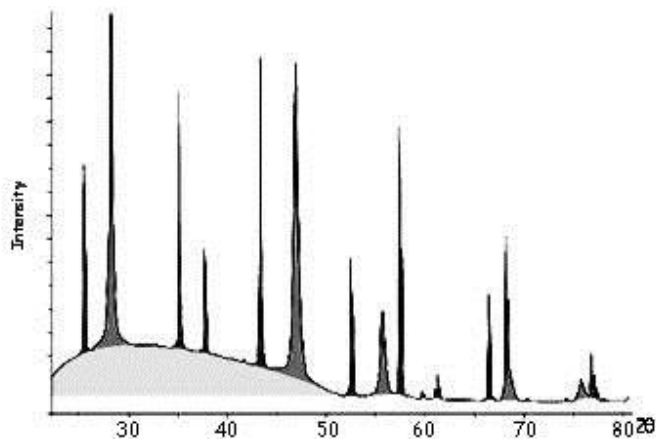


Figure 18 Typically XRD spectrum

IV.2.3 Determination of the specific surface area (SSA)

Surface area and porosity are important parameters in powdered materials. The most widely used techniques for estimating surface area are based on physical adsorption of gas molecules on a solid surface.

Generally gas adsorption on solid surfaces and in the pore spaces is a complex phenomenon involving mass and energy interaction and phase changes. Depending upon the strength of the interaction, all adsorption processes can be divided into the two categories of chemical or physical adsorption. The former, also called irreversible or chemisorption, is characterized mainly by large interaction potentials, which lead to high heats of adsorption often approaching the values of chemical bonds. This fact, coupled with other spectroscopic, electron spin resonance, and magnetic susceptibility measurements, confirms that chemisorption involves true chemical bonding of the gas or vapour with the surface. Because chemisorption occurs through chemical bonding, it is often found to occur at temperatures above the adsorbates' critical temperature. Strong bonding to the surface is necessary, in the presence of higher thermal energies, if adsorption has to occur at all. Also, as it is true for most chemical reactions, chemisorption is usually associated with an activation energy. In addition, chemisorption is necessarily restricted to, at most, a single layer of chemically bound adsorbate at the surface. Another important factor relating to chemisorption is that the adsorbed molecules are localized on the surface. Because of the formation of a chemical bond between an adsorbate molecule

Chapter IV

and a specific site on the surface, the adsorbate is not free to migrate along the surface. This fact often enables the number of active sites on catalysts to be determined by simply measuring the quantity of chemisorbed gas. The second category, reversible or physical adsorption, exhibits characteristics that makes it most suitable for surface area determinations as indicated by the following:

- Physical adsorption is accompanied by low heats of adsorption with no violent or disruptive structural changes occurring on the surface during the adsorption measurements.
- Unlike chemisorption, physical adsorption may lead to surface coverage by more than one layer of adsorbate. Thus, pores can be filled by the adsorbate for pore volume measurements.
- At elevated temperatures physical adsorption does not occur or is sufficiently slight that relatively clean surfaces can be prepared on which to make accurate surface area measurements.
- Physical adsorption equilibrium is achieved rapidly since no activation energy is required as in chemisorption. An exception here is adsorption in small pores, where diffusion can limit the adsorption rate.

Physical adsorption is fully reversible, enabling both the adsorption and desorption processes to be studied.

· Physical adsorbed molecules are not restrained to specific sites and are free to cover the entire surface. For this reason surface areas, rather than the number of sites, can be calculated.

The kinetics and thermodynamics of adsorption have been extensively studied, but, when surface area and pore structure are the subject of interest, it's essential to establish the meaning of an adsorption (desorption) isotherm. This is a measure of the molar quantity of gas n (or standard volume V_a , or general quantity q) taken up, or released, at a constant temperature T by an initially clean solid surface as a function of gas pressure P . In order to increase the amount of physisorbed molecules (usually nitrogen) most frequently the test is conducted at a cryogenic temperature, usually that

of liquid nitrogen (LN_2) at its boiling point (77.35 K at 1 atm pressure). Convention has established that the quantity of gas adsorbed is expressed as its volume at standard temperature and pressure conditions ($0^\circ C$ and 760 torr and denoted by STP), while the pressure is expressed as a relative pressure, which is the actual gas pressure P divided by the vapor pressure P_0 of the adsorbing gas at the temperature of the test. Plots of V_a as the ordinate against P/P_0 as the abscissa reveal much about the structure of the adsorbing

material (called the adsorbent) simply from their shape. The theory mainly used in order to get essential information (such as surface area and pore distribution) from experimental adsorption isotherm is known as BET theory from the surnames of its creators, Brunauer, Emmett and Teller.⁵⁰ This is an extension to multilayer adsorption of the Langmuir model (related to monolayer molecular adsorption) and the resulting BET equation is expressed as follows:

$$V_{\alpha} = \frac{V_m CP}{(P_0 - P) \left[1 + (C - 1) \frac{P}{P_0} \right]} \quad (14)$$

where:

V_{α} = volume of adsorbed gas at pressure P.

V_m = monolayer volume.

P = gas pressure.

P_0 = saturation gas pressure

The value of parameter C, fairly constant for a given class of materials, e.g. oxides and metals, in simplest terms is given by the following equation:

$$C \propto \exp \frac{(q_1 - q_L)}{RT} \quad (15)$$

where:

q_1 = heat of adsorption of the first layer.

q_L = heat of liquefaction of the adsorptive.

R = gas constant.

T = absolute temperature.

Small values of the C parameter stand for a higher affinity between molecules than between the molecules and the adsorbing species, resulting in lower wettability. On the contrary, high C values describe the typical isotherm, characterized, firstly, by a monolayer adsorption and then by the multilayer one, layer by layer.

Equation (14) can also be written in the linear form:

$$\frac{P}{V_{\alpha} (P_0 - P)} = \frac{1}{V_m C} + \frac{C - 1}{V_m C} \left(\frac{P}{P_0} \right) \quad (16)$$

Chapter IV

Isotherm data for most solids when using nitrogen as the adsorptive and plotting them in according to equation (16) yield a straight line within the range $0.05 < P/P_0 < 0.35$.

From the slope and intercept values of the BET linear plot it is possible to calculate both the amount of adsorbate corresponding to the first monolayer, V_m , and the C parameter can be calculated. Assuming that the surface occupied by a N_2 molecule is $16.2 \cdot 10^{-20} \text{ m}^2$, once calculated V_m , it's easy to obtain the Specific Surface Area (SSA) of the adsorbing material, by the following equation:

$$SSA = \frac{V_m N_A S_{N_2}}{22.414 g} \quad (17)$$

where:

N_A = Avogadro number ($6.023 \cdot 10^{23}$ molecules mol^{-1}).

S_{N_2} = surface occupied by a N_2 molecule adsorbed on the monolayer.

22.414 = volume (dm^3) occupied by 1 mole of gas under standard conditions.

g = sample quantity (g).

Moreover, the C value is most frequently between 50 and 300, when using nitrogen at 77 K. A high or negative C value is indicative of micropores and their measurement cannot be analysed by this BET model without further modification.

IV.2.4 Electron Microscopy

Since its invention, the electron microscope has been a valuable tool in the development of scientific theory and it contributed greatly to biology, medicine and material sciences. This wide spread use of electron microscopes is based on the fact that they permit the observation and characterization of materials on a nanometer (nm) to micrometer (μm) scale. The basic theory for electron microscopy are here shortly presented, focusing on the two basic types of Ems; SEM (Scanning Electron Microscope) and TEM (Transmission Electron Microscope).

Electron Microscopes are scientific instruments that use a beam of highly energetic electrons to examine objects on a very fine scale. This examination can yield information about the topography (surface features of an object), morphology (shape and size of the particles making up the object), composition (the elements and compounds that the object is composed of and the relative amounts of them) and crystallographic information (how the atoms are arranged in the object). Electron Microscopes were developed due

to the limitations of Light Microscopes which are limited by the physics of light to 500x or 1000x magnification with a resolution of 0.2 μm . In the early 1930's this theoretical limit had been reached and there was a scientific desire to see the fine details of the interior structures of organic cells (nucleus, mitochondria...etc.). This required 10,000x plus magnification which was just not possible using Light Microscopes.

The Transmission Electron Microscope (TEM) was the first type of Electron Microscope to be developed and is patterned exactly on the Light Transmission Microscope except that a focused beam of electrons is used instead of light to "see through" the specimen. It was developed by Max Knoll and Ernst Ruska in Germany in 1931. The first Scanning Electron Microscope (SEM) debuted in 1942, with the first commercial instruments around 1965. Its late development was due to the electronics involved in "scanning" the beam of electrons across the sample. Electron Microscopes (EMs) function exactly as their optical counterparts except that they use a focused beam of electrons instead of light to "image" the specimen and gain information as to its structure and composition.

IV.2.4.1 Electron matter interactions

When an electron beam interacts with the atoms in a sample, individual incident electrons undergo two types of scattering - elastic and inelastic. In the former, only the trajectory changes and the kinetic energy and velocity remain constant. In the case of inelastic scattering, some incident electrons will actually collide with and displace different kind of electrons from the specimen, thus losing their kinetic energy. Figure 19 summarizes the main secondary signals (with different relative intensity) that can be produced due to electron-matter interactions.

By considering the large amount of information obtained by this kind of interaction it's essential try to amplify each single signal by using different kinds of instrumentation. In this regard the first main difference between SEM and TEM, mainly concerning the sample location in the microscope, can be outlined. In particular SEM studies the information related to secondary and backscattered electrons, detected on the same side with respect to the incident electrons beam. In this case the sample holder is located at the end of microscope's column (Figure 20a). On the contrary TEM deals with transmitted, elastically or inelastically scattered electrons, detected on the opposite side with respect to the incident electrons beam. In this case the sample holder is located in the middle of the microscope's column (Figure 20b).

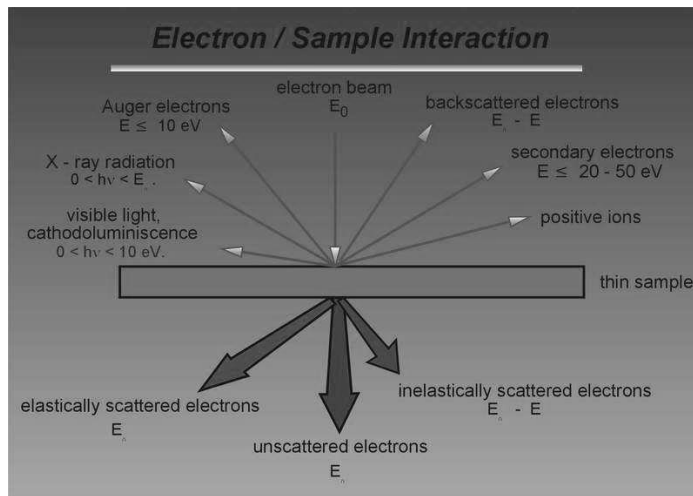


Figure 19 Signals generated when a high-energy beam of electrons interacts with a thin specimen

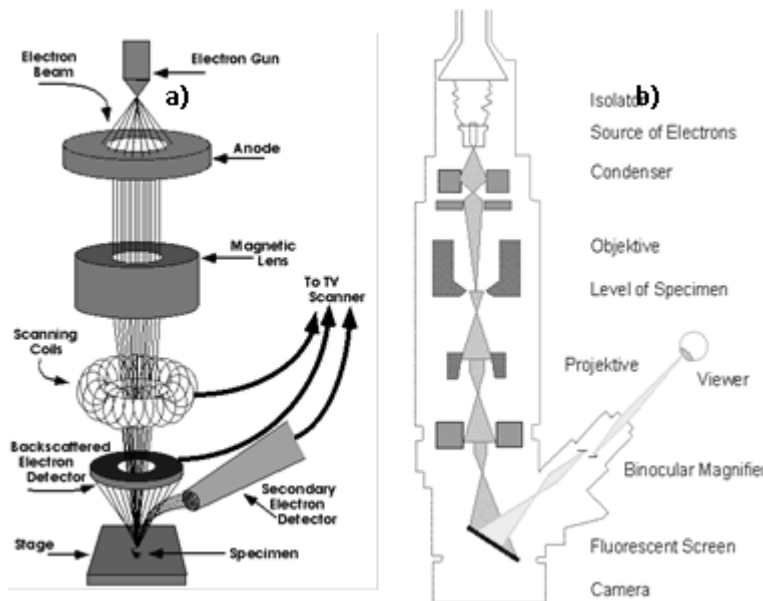


Figure 20 General scheme of a) SEM and b) TEM instrumentations

Both SEM and TEM instruments must work under ultra high vacuum conditions (10^{-7} - 10^{-8} Pa) in order to avoid any kind of collision between the electrons beam and atoms, which are not those contained in the investigated sample. Moreover there are essential instrumental components which are common to SEM and TEM systems: electron guns, which can be divided into thermoionic and field-emission types, and metal apertures and magnetic

lenses necessary to confine and focus the electron beam toward the specimen (thanks to the application of a proper potential).

IV.2.4.2 Electrons exploited in Transmission Electron

Microscopy (TEM)

TEM exploits three different interactions of electron beam-specimen: unscattered electrons (transmitted beam), elastically scattered electrons (diffracted beam) and inelastically scattered electrons. When incident electrons are transmitted through the thin specimen without any interaction occurring inside the specimen, then the beam of these electrons is called transmitted. The transmission of unscattered electrons is inversely proportional to the specimen thickness. Areas of the specimen that are thicker will have fewer transmitted unscattered electrons and so will appear darker; conversely the thinner areas will have more transmitted and thus will appear lighter. Another part of the incident electrons, are scattered (deflected from their original path) by atoms in the specimen in an elastic fashion (without loss of energy). These diffracted electrons according to Bragg's law are then transmitted through the remaining portions of the specimen. In this case a diffraction pattern and the related information about orientation, atomic arrangements and phases present in the examined area can be obtained. There are essentially three different imaging modes in TEM, which can be selected by changing proper apertures of the back focal plane (after the objective lens) (Figure 21):

1. Bright field mode: the aperture selects only transmitted electrons. In this case, factors such as mass and thickness of the sample influence the formation of the image.

2. Dark field mode: in this case only diffracted electrons, which gave strong interaction with the sample, are selected. The image obtained can give information about the presence of defects or different phases of the specimen.

3. High resolution (HR-TEM): in this case both transmitted and diffracted electrons are selected. Using proper corrections for spherical aberration, special high resolution TEMs can generate images with a resolution below 0.1 nm; it's thus possible observe reticular planes and get crystallographic information of the examined sample. By considering that for TEM analysis the analyzed electrons have to pass through the sample, the specimens have to be rather thin, less than 100 nm.

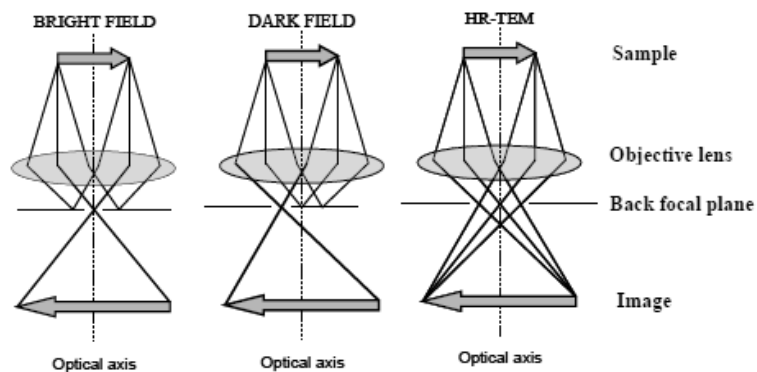


Figure 21 Generalized description of the three main imaging modes in TEM.

IV.2.6 Temperature Programmed Reduction (TPR)

The purpose of the TPR technique is to determine the behaviour of the catalyst, in relation to its reducibility. The calcined samples were subjected to reduction in programmed temperature in the same laboratory plant developed for the shift reaction, described in more details later. The catalysts were reduced using a stream of 5% by volume of H_2 in N_2 with a GHSV of 15000 h^{-1} . The set temperature program includes a step of heating by T_{amb} up to 600°C , with a speed of $10^\circ\text{C}/\text{min}$, and a step isotherm at 600°C for a period of 1h.

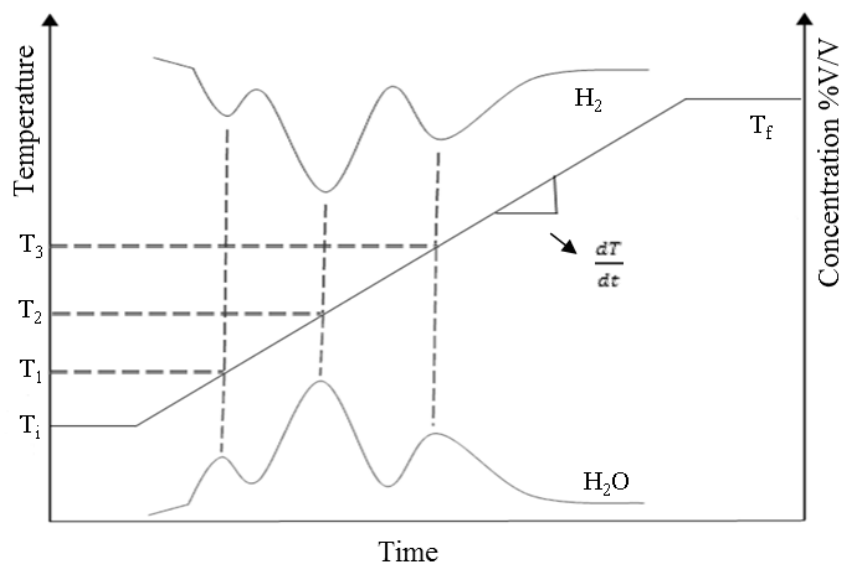


Figure 22 Curve Concentration-Temperature-Time obtained by a TPR

In the course of the TPR, in correspondence of specific temperatures, oxidation-reduction reactions occur, which involve a constituent of the test sample, generally the active species, and the hydrogen:



The amount of consumed hydrogen is, in principle, equivalent to the moles of water produced.

The results of this test characterization are typically reported in a graph Concentration/temperature against time, as shown in Figure 22.

- qualitative information: based on the number of peaks obtained, not only the number and type of reducible species present can be determined, but also their oxidation state and their temperature reduction;

- quantitative information: it is possible to determine the quantity of the sample reduced by calculating the moles of H_2 consumed, through the integration of the peak area.

IV.2.7 Raman Spectroscopy

The Raman spectroscopy measures the vibrational motions of a molecule like the infrared spectroscopy. The physical method of observing the vibrations is, however, different from the infrared spectroscopy. In Raman spectroscopy one measures the light scattering while the infrared spectroscopy is based on absorption of photons. The Raman phenomenon was detected in 1928 by the Indian physicist Sir Chandrasekhara Venkata Raman and Kariamanikkam Srinivasa Krishnan.¹² Independently of this work, the phenomenon was also reported by Grigory Landsberg and Leonid Mandelstam. However, the phenomenon was predicted theoretically even earlier by using the classical model. After the end of 1920's the method was forgotten for several decades because the signal is very weak. Raman spectroscopy experienced a renaissance in the 1960's when the lasers were invented and started to be used as light sources in spectroscopy. The basics of the Raman scattering can be explained using classical physics but a more comprehensive theory requires quantum mechanical treatise. Both the classical and quantum mechanical formulations are sketched below.

When light interacts with matter, the photons which make up the light may be absorbed or scattered, or may not interact with the material and may pass straight through it. If the energy of an incident photon corresponds to the energy gap between the ground state of a molecule and an excited state, the photon may be absorbed and the molecule promoted to the higher energy excited state. It is this change which is measured in absorption spectroscopy by the detection of the loss of that energy of radiation from the light. However, it is also possible for the photon to interact with the molecule and

Chapter IV

scatter from it. In this case there is no need for the photon to have an energy which matches the difference between two energy levels of the molecule. The scattered photons can be observed by collecting light at an angle to the incident light beam, and provided there is no absorption from any electronic transitions which have similar energies to that of the incident light, the efficiency increases as the fourth power of the frequency of the incident light. Scattering is a commonly used technique. For example, it is widely used for measuring particle size and size distribution down to sizes less than 1 μm . One everyday illustration of this is that the sky is blue because the higher energy blue light is scattered from molecules and particles in the atmosphere more efficiently than the lower energy red light. However, the main scattering technique used for molecular identification is Raman scattering. The process of absorption is used in a wide range of spectroscopic techniques. For example it is used in acoustic spectroscopy where there is a very small energy difference between the ground and excited states and in X-ray absorption spectroscopy where there is a very large difference. In between these extremes are many of the common techniques such as NMR, EPR, infrared absorption, electronic absorption and fluorescence emission, and vacuum ultraviolet (UV) spectroscopy. Radiation is often characterized by its wavelength (λ). However, in spectroscopy, because we are interested in the interaction of radiation with states of the

molecule being examined and this being usually discussed in terms of energy, it is often useful to use frequency (ν) or wavenumber ($\bar{\nu}$) scales, which are linearly related with energy:

$$\lambda = \frac{c}{\nu} \quad (19)$$

$$\nu = \frac{\Delta E}{h} \quad (20)$$

$$\bar{\nu} = \frac{1}{\lambda} \quad (21)$$

It is clear from Equations 19-21 that the energy is proportional to the reciprocal of wavelength and therefore the highest energy region is on the left in Figure 23 and the longest wavelength on the right. The way in which radiation is employed in infrared and Raman spectroscopies is different. In infrared spectroscopy, infrared energy covering a range of frequencies is directed onto the sample. Absorption occurs where the frequency of the incident radiation matches that of a vibration so that the molecule is promoted to a vibrational excited state. The loss of this frequency of radiation from the beam after it passes through the sample is then detected. In contrast, Raman spectroscopy uses a single frequency of radiation to

irradiate the sample and it is the radiation scattered from the molecule, one vibrational unit of energy different from the incident beam, which is detected. Thus, unlike infrared absorption, Raman scattering does not require matching of the incident radiation to the energy difference between the ground and excited states. In Raman scattering, the light interacts with the molecule and distorts (polarizes) the cloud of electrons round the nuclei to form a short-lived called a ‘virtual state’.

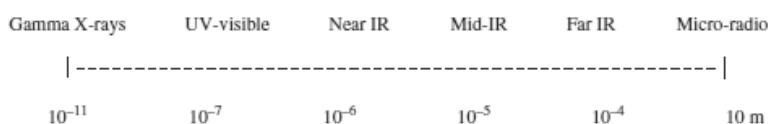


Figure 23 The electromagnetic spectrum on the wavelength scale in meters

This state is not stable and the photon is quickly re-radiated. The energy changes we detect in vibrational spectroscopy are those required to cause nuclear motion. If only electron cloud distortion is involved in scattering, the photons will be scattered with very small frequency changes, as the electrons are comparatively light. This scattering process is regarded as elastic scattering and is the dominant process. For molecules it is called Rayleigh scattering. However, if nuclear motion is induced during the scattering process, energy will be transferred either from the incident photon to the molecule or from the molecule to the scattered photon. In these cases the process is inelastic and the energy of the scattered photon is different from that of the incident photon by one vibrational unit. This is Raman scattering. It is inherently a weak process in that only one in every $10^6 - 10^8$ photons which scatter is Raman scattered. In itself this does not make the process insensitive since with modern lasers and microscopes, very high power densities can be delivered to very small samples but it does follow that other processes such as sample degradation and fluorescence can readily occur.

Figure 24 shows the basic processes which occur for one vibration. At room temperature, most molecules, but not all, are present in the lowest energy vibrational level. Since the virtual states are not real states of the molecule but are created when the laser interacts with the electrons and causes polarization, the energy of these states is determined by the frequency of the light source used. The Rayleigh process will be the most intense process since most photons scatter this way. It does not involve any energy change and consequently the light returns to the same energy state. The Raman scattering process from the ground vibrational state m leads to absorption of energy by the molecule and its promotion to a higher energy excited vibrational state (n) . This is called Stokes scattering.

Chapter IV

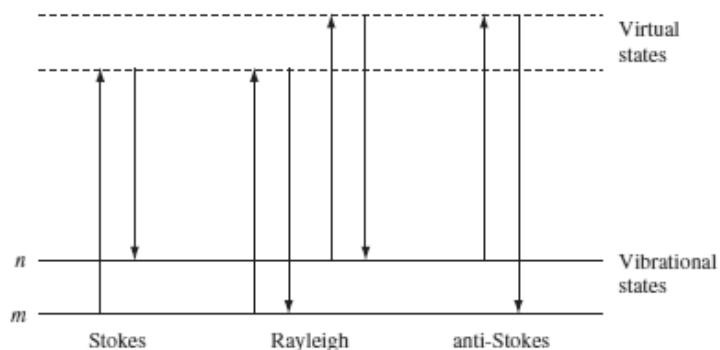


Figure 24 Diagram of the Rayleigh and Raman scattering processes. The lowest energy vibrational state m is shown at the foot with states of increasing energy above it. Both the low energy (upward arrows) and the scattered energy (downward arrows) have much larger energies than the energy of a vibration.

However, due to thermal energy, some molecules may be present in an excited state such as n in Figure 24. Scattering from these states to the ground state m is called anti-Stokes scattering and involves transfer of energy to the scattered photon. The relative intensities of the two processes depend on the population of the various states of the molecule. The populations can be worked out from the Boltzmann equation but at room temperature, the number of molecules expected to be in an excited vibrational state other than any really low-energy ones will be small.

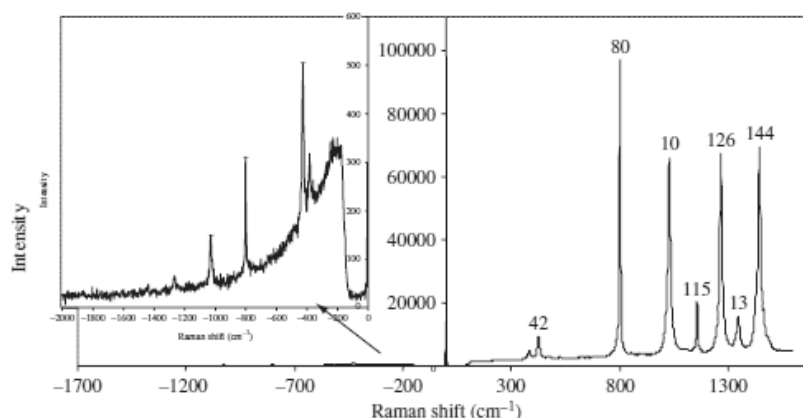


Figure 25 Stokes and anti-Stokes scattering for cyclohexane. To show the weak anti-Stokes spectrum, the y-axis has been extended in the inset

Thus, compared to Stokes scattering, anti-Stokes scattering will be weak and will become weaker as the frequency of the vibration increases, due to decreased population of the excited vibrational states. Further, anti-Stokes

scattering will increase relative to Stokes scattering as the temperature rises. Figure 25 shows a typical spectrum of Stokes and anti-Stokes scattering from cyclohexane separated by the intense Rayleigh scattering which should be offscale close to the point where there is no energy shift. However there is practically no signal close to the frequency of the exciting line along the x-axis. This is because filters in front of the spectrometer remove almost all light within about 200 cm^{-1} of the exciting line. Some breakthrough of the laser light can be seen where there is no energy shift at all.

Usually, Raman scattering is recorded only on the low-energy side to give Stokes scattering but occasionally anti-Stokes scattering is preferred. For example, where there is fluorescence interference, this will occur at a lower energy than the excitation frequency and consequently anti-Stokes scattering can be used to avoid interference. The difference in intensities of Raman bands in Stokes and anti-Stokes scattering can also be used to measure temperature Figure 24 illustrates one key difference between infrared absorption and Raman scattering. As described above, infrared absorption would involve direct excitation of the molecule from state m to state n by a photon of exactly the energy difference between them. In contrast, Raman scattering uses much higher energy radiation and measures the difference in energy between n and m by subtracting the energy of the scattered photon from that of the incident beam (the two vertical arrows in each case). The cyclohexane spectrum in Figure 25 shows that there is more than one vibration which gives effective Raman scattering (i.e. is Raman active). However, there is a basic selection rule which is required to understand this pattern. Intense Raman scattering occurs from vibrations which cause a change in the polarizability of the electron cloud round the molecule. Usually, symmetric vibrations cause the largest changes and give the greatest scattering. This contrasts with infrared absorption where the most intense absorption is caused by a change in dipole and hence asymmetric vibrations which cause this are the most intense. As will be seen later, not all vibrations of a molecule need, or in some cases can, be both infrared and Raman active and the two techniques usually give quite different intensity patterns. As a result the two are often complementary and, used together, give a better view of the vibrational structure of a molecule.

One specific class of molecule provides an additional selection rule. In a centrosymmetric molecule, no band can be active in both Raman scattering and infrared absorption. This is sometimes called the mutual exclusion rule. In a centrosymmetric molecule, reflection of any point through the centre will reach an identical point on the other side (C_2H_4 is centrosymmetric, CH_4 is not). This distinction is useful particularly for small molecules where a comparison of the spectra obtained from infrared absorption and Raman scattering can be used to differentiate cis and trans forms of a molecule in molecules such as a simple azo dye or a transition metal complex.

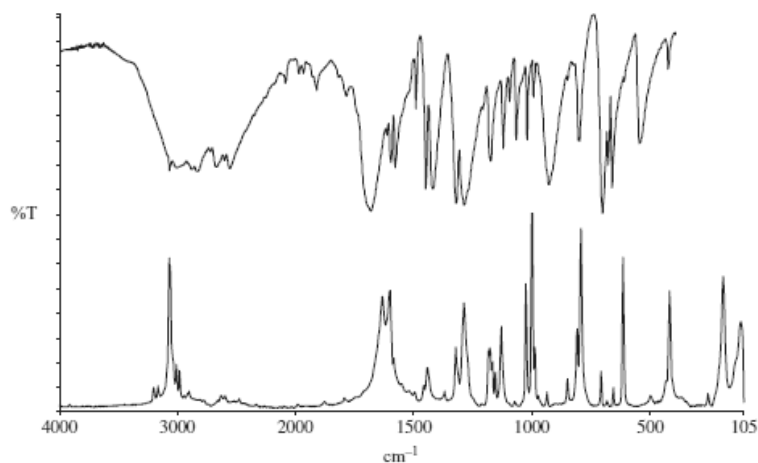


Figure 26 Infrared and Raman spectra of benzoic acid. The top trace is infrared absorption given in % transmission (%T) so that the lower the transmission value the greater the absorption. The lower trace is Raman scattering and the higher the peak the greater the scattering

Figure 26 a comparison of the infrared and Raman spectra for benzoic acid. The x-axis is given in wavenumbers for which the unit is cm^{-1} .

Wavenumbers are not recommended SI units but the practice of spectroscopy is universally carried out using these and this is unlikely to change. For infrared absorption each peak represents an energy of radiation absorbed by the molecule. The y-axis gives the amount of the light absorbed and is usually shown with the maximum absorbance as the lowest point on the trace. Raman scattering is presented only as the Stokes spectrum and is given as a shift in energy from the energy of the laser beam. This is obtained by subtracting the scattered energy from the laser energy. In this way the difference in energy corresponding to the ground and excited vibrational states (n and m Figure 24) is obtained. This energy difference is what is measured directly by infrared. The scattering is measured as light detected by the spectrometer and the maximum amount of light detected is the highest point on the trace

Strictly speaking, Raman scattering should be expressed as a shift in energy from that of the exciting radiation and should be referred to as Δcm^{-1} but it is often expressed simply as cm^{-1} . This practice is followed in this book for simplicity. Although different energy ranges are possible, the information of interest to most users is in the $3600\text{--}400\text{ cm}^{-1}$ (2.8–12 micron) range in infrared spectroscopy and down to 200 cm^{-1} in Raman spectroscopy since this includes most modes which are characteristic of a molecule. In some applications, much larger or smaller energy changes are studied and modern Raman equipment can cope with much wider ranges. One specific advantage of Raman scattering is that shifts from the laser line of 50 cm^{-1} or

lower can easily be recorded with the correct equipment. Many modern machines for reasons of cost and simplicity are not configured in a suitable way to measure shifts below $100\text{-}200\text{ cm}^{-1}$. The intensities of the bands in the Raman spectrum are dependent on the nature of the vibration being studied and on instrumentation and sampling factors. Modern instruments should be calibrated to remove the instrument factors but this is not always the case; these factors are dealt with in the next chapter. Sampling has a large effect on the absolute intensities, bandwidths observed and band positions. Again these will be dealt with later. This chapter will concentrate on the effect on Raman scattering of the set of vibrations present in a molecule and set out a step-by-step approach to interpretation based on simple selection rules.

IV.3 Water Gas Shift (WGS) tests

In order to accurately investigate the catalysts performances, a set of experimental tests was established, for all the proposed samples.

IV.3.1 Activity and Selectivity tests

First of all, the catalytic activity was studied through experiments in the temperature range $150\text{-}400^\circ\text{C}$, with the following composition of the feed mixture: 5% vol CO / 25% vol H_2O / 70% vol He. The molar feed ratio of water-to-carbon monoxide was, therefore, equal to 5, while the space velocity GHSV (gas hourly space velocity) was equal to 5000 h^{-1} , referred to standard conditions (STP), in correspondence of each value of temperature in the range of interest. The activity of the catalysts was tested in a fixed bed tubular stainless steel reactor having an internal diameter of 18 mm. All the samples were crushed into powder and sieved ($180\text{-}355\text{ }\mu\text{m}$) to reach 6 cm^3 of catalyst, diluted 1:1 vol with quartz ($500\text{-}700\text{ }\mu\text{m}$), in order to minimize the pressure drops and the thermal effect of the exothermic reaction.

Each activity test provided continuous monitoring of the concentrations of the substances from the reactor outlet after checking the feed composition in by-pass. The flow of water sent to the reactor was controlled gravimetrically, therefore, the concentrations of other substances were read by the analyzer on a dry basis. In this way, for each value of temperature, the trend function of time of the concentration of gaseous products was obtained, from which the conversions of the reactants, the hydrogen yield and the selectivity towards the products could be calculated. The composition of the mixture leaving the reactor at each temperature was defined by the average concentration of each product; it is, in this case, the compositions of the mixture at steady state. Therefore, the composition of the products mixture has also been reported as a function of temperature, in

Chapter IV

order to know the effect of this parameter on the performance of the samples.

IV.4 Laboratory plant used for the activity tests

The experimental tests were conducted in a lab scale plant, schematized in Figure 27, consisting in 3 main sections:

1. Feed section
2. Reaction section
3. Analysis section

The experimental apparatus was available in Proceed lab – Industrial Chemistry and Catalysis lab – in the Department of Industrial Engineering of the University of Salerno.

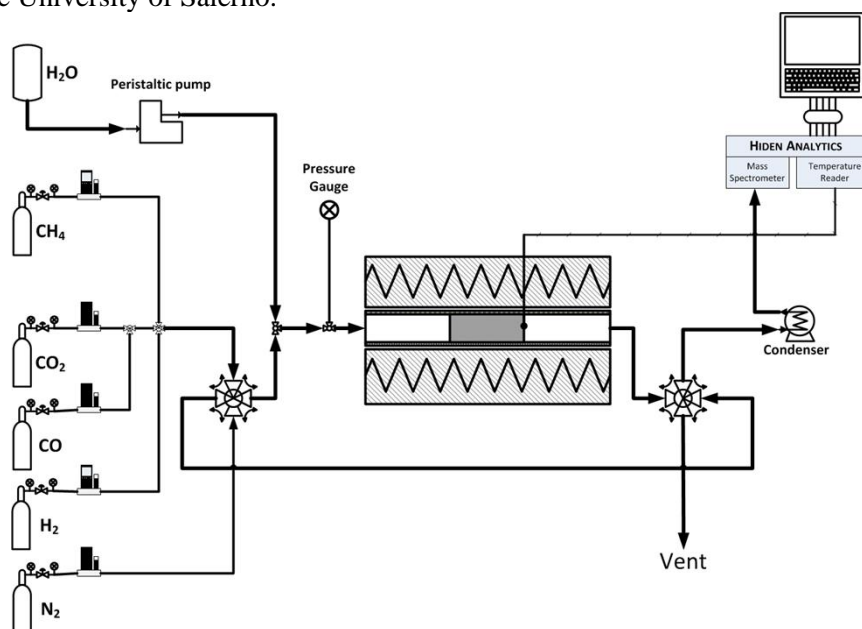


Figure 27 Experimental set-up

IV.4.1 Feed section

Gaseous reactant delivery was assured by means of a series of mass flow controllers (MFC). A series of pure gases (precision gas purity), supplied by SOL S.p.a, was used to calibrate analysis system. A couple of 4-way valves allows delivered stream to by-pass reaction system, for preliminary calibration operations. In this phase, an equivalent He stream was fed to the reactor, in order to stabilize temperature in the initial period of the catalytic tests, assuring a constant heat flux.

In the case of water, a “Watson-Marlowe” peristaltic pump was used to feed it directly into the reactor. Of course, water was feed as liquid, so it had to be vaporized before entering in contact with the catalytic bed.

IV.4.2 Reaction section

Reaction tests are conducted by using a tubular stainless steel reactor.

It is inserted in an adiabatic electrical oven, to assure reactions in isothermal conditions.

IV.4.2.1 Electrical oven

Reaction temperature control is realized by placing the reactor in a 4kW annular oven, supplied by “Officina Elettromeccanica Mormile”: it consists of an open oven with 3 heating sections, each driven by means of a TLK38 controller that allows to realize a controlled heat changing in the reaction system; the temperatures in the different sections are measured through 3 thermocouples, able to measure temperature on the external wall of the reactor. In Figure 28 a screenshot of the oven is reported.



Figure 28 Oven used in experimental set-up

Oven wall are realized in ceramic material, to avoid high axial and radial temperature gradients, so improving isothermal behavior. The oven has an

Chapter IV

inner channel of 55 mm diameter, in order to easily place the reactor. A relevant amount of quartz wool was placed around the reactor at inlet and outlet of the oven, in order to minimize thermal dispersion in the surrounding, and to assure a coaxial alignment between reactor and oven channel.

The electrical oven should be able to assure a constant reaction temperature (up to 600°C) inside the reactor, and to hold a flat axial thermal profile. Therefore, before start catalytic tests, oven thermal profile was verified, by setting oven zone controllers to 600°C and by sliding a k-type thermocouple along the oven channel. The achieved results are summarized in Figure 29.

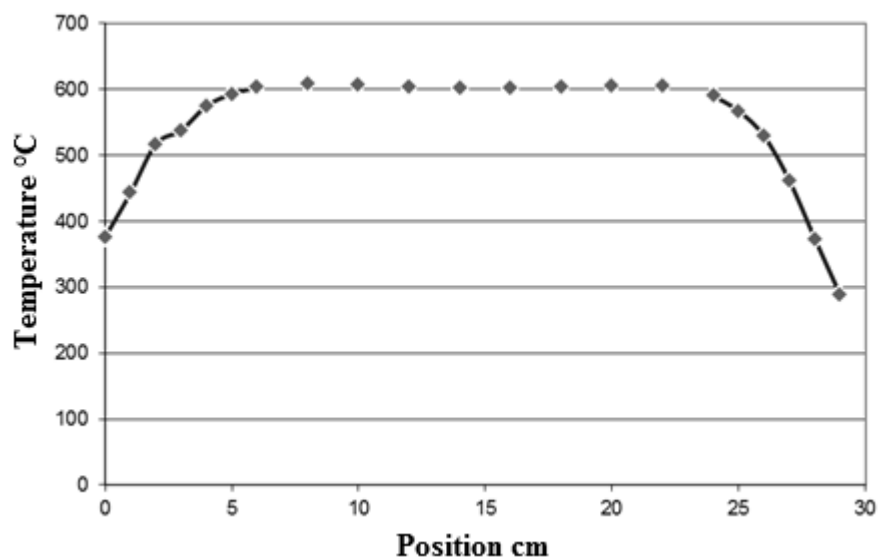


Figure 29 Temperature profile along the empty reactor

As reported in the diagram, the electrical oven shows a wide isothermal zone. In fact, apart the external 6 cm, there is a 18 cm length zone in which temperature appears constant: this is the zone in which catalyst should be placed, to assure an effective isothermal reaction.

However, it is important to underline that thermal profile was verified without any flux or chemical reactions. In the facts, a reaction mixture will be delivered at room temperature inside the oven, and simultaneously an endothermic reaction occurs. Therefore the oven should be able, at same time, to supply the heat needed to reactants preheating and to sustain chemical reaction exothermicity.

IV.4.2.2 Stainless steel tubular reactor

A tubular AISI 310 stainless steel reactor was designed and realized, with a length of 38 cm, inner diameter of 18 mm and wall thickness of 4 mm (Figure 30); the two ends are fixed by a Swagelok type connection, in order to allow relatively high operative pressure as well as easy disassembling procedure. AISI 310 stainless steel is suitable to operating conditions at high temperature in both oxidant and reducing environment. To evaluate the real reaction conditions, reaction system was provided with devices to measure pressure and temperature.

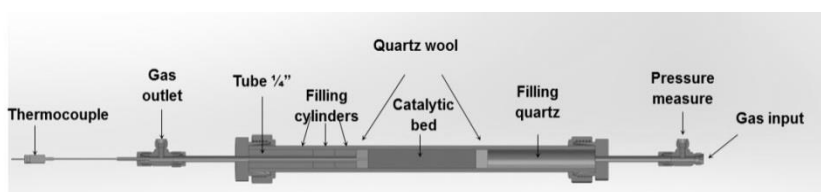


Figure 30 Reacting system

In the inner zone the feed line is provided; by means of a tee connection, the feed line is linked to a pressure transducer, to monitoring pressure upstream the catalytic bed. By checking that downstream the catalytic bed in tests conditions the pressure is 1 bar, the upstream pressure measuring allows to evaluate the pressure drop along the catalyst. Water, as already disclaimed, is fed by means of another stream, which is send directly to the reactor, after passing through a narrow serpentine, in order to ensure a complete vaporization before entering the catalytic section. Furthermore, there is also the possibility to insert a K-type thermocouple with the aim of measuring the reagents inner temperature.

The outside zone is linked to the analysis system; also, a K-type thermocouple was inserted inside the reactor, to measure the temperature in the centre of the catalyst out section.

Powder catalyst was diluted with quartz powder in a ratio 1:1, to reduce pressure drop and to avoid catalyst packing. The catalyst is so inserted in the reactor and locked between 2 quartz wool disks.

IV.4.3 Analysis section

The products stream analysis was assured by a Hiden Analytical mass spectrometer (Figure 31). This device assures a continuous stream scanning, with a composition response every 7 seconds. Moreover, this instrument is able to import the reaction temperature signal, so obtaining a very comprehensive outlook of the system behavior.



Figure 31 Mass spectrometer

The Hiden Analytical mass spectrometer was equipped with a detector able to detect up to 50 AMU. Therefore, in order to analyze the composition of all possible products stream components, the following masses were monitored (Table 6):

Table 6 Scanned Masses

<i>AMU</i>	<i>Compound</i>
2	H ₂
4	He
15	CH ₄
28	CO
44	CO ₂

Before the analysis section, products stream passed through a cold trap to remove water.

IV.5 Tests made on the more active catalyst

The catalyst showing the best performances in this initial screening was then tested under different flowing condition (at different GHSV), and also its stability was investigated. The tests were carried out in a stainless steel tubular reactor with annular geometry, the same reactor as described above for the WGS activity and selectivity tests.

The influence of contact time on CO conversion was studied by varying the gas hourly space velocity from 6,000 h⁻¹ up to 51,000 h⁻¹. The reactants mixture consisted of 8 % CO, 30 % H₂O and N₂ balance and the temperature was set up to 225°C.

Finally, a stability test was made up at a temperature of 200°C on a reactants mixture containing 8 % CO, 30 % H₂O and N₂ balance, with a GHSV = 15,000 h⁻¹.

Chapter V. Heat transfer tests: choice of the best structured carrier

V.1 Heat transfer tests results: thermal profiles

Solid temperature profiles of tested samples are reported in Figure 32. In particular, here it is shown the condition in which the oven temperature is set up to 400 °C and the gas flow rate are 1.2 and 2.4 Ndm³/min. All the other conditions, in the investigated range, showed qualitatively the same behavior.

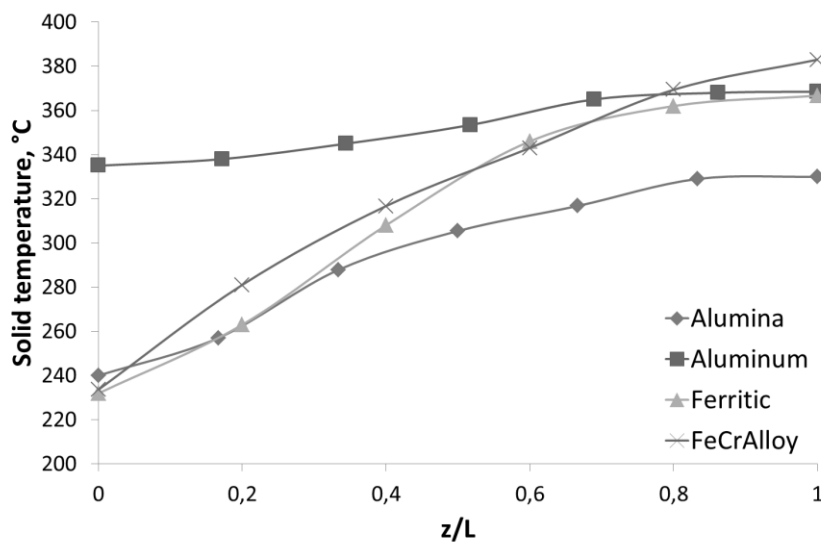


Figure 32 Solid temperature (operating conditions: $T_{oven} = 200^{\circ}\text{C}$, $Q_{tot} = 2.4$ l/min)

The solid temperature profiles of the samples reflect in some way the thermal conductivity of themselves, as will be specified in more details in the section relative to the mathematical model results (V.2 Mathematical Model). As a matter of fact, Aluminum foam showed the most flat thermal profile, sign of a good redistribution of the heat along the monolithic bed. As evidence of this, the outlet temperature of this foam is even lower than other samples' one, such as the FeCr-Alloy and the ferritic foam, in which the difference between inlet and outlet temperatures is very large. The alumina foam also showed a quite flat thermal profile, in fact the thermal conductivity calculated for this sample is much greater than ferritic and FeCr-Alloy foams and about a half of the Aluminum foam. Actually, there is another factor that has to be taken into account. In fact, it has to be remembered that the Alumina foam has the highest relative density, which of course contributed to enhance its thermal conductivity with respect to the other samples. The influence of the material's thermal conductivity can be observed also if looking at the gas temperature profiles Figure 33.

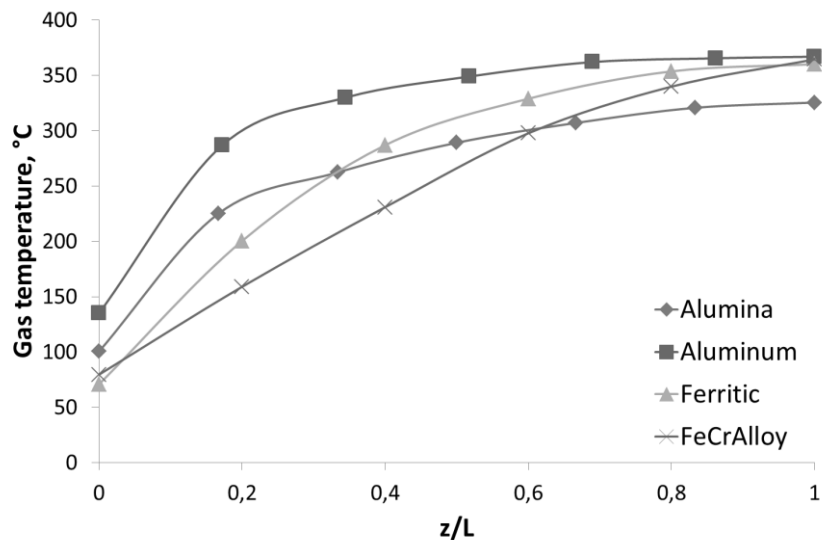


Figure 33 Gas temperature (operating conditions: $T_{oven} = 400^{\circ}\text{C}$, $Q_{tot} = 2.4$ l/min)

Also in this case the qualitative behaviour is similar in all the conditions. Here it can be noticed that the more conductive foams are those who guarantee an almost flat thermal profile of the gas, surely because they assure a more efficient heat flow along the structured carrier. In fact, looking for example at the Aluminum foam, the gas temperature raised straightaway yet in the inlet zone of the monolithic foam, because the solid temperature of the material is higher also next to the inlet of the foam. The same thing has been observed for the Alumina foam, but in this case the gas temperature

was lower because also the solid temperature was lower. Another factor that can influence the gas heating is of course the pores per inch property, which can enhance the heat transfer by means of an enhancement of the turbulence of the system, and in parallel, higher PPI result in higher exchange area, which still enhance gas-solid heat exchange.

V.2 Mathematical Model

In Table 7 the results of the optimization of the heat transfer model are shown. The model was optimized only for the condition relative to a gas flow rate equal to 2.4 dm³/min; the other data were processed to validate the mathematical model. The optimization of the mathematical model by means of changing the two parameters “foam thermal conductivity” and “gas phase heat transfer coefficient” generated the results available in the figures below, relative to the ERG Duocel Aluminum foam.

Table 7 Parametric optimization of the heat transfer model (volumetric flow rate: 2.4 Ndm³/min).

Sample	T _{ov} , °C	k _{foam} , W/m/K	h _g , W/m ² /K	h, W/m ² /K	Q, W
Alumina	200	16.5	204.1	26.4	5.7
	400	12.7	250.0	31.0	12.1
	600	10.9	291.0	33.0	18.2
Aluminum200	30.0	80.1	80.1	17.7	8.4
	400	60.1	90.3	27.9	15.9
	600	89.7	108.4	33.9	23.8
Ferritic	200	1.6	73.2	20.7	6.4
	400	1.5	96.8	30.0	18.1
	600	1.4	164.1	43.0	24.1
FeCrAlloy200	1.5	81.2	81.2	28.9	6.8
	400	1.8	86.7	33.2	23.9
	600	2.0	91.4	36.0	37.2

As it can be seen from the different plots above (Figure 34-Figure 39), the results of the optimization of the model for the tested Aluminum sample were very good. The continuous lines, which represent the model, fit almost perfectly the experimental data in all the conditions employed in these tests. This could mean that the proposed mathematical model describes well the real phenomenon, and so its results, in terms of thermal properties of the foam, are very reliable.

Here below there are the values of the two model parameters estimated at the various operating conditions.

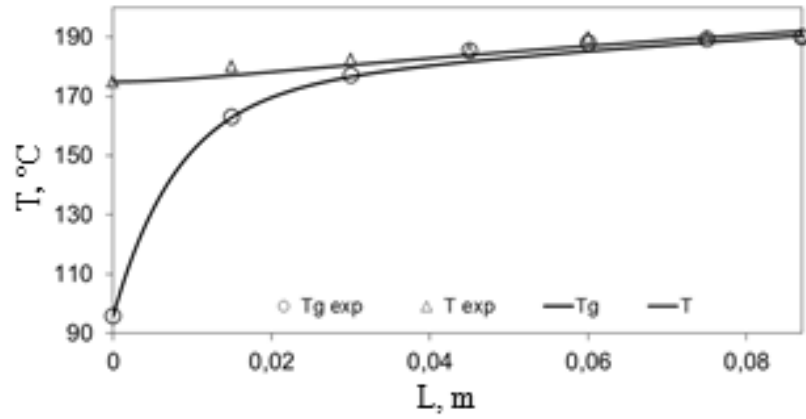


Figure 34 ERG Duocel foam, model optimization (operating conditions: $T_{oven} = 200^{\circ}\text{C}$, $Q_{tot} = 1.2 \text{ l/min}$).

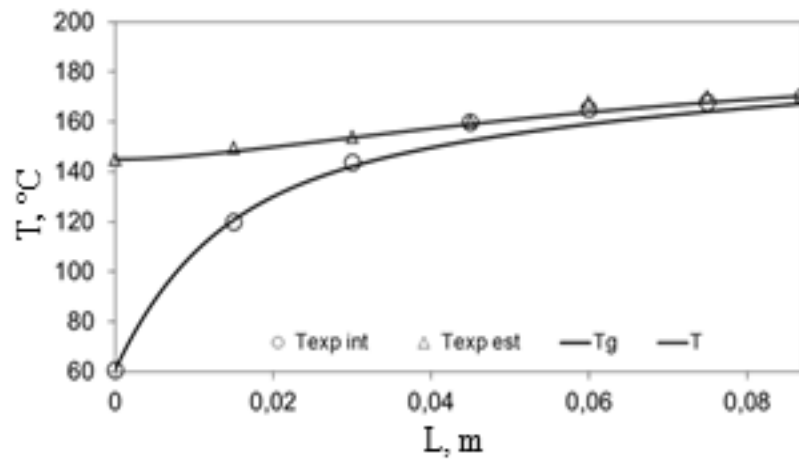


Figure 35 ERG Duocel foam, model optimization (operating conditions: $T_{oven} = 200^{\circ}\text{C}$, $Q_{tot} = 2.4 \text{ l/min}$).

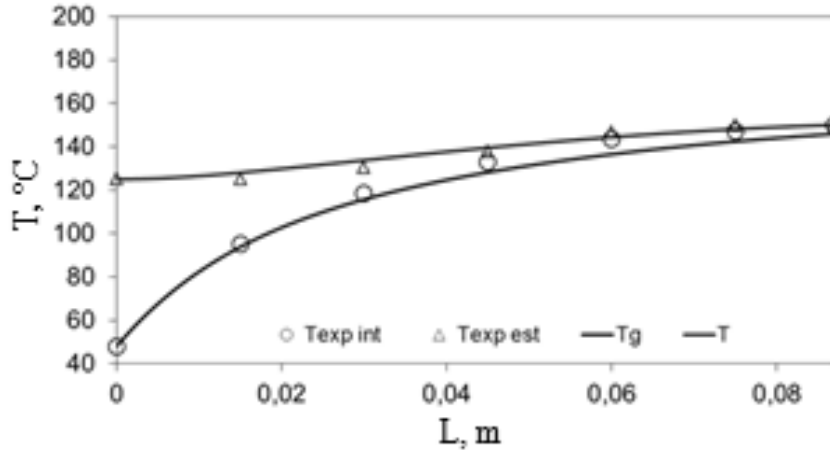


Figure 36 ERG Duocel foam, model optimization (operating conditions: $T_{\text{oven}} = 200^{\circ}\text{C}$, $Q_{\text{tot}} = 3.6 \text{ l/min}$)

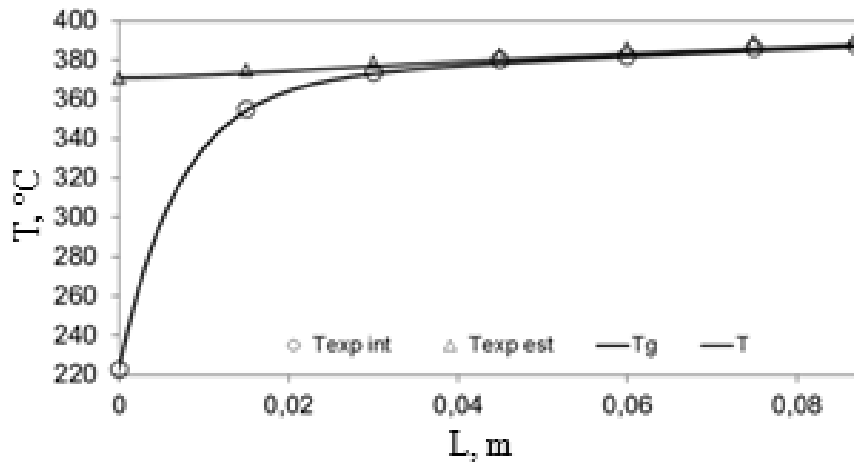


Figure 37 ERG Duocel foam, model optimization (operating conditions: $T_{\text{oven}} = 400^{\circ}\text{C}$, $Q_{\text{tot}} = 1.2 \text{ l/min}$).

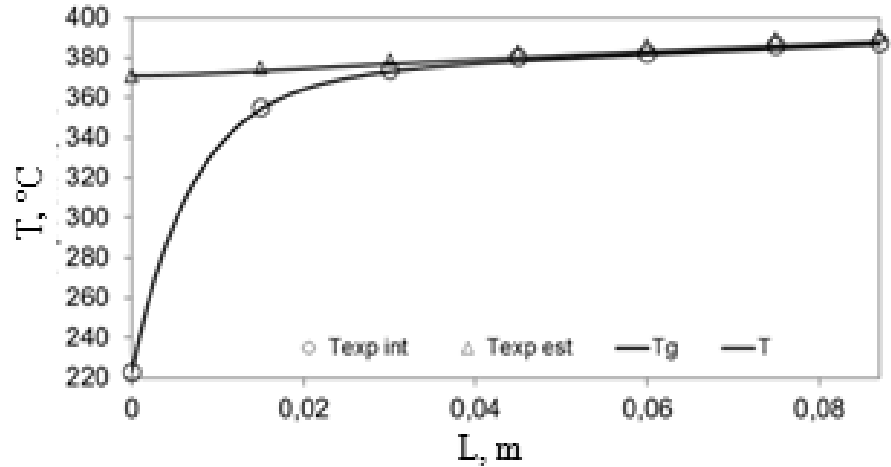


Figure 38 ERG Duocel foam, model optimization (operating conditions: $T_{oven} = 400^{\circ}\text{C}$, $Q_{tot} = 2.4 \text{ l/min}$).

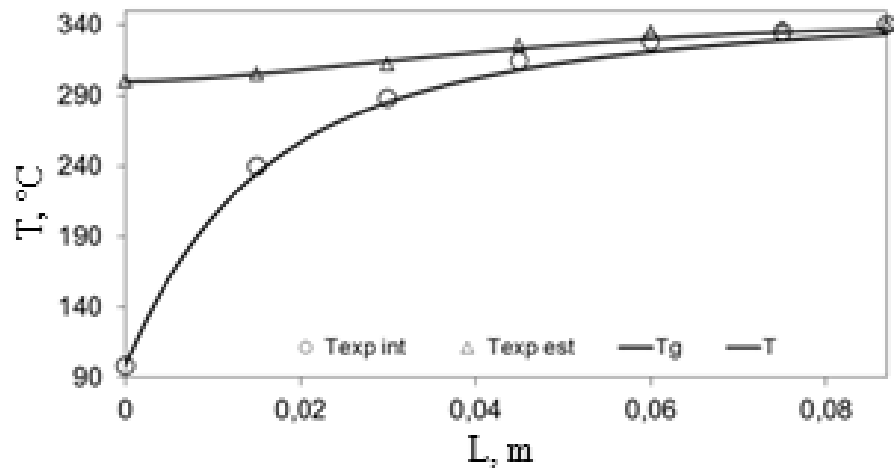


Figure 39 ERG Duocel foam, model optimization (operating conditions: $T_{oven} = 400^{\circ}\text{C}$, $Q_{tot} = 3.6 \text{ l/min}$).

In particular, it can be stated that of course the foam thermal conductivity increased with the temperature, as expected for an aluminum material, while it is constant by varying the flow rate at the same temperature. Moreover, the gas phase heat transfer coefficient tended to increase both with the temperature that with the flow rate. Of course, by increasing the flow rate there is an increasing of the Reynolds number, and so the turbulence is more evident, causing within the foam a better mixing of the gas, and so enhancing the heat exchange.

Furthermore, it is well known that the density of the gas decreases when temperature increases, this causing an increasing of the local gas velocity, still favoring the heat transfer along the bulk of the gas phase.

As a conclusion of this heat transfer study, a comparison between all the samples was made, and this can be seen in Figure 40 and Figure 41 .

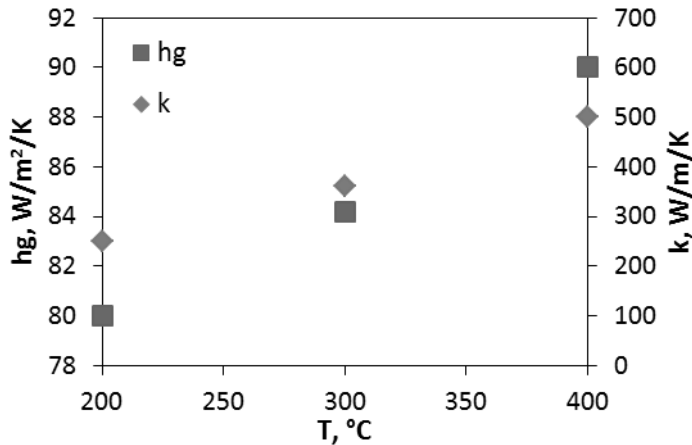


Figure 40 ERG Duocel foam, thermal conductivity coefficient (k) and gas phase heat transfer coefficient (hg) as function of oven temperature

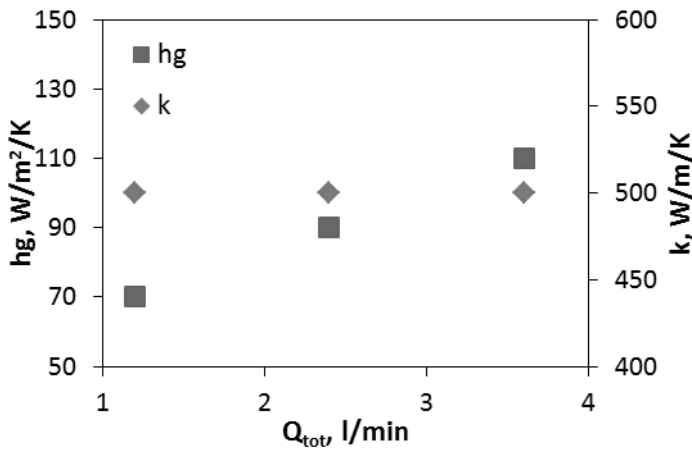


Figure 41 ERG Duocel foam, thermal conductivity coefficient (k) and gas phase heat transfer coefficient (hg) as function of volumetric gas flow rate

As already revealed in the previous sections, the most conductive foam was the Aluminum one, showing a very appreciable thermal conductivity. The Alumina sample showed a quite high k value, but it has to be considered that it also has the highest relative density with respect to the investigated foams. Moreover, in the Figure 42 also the influence of the PPI value can be

Chapter V

noticed. In fact, Alumina foam, which had a sensibly higher PPI value (65 pores per inch) revealed also the highest value of the gas phase heat transfer coefficient, as it could be expected. In conclusion, within the investigated temperature range, Aluminum foam was the most promising structured carrier, showing an excellent heat exchange due to the high thermal conductivity value. This is also reflected on the thermal profile in the gas phase, by promoting a flattening of the profile, increasing the temperature in the inlet zone and decreasing next to the outlet.

These results configure Aluminum foam as a good candidate as a structured carrier for the intensification of processes such as Water Gas Shift.


	FeCr ALLOY	Aluminium Foam	SCHIUMA FERROSA	Al92 Foams
				
h_g	64 W/m ² K	60 W/m ² K	53,5 W/m ² K	204 W/m ² K
$H_{glob.}$	27,5 W/m ² K	13,5 W/m ² K	15,5 W/m ² K	26,5 W/m ² K
K_{foam}	2 W/mK	30 W/mK	1,6 W/mK	17,5 W/mK

Figure 42 Estimated model parameters, comparison between the foam samples.

Chapter VI. Choice of the catalytic phase: Characterization and WGS tests results

VI.1 Characterization results

VI.1.1 Specific surface area (SSA)

In Table 8 the main results of the characterization of the catalysts were reported.

The hexahydroxy platinumic acid (platinum nitrate solution precursor) was analysed by EDXRF to confirm the absence of sodium and by TGA to evaluate the water content.

Table 8 Catalysts characterization: EDXRF Pt content, Specific Surface Area, average crystallites size, TPR H₂ uptake

Sample	Pt %w/w	load.S.S.A. [m ² /g]	Crist. size [nm] (plane)	H ₂ uptake [μmol/g]
γ-Al ₂ O ₃	-	158.4	5.35 (440)	-
14CeAl	-	137.46	6.09 (CeO ₂ (111))	-
Pt14CeAl	1.08	132.3	6.78 (CeO ₂ (111))	134
CeO ₂	-	127.2	5.66 (111)	-
PtCe	0.76	125.7	6.60 (CeO ₂ (111))	983
CeO ₂ -ZrO ₂	-	64.45	7.21 (111)	-
PtCeZr	0.75	65.35	7.22 (CeO ₂ -ZrO ₂ (111))	1205

The specific surface areas recorded for all samples showed that the addition of the active species did not involve a substantial decrease of the s.s.a. The specific surface areas values (Table 8) showed that the loading of ceria on γ-Al₂O₃ support to prepare 14CeAl generated a decreasing of s.s.a., so Pt14CeAl had an s.s.a. only slightly greater than PtCe. This behavior can be observed also Figure 43.

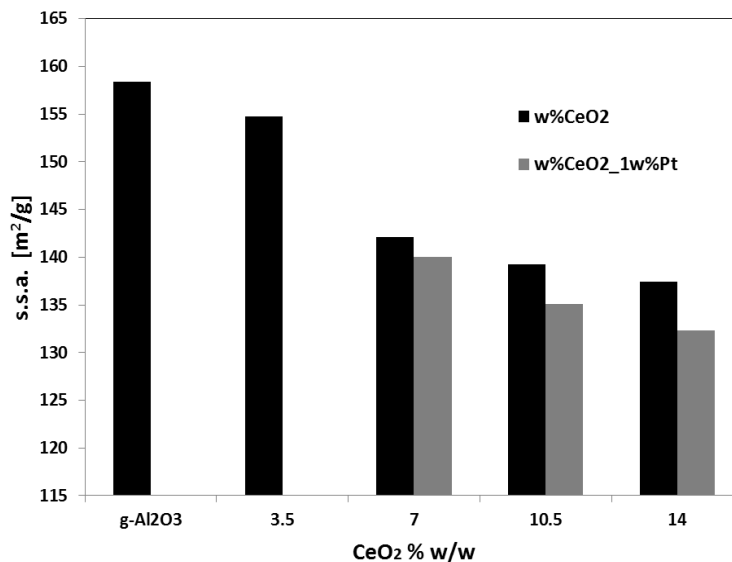


Figure 43 SSA (m^2/g) as function of CeO_2 amount

VI.1.2 X-Ray Diffraction (XRD)

The calcined supports and catalysts were subjected to X-ray diffraction analysis and the results were analyzed by comparing them with the data available in literature. In Figure 44 the diffraction spectrum of 1%Pt/CeO₂, compared to CeO₂ alone, is shown.

Here the characteristic CeO₂ peaks (JCPDS 34-0394) at 28.6, 33.4, 47.8 and 56.7°, corresponding to the reflections in the (1 1 1), (2 0 0), (2 2 0) and (3 1 1) crystalline planes of the cubic fluorite type phase, can be observed (Fu Q., 2003) (Li Y., 2000) (Buitrago R., 2012). As it is clear from the graph, no peak belonging to platinum (the characteristic Pt peak is at 39.9° (Hwang K.-R., 2011)) can be seen; this can be due on the one hand to a too low platinum loading, so that it cannot be detected from the diffractometer, while on the other hand to a good active species dispersion on support surface.

The 1%Pt/CeO₂-ZrO₂ sample is shown in Figure 45. In this case as well, no platinum peak appears in the spectrum. In order to better understand the relation between ceria and zirconia in this latter commercial ceria/zirconia support, a comparison between the two supports is shown in Figure 46.

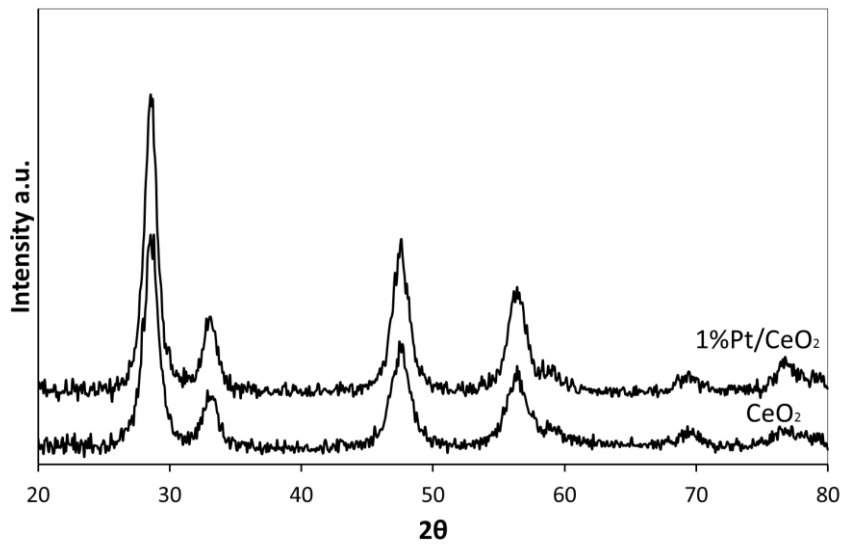


Figure 44 Diffraction spectrum of 1%Pt/CeO₂ sample

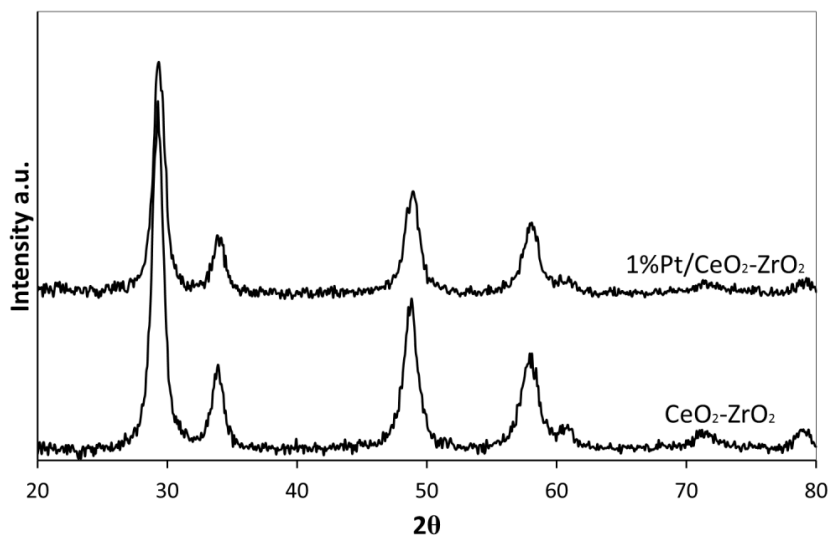


Figure 45 Diffraction spectrum of 1%Pt/CeO₂-ZrO₂ sample

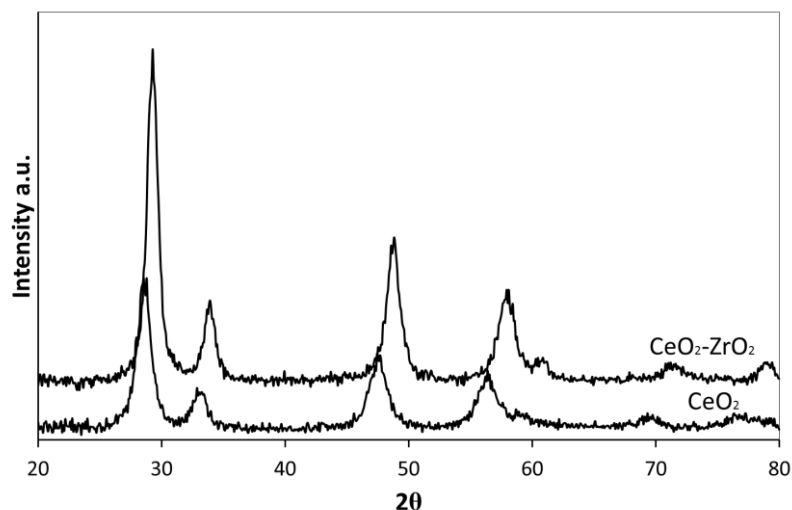


Figure 46 Diffraction spectrum of CeO_2 and $\text{CeO}_2\text{-ZrO}_2$ sample

The XRD diffractogram of the ceria support presented one more time the characteristic cubic fluorite type phase, the main peaks were located (JCPDS 34-0394) at 28.6, 33.4, 47.8 and 56.7°, corresponding to the reflections in the (111), (200), (220) and (311) crystalline planes. The same profile was recorded also in ceria/zirconia diffractogram (Figure 46), however all the peaks appeared shifted towards higher 2θ values, to indicate the formation of a solid solution between ceria and zirconia (Petkovich N. D., 2011). No Platinum peak was observed in all samples, probably due to the too low Platinum loading, below the instrument detection limit. The support crystallites size of the catalysts were determined from X-ray line broadening using the Scherrer equation (Table 9).

Table 9 Crystallite size from Scherrer equation

Sample	Crystallite size, nm
CeO_2	6.1
$\text{CeO}_2\text{-ZrO}_2$	7.2
1%Pt/ CeO_2	6.6
1%Pt/ $\text{CeO}_2\text{-ZrO}_2$	7.2

All the samples had a support average size less than 10 nm. In particular, the Ce and 14CeAl samples showed very similar size, while the CeZr one had a slightly bigger crystallites size. Actually, the addition of the active species caused an increase in the crystallite size of the support for Ce and 14CeAl samples, while no increase was obtained for the ceria-zirconia one. As it can be seen, the crystal dimension of ceria/zirconia solid solution is

slightly higher than ceria. This probably can give a higher oxygen mobility in the support lattice, favouring the WGS activity.

VI.1.3 Raman spectra

Raman spectroscopy was used to probe the local structure. It is a complementary technique to XRD, and is effective at detecting the presence of local inhomogeneity in the samples. While this technique does not yield localized information of crystal structure on the nanoscale, it allows for examination of micrometer-sized spots across a sample.

The Raman spectra of ceria support (Figure 47) show the typical strong band at 464 cm^{-1} attributed to the first order F_{2g} mode of the fluorite type phase, while are barely visible the weak bands at 258 , 595 and $1,179\text{ cm}^{-1}$ respectively attributed to second-order transverse acoustic (2_{TA}), defect-induced (D) and second-order longitudinal optical modes (2_{LO}) (Wu Z., 2010). On the contrary the calcined PtCe derivate shows the growth of the bands at 258 , 595 and $1,179\text{ cm}^{-1}$, the appearance of a broad band at 657 cm^{-1} and a shoulder at 420 cm^{-1} ; the last two bands were attributed to the presence of PtO species (McBride J.R., 1991), besides the band at 595 cm^{-1} could be an overlapping between the D-band of ceria and traces of an amorphous phase of $\alpha\text{-PtO}_2$.

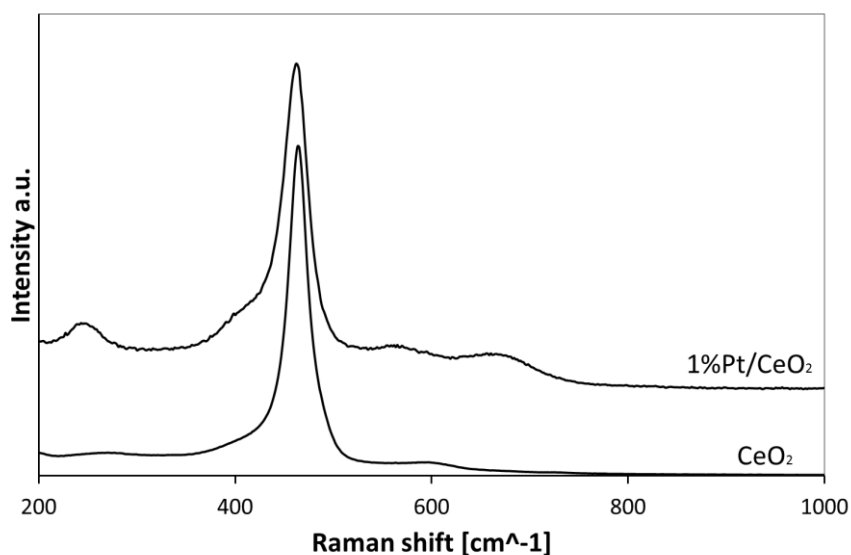


Figure 47 Raman spectrum of 1%Pt/CeO₂ sample

The comparison between the Raman spectra of ceria and ceria-zirconia (Figure 48) showed a significantly distorted structure due to the substitution of some Ce^{4+} ions with the smaller Zr^{4+} ions; so, comparing the data with

Chapter VI

those reported in literature (Ahniyaz A., 2005), we concluded that the $\text{CeO}_2\text{-ZrO}_2$ mixed oxide contained a tetragonal distortion attributable to the metastable t'' phase. The same results were achieved by applying the Bragg formula to the XRD patterns, obtaining a smaller cell parameter for the ceria-zirconia sample (7.3 \AA for CeO_2 and 6.9 \AA for $\text{CeO}_2\text{-ZrO}_2$). Moreover, there is also a peak at 615 cm^{-1} , indicative of distortions in the cubic lattice structure brought by the addition of Zr, and another near 300 cm^{-1} corresponding to the tetragonal space group (Petkovich N. D., 2011). So, it seems that the t'' phase coexists with the cubic phase in this inhomogeneous sample.

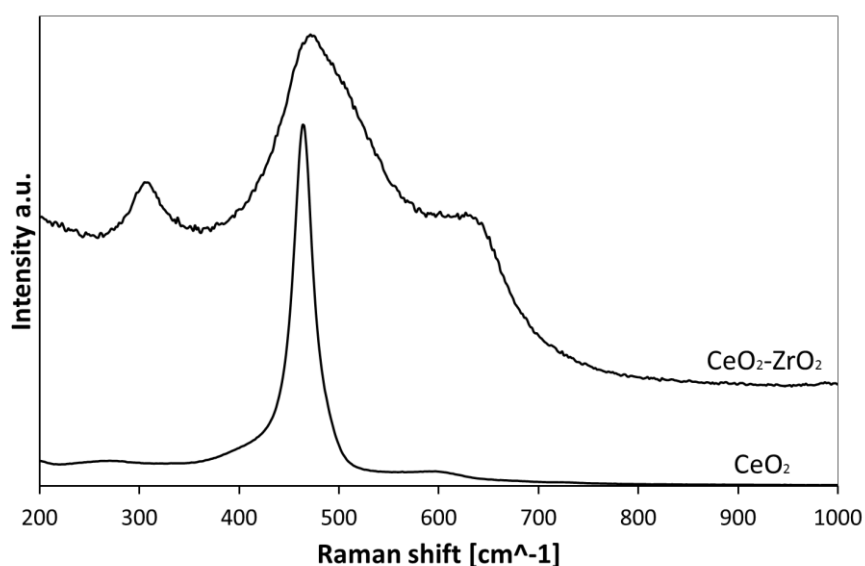


Figure 48 Raman spectrum of $\text{CeO}_2\text{-ZrO}_2$ sample

In addition to the bands of CeZr support the Raman spectra of PtCeZr show also bands at $175, 555 \text{ cm}^{-1}$ similarly to what happened of PtCe (Figure 50). The Raman spectra of 14CeAl (Figure 49) show exclusively the first order band of ceria at 464 cm^{-1} , while the $\text{Pt}14\text{CeAl}$ shows also the two bands at 655 and 550 cm^{-1} , attributed to the PtO_x phases (Lin W., 2008).

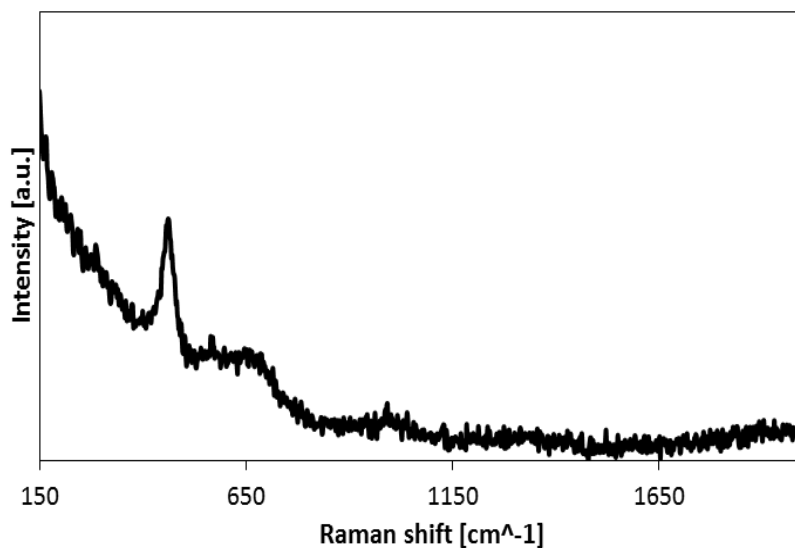


Figure 49 Raman spectrum of 1%Pt/14%CeO₂/γAl₂O₃ sample

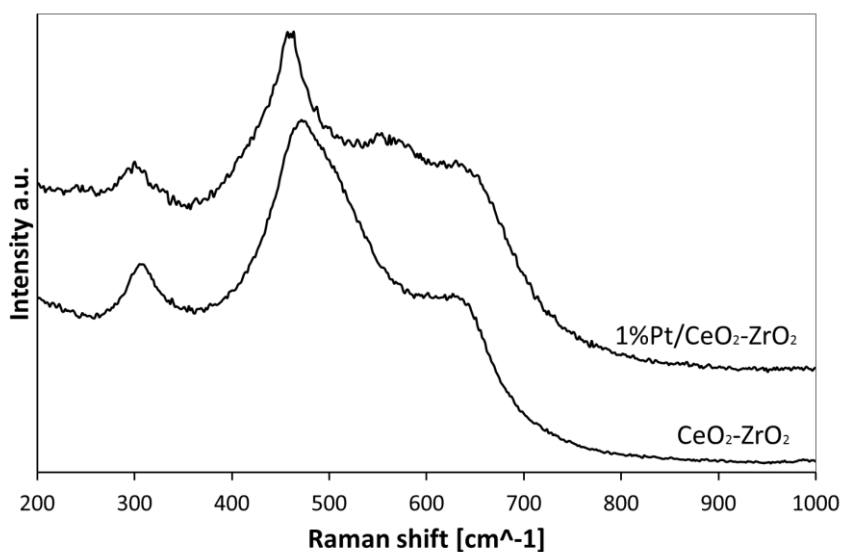


Figure 50 Raman spectrum of 1%Pt/CeO₂-ZrO₂ sample

VI.1.4 Temperature Programmed Reduction (TPR) results

The TPR technique is used not only to study the reducibility of a catalyst, but also to verify eventual improving, or changing, in the reduction

Chapter VI

properties of the catalyst. For ceria water-gas-shift catalysts, the reduction temperature for the surface support is very important, because this corresponds to the temperature at which the active bridging –OH groups are formed, which are crucial for the WGS catalyst activity (Jacobs G., 2005).

Below (Figure 51) the TPR profile of the 1%Pt/CeO₂-ZrO₂ fresh sample is shown.

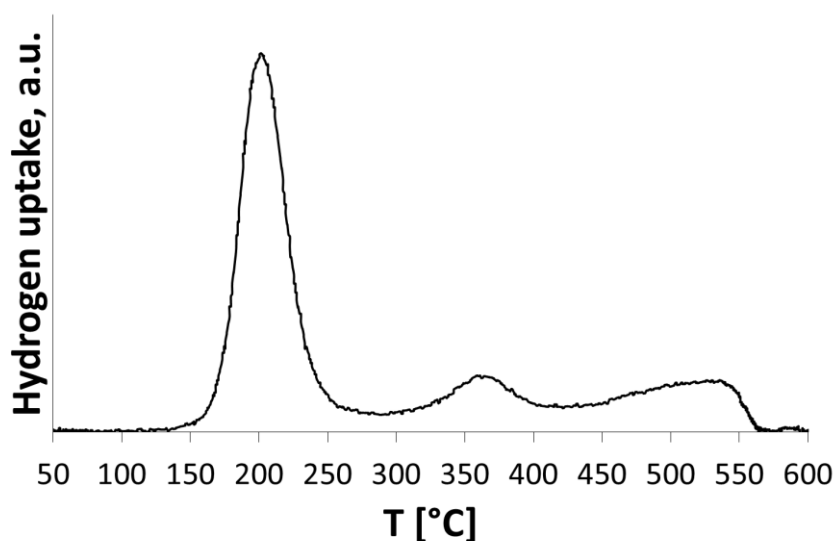


Figure 51 TPR profile of 1%Pt/CeO₂-ZrO₂ sample

As already present in literature, the reduction of ceria in this type of catalyst typically occurs in two steps: the bulk reduction above 750°C, while the surface reduction around 450-550°C (Yao H.C., 1984). In particular, the surface reduction can involve several phenomena: liberation of surface carbonates, reduction of cerium atoms from 4+ to 3+, and the formation of bridging –OH groups.

For the studied sample, the TPR profile shows three main peaks, as shown in Table 10:

Table 10 Main peak of TPR profile

	Centre	Area	Start	Finish
I PEAK	201°C	67.432	120	291.657
II PEAK	360°C	16.904	291.657	421.081
III PEAK	535°C	23737	421.081	585

So, the first peak was attributed to PtO_x species reduction (Ricote S., 2006); this temperature does not correspond to the platinum reduction temperature that is reported in literature (which is 220°C), but this phenomenon is favored by the presence of Zr in the catalyst, which can shift

the platinum reduction temperature to lower temperatures, if zirconium is present in a certain quantity.

The second reduction peak is attributed to zirconium reduction from +4 to +3 oxidation state (Ricote S., 2006), while the third peak was attributed to surface ceria reduction (+4 to +3) (Ricote S., 2006).

Through a deconvolution of the peaks, it was possible to quantify the magnitude of these peaks, which is reported in Figure 52:

Reduction Reaction	Theor. H ₂ [mmol/gcat]	H ₂ uptake [mmol/gcat]	Exp/teor
PtO ₂ + 2 H ₂ → Pt + 2 H ₂ O	0.102520	0.752119211	7.33632
2 ZrO ₂ + H ₂ → Zr ₂ O ₃ + H ₂ O	2.311794	0.188542875	0.08156
2 CeO ₂ + H ₂ → Ce ₂ O ₃ + H ₂ O	2.028023	0.264756402	0.13055

Figure 52 Magnitude of peak obtained from the deconvolution elaboration

By observing this table, what immediately stands out in the eyes is the huge gap between the experimental hydrogen consumption of the first peak and the theoretically expected one. Actually, this is a phenomenon quite common in noble metal based catalysts known as “H₂ spillover”. In fact, in this case platinum catalyzes the reduction of the surface support at lower temperatures, while also reducing himself (Ricote S., 2006). That’s why the extent of the surface reduction peaks of the support in the TPR profile is much smaller than the platinum attributed reduction peak.

Table 11 Hydrogen uptake experimentally measured

Catalyst	H ₂ uptake (μmol/g)
PtCeZr	752
PtCe	649
1Pt14CeAl	134

The reduction behavior of the other samples was compared to that of PtCeZr in quantitative and qualitative terms. Table 11, in which there is the hydrogen uptake experimentally measured for all catalysts, showed a marked difference between Pt14CeAl and the other two catalysts; in fact, the most reducible catalyst was PtCeZr, followed closely by PtCe, with Pt14CeAl that resulted much less reducible than the other samples. This phenomenon is of course correlated to the type of support, with alumina that is widely known as a non-reducible oxide. Moreover, the Figure 53, which shows the first reduction peak of the three samples (the peak which is surely related to the presence of platinum (Ricote S., 2006)), it can be seen that the pattern of the onset seems to follow a trend of platinum’s temperature reduction probably correlated to the uptake; the PtCeZr catalyst showed the onset at lower temperature, the PtCe catalyst was located at higher temperature but nearby the PtCeZr while at much higher temperature there is Pt14CeAl. This

behavior once again suggests the importance of the supports, where PtCeZr showed a more intimate interaction between active species and support, resulting in a better reducibility of the whole catalyst (Lin W., 2008).

In Figure 53 is shown comparison between the platinum reduction peaks of the three catalysts

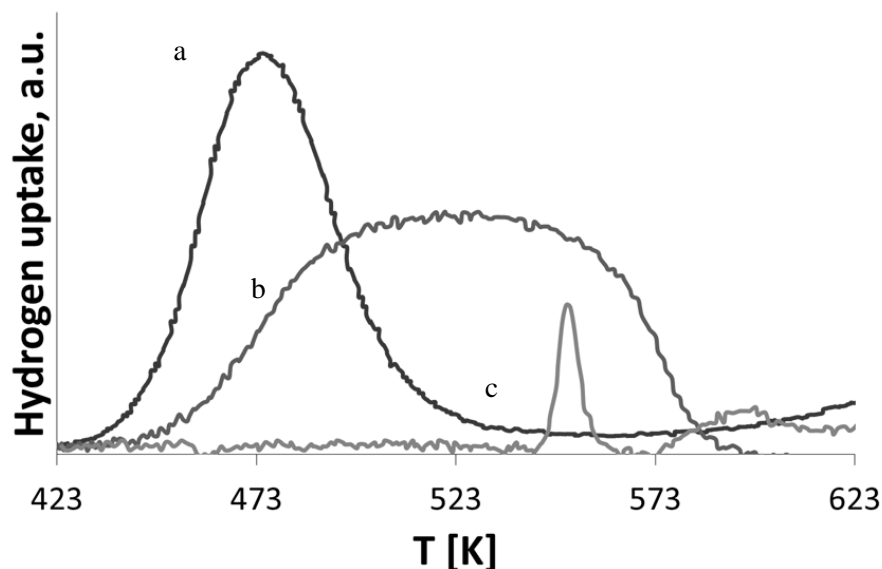


Figure 53 Comparison between the platinum reduction peak of the three catalysts (a: PtCeZr; b: PtCe; c: Pt14CeAl).

As it can be seen from the figure, the behavior of the 3 catalysts is quite different. In fact, looking at the platinum reduction peaks of all catalysts, it could be affirmed that the reduction sequence can somehow suggest the activity of the catalyst (which will be shown in the following section), both in quantitative terms (in fact, platinum ceria-zirconia is the more reducible catalyst, then platinum ceria and then platinum ceria alumina) that in terms of reduction temperature, and in this case it can also suggest somehow the threshold temperature of the catalysts.

VI.2 Initial screening: WGS activity and selectivity tests

Activity and selectivity tests were made in PROCEED lab by operating the plant described in details in (IV.4 Laboratory plant used for the activity tests). In Figure 54 WGS tests: dry molar composition at the outlet of the reactor for 1%Pt/CeO₂ catalythe results for 1%Pt/CeO₂ sample are shown. In particular, on the x-axis there is the reaction temperature, while the y-axis shows the molar percentage (on a dry basis) of the species at the outlet of the reactor.

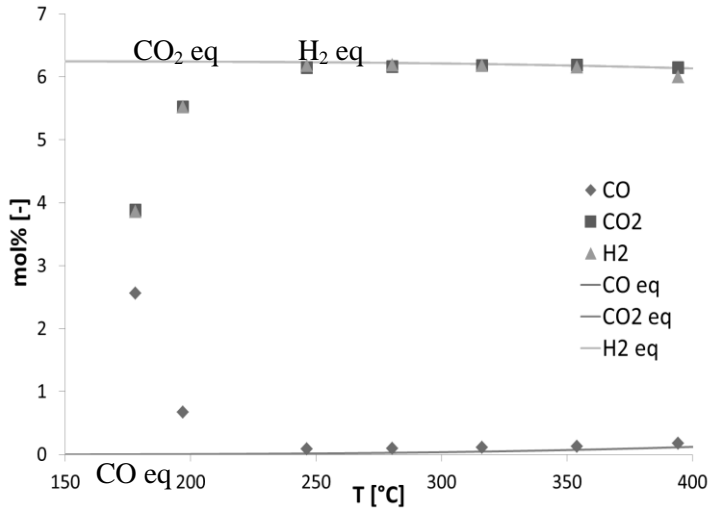


Figure 54 WGS tests: dry molar composition at the outlet of the reactor for 1%Pt/CeO₂ catalyst

First of all, it is noted that the composition profiles of the various species are quite symmetrical, so the catalyst would be very selective, because CO is always transformed in CO₂ and hydrogen: in particular, the signals seem to be in good agreement with the equilibrium composition in the range 240-390°C, while below 240°C the catalyst gradually loses its activity (at 180°C CO conversion is almost 60%).

In Figure 54 are shown the results for 1%Pt/CeO₂-ZrO₂ sample.

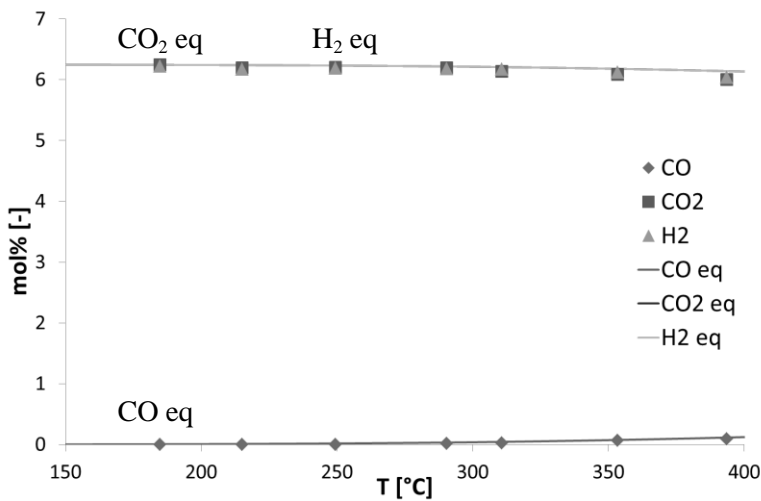


Figure 55 WGS tests: dry molar composition at the outlet of the reactor for 1%Pt/CeO₂-ZrO₂

Chapter VI

In this case, the experimental points seem to be in good agreement with the equilibrium composition in all the investigated range. Actually, at the highest temperature (390°C) it has been registered a little amount of methane (ppm), probably due to the methanation reaction (Figure 56). But overall, this catalyst seems to be much more active and selective (at the lower temperatures) than the other tested sample. In particular, it is noted that the experimental composition equals the equilibrium one even at 180°C, and this is very impressive in LT-WGS.

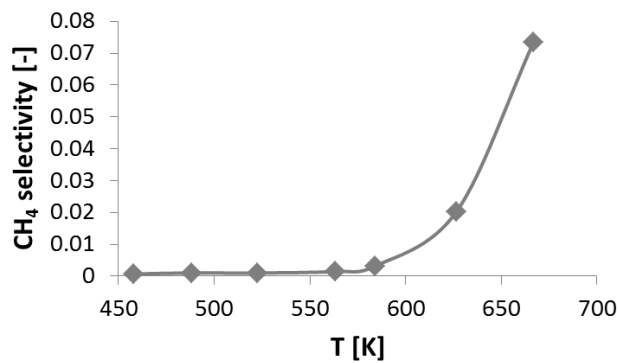


Figure 56 Composition of methane at the outlet of the reactor for 1%Pt/CeO₂-ZrO₂

In Figure 57 the results for 1%Pt/14%CeO₂/γAl₂O₃ are shown

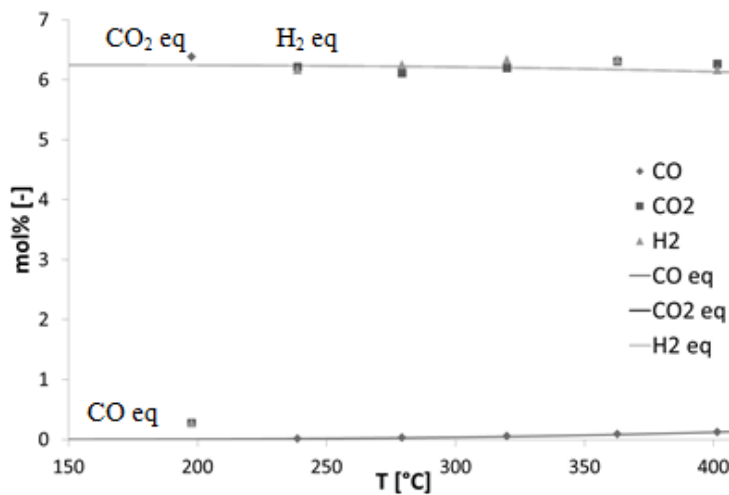


Figure 57 WGS tests: dry molar composition at the outlet of the reactor for 1%Pt/14%CeO₂/Al₂O₃ catalyst

Also in this case, the catalyst showed a very good selectivity for the WGS reaction, due to the presence of platinum interacting with ceria (Luengnaruemitchai A., 2003). In particular, it was observed an equilibrium composition in the temperature range between 240°C and 400°C, while at 200°C the CO conversion fell down.

The Figure 58 a comparison between the three investigated samples in terms of CO conversion as function of temperature are shown. The activity data at each temperature were determined after stabilization of the concentration of the species, and no deactivation was detected during the tests.

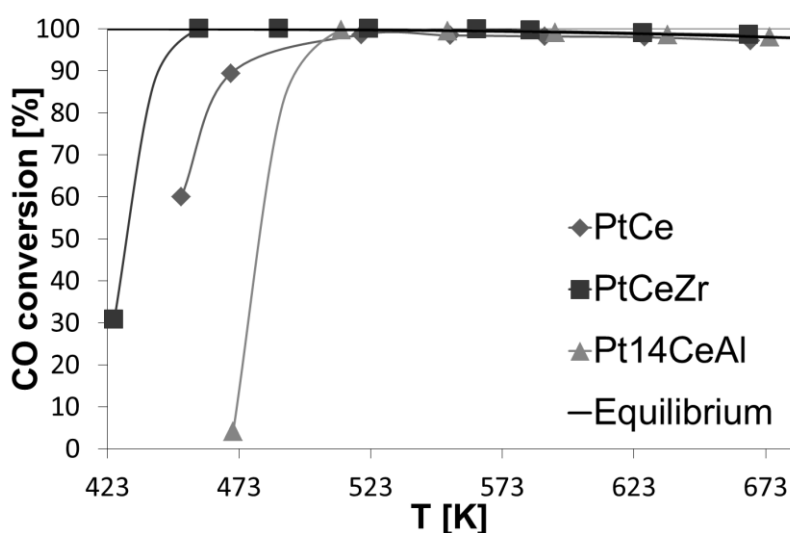


Figure 58 Comparison between the three investigated samples in terms of CO conversion as function of temperature.

All the samples showed a very good activity for the WGS, since the thermodynamic equilibrium approach was observed for temperature above 513 K. The activity of the catalysts was in the following order: PtCeZr > PtCe > Pt14CeAl. In particular, Pt14CeAl approached the equilibrium in the range 513-673 K, but at 473 K the conversion fell to 5 %. The same happened for the PtCe sample, but in this case the CO conversion at 473 K was still very high (90 %), while it decayed to 60 % at 453 K. The PtCeZr catalyst was above all the most active, reaching the equilibrium value even at 453 K, and also showing a very appreciable activity at 423 K (CO conversion was about 30 %).

During the last years the catalytic behavior of the ceria supported catalysts for the Water Gas Shift reaction has been largely studied. It has been demonstrated also the synergism between the noble metal and the oxide support, operating together into the reaction mechanism; so, it has been

Chapter VI

established that the main reason for having a high active WGS catalyst has been referred to the redox properties of the ceria support, i.e. the capability to provide oxygen atoms due to the high oxygen mobility into the bulk of the support. Therefore, it is clear that the presence of ceria is of primary importance. The approach used in this part of the thesis has been to prepare different platinum based catalysts supported on ceria, trying to modify the support composition to show the importance of the reasons discussed above. In fact, the modification of the ceria bulk by the introduction of Zr atoms brought to a lower cell parameter, as detected by XRD; this phenomenon has created a distortion in the crystal cell, and may have been the main cause of the better activity of the PtCeZr catalyst. Moreover, it is well known that ceria, when used in a WGS catalyst, undergoes the carbonation phenomenon, this limiting the catalyst overall activity. So, the presence of zirconium could have also limited this, enhancing the activity also at lower temperatures.

The PtCeZr catalyst could be really a very attractive catalyst for the one-stage WGS process, showing a 30 % CO conversion at 423 K, which is a very low temperature; moreover, it could be used also in a membrane reactor, where the operating condition of course could be favorable, leading to savings in terms of energy consumption, and where the presence of the membrane is useful to reach higher conversion by removing selectively one product from the reaction mixture.

Actually, also the Pt14CeAl could be a promising catalyst for the WGS process, taking into account the limited supply of ceria and zirconia, as rare earths, because in this catalyst there is a reduction of the ceria content of about 85 %; this, together with the low platinum loading, would provide a very active catalyst with also a competitive price. Moreover, taking into account also that the presence of Alumina could be very useful for the deposition of the active phases on the structured carrier already investigated in the previous chapters, this increases the utility that this type of catalyst might show for WGS reaction; this will be evidenced in the following chapters.

VI.3 1%Pt/CeO₂-ZrO₂: performances by increasing space velocity

(GHSV test) and preliminary stability test.

The catalyst showing the best performances in this initial screening was then tested under different flowing condition (at different GHSV), and also its stability was investigated. The tests were carried out in a stainless steel tubular reactor with annular geometry, the same reactor as described in the previous chapters for the WGS initial screening experiments. The influence of contact time on CO conversion was studied by varying the gas hourly space velocity from 6,000 h⁻¹ up to 51,000 h⁻¹. The reactants mixture

consisted of 8 % CO, 30 % H²O and N² balance and the temperature was set up to 498 K.

Finally, a stability test was made up at a temperature of 473 K on a reactants mixture containing 8 % CO, 30 % H²O and N² balance, with a GHSV = 15,000 h⁻¹.

As already mentioned above, in the conditions investigated PtCeZr resulted, among the others, the best catalyst in terms of activity and selectivity: on this formulation, the effect of GHSV on catalytic performances was investigated (Figure 59).

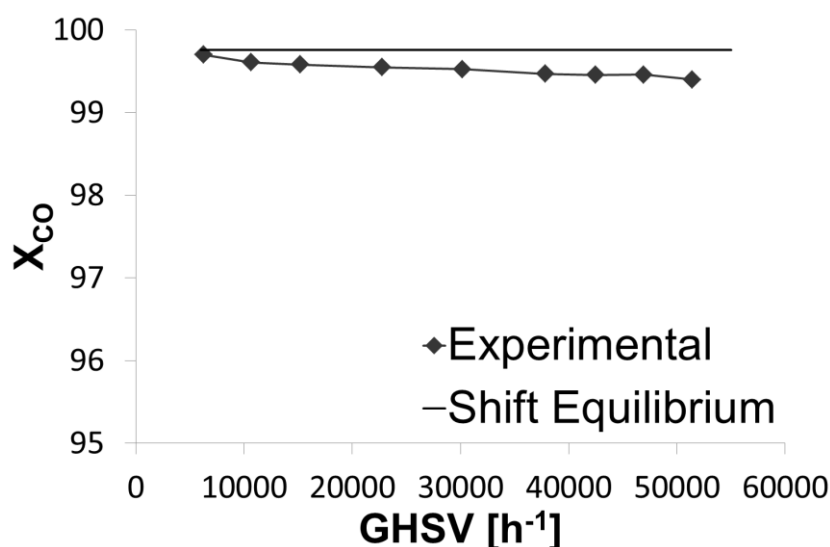


Figure 59 Effect of space velocity on PtCeZr catalyst

It is worth to underline that the operating conditions chosen for this kind of test were very stressful. In fact, for this type of experiment we decided to work with a very low temperature, the CO concentration was higher than that used for the activity test, and the steam to carbon ratio was even lower, and we operated up to a space velocity of about 10 times greater than the industrial one.

As reported, this catalyst showed an excellent activity, also at high space velocity, both in terms of conversion that selectivity. A slight reduction in catalytic activity did not affect the very good performance of the proposed formulation.

Stability test results are summarized in Figure 60.

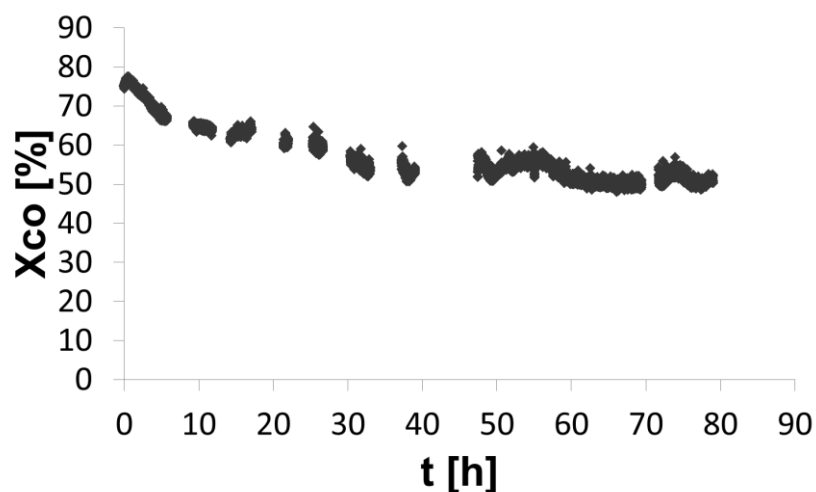


Figure 60 Stability test on PtCeZr (80 hours)

It is observed that, under the selected operative conditions, typically very stressful for the WGS catalyst, the CO conversion started from a value of about 80%, in the first 40 hours decayed to a value of about 50%, then it remained almost constant. All of this behavior suggests a negative exponential law, coming to a plateau value. Regarding the reasons for the partial deactivation followed by stabilization, it can be assumed that probably sintering phenomena may occur (Azzam K.G., 2008). Moreover, the stabilization of the conversion suggests that the initial deactivation is not a dramatic phenomenon (also it's to be remembered that the operating conditions chosen for the stability test were very stressful for the catalyst).

Chapter VII. Deposition of the active phases on the structured carrier, characterization and tests on the structured catalysts

The structured catalysts are usually prepared by deposition of a catalytic formulation on the structured carrier, sometimes modified by the deposition of a washcoat formulation. Washcoat materials are selected to form a rough, irregular surface, which greatly increases the surface area compared to the smooth surface of the bare structured carrier. Coating the structured directly with precious metals would yield a catalyst that would react poorly, so it would take very large catalyst elements to reach high levels of control efficiency. Washcoating the structured increases the available surface area dramatically, which in turn maximizes the catalytically active surface available to react.

The use of a washcoat allows to increase the specific surface area of the carrier significantly (González Carlos A., 2007) so, the chemical and physical affinity of the washcoat compounds with the structured support material is very crucial. In this chapter the choice of the Washcoat formulation will be discussed, for the deposition of the catalytic phases on the Aluminum open cells foam chosen from the heat transfer study already discussed in Chapter V. Moreover, the structured catalysts have been characterized with different techniques, and tested for the WGS reaction, also in nearly adiabatic conditions, to exploit the high thermal properties of these new catalysts with respect to a packed bed.

VII.1 Preparation of the Washcoat

Although foams have a lot of pores, they still show a low specific surface area, also because the external surface of the pores (which are macropores) isn't rough enough. So, they need a washcoat to increase their surface area.

Chapter VII

The active species of the washcoat was the ceria-zirconia solid solution, as it showed the best catalytic performances in the activity and selectivity test made on the catalysts in powder. Actually, there was a totally different situation in the choice of the precursor of the platinum for the impregnation of the washcoated foam.

The first tests were made by using as precursor salt the platinum chloride, by Sigma Aldrich. But, after few minutes the solution became black, as it can be seen in Figure 61.



Figure 61 Experimental result obtaining using platinum chloride as precursor

A very “nice” phenomenon happened to the foam too (Figure 62).

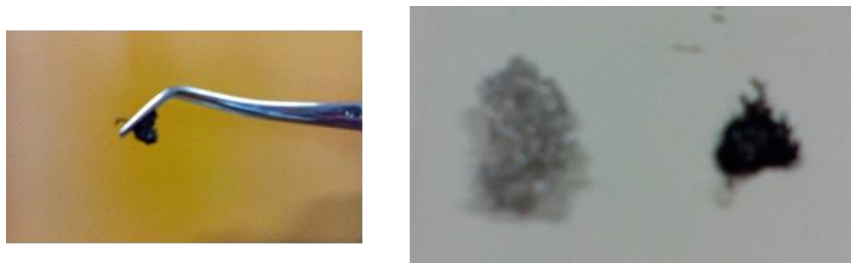


Figure 62 Aluminum foam after dipping in platinum chloride solution

This is of course a problem of corrosion. In fact, the chloride is a problem during the aqueous impregnation of aluminum for the onset of the corrosion reaction. This redox reaction is catalyzed by the presence of Cl^- ions which, migrating through the oxygen vacancies in the oxide film that covers the aluminum, "dissolves the aluminum" in water making corrosion possible. Among the anions that accelerate this reaction there is not nitrate. It was made a comparison, by impregnating a portion of aluminum foam in a solution of platinum chloride on one side and amino platinum nitrate on the other side; in the chloride solution was forming in a short time a thin black precipitate, evidence of the redox reaction; in the nitrate solution this does

not occur within 30 minutes (Figure 63), and it was also verified that during the drying in the oven does not have any evidence of redox reaction.

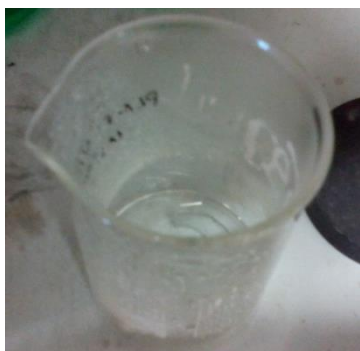


Figure 63 Experimental result obtaining using amino platinum nitrate as precursor

VII.1.1 Formulation of the Washcoat

The washcoat was prepared by dispersing the support in powder form CeO_2ZrO_2 in a weakly acidic solution of pseudoboehmite and methylcellulose (pH = 4). The ratio of the mixed oxide cerium / zirconium and pseudoboehmite is 8/1 by weight. The washcoat had a concentration of 20% by weight of solids. The amount of pseudoboehmite proved adequate to ensure good adhesion of the washcoat to the structured substrate of aluminum as well as evident in the characterization of the washcoated aluminum foam, that will be shown in the next sections.

The washcoating was made according to the following points (Figure 64):

1. Foam cut: the open cells Aluminum foam was cut and modeled to obtain a cylindrical form.
2. The washcoat was prepared according to what explained in details in the previous section.
3. The real washcoating procedure was applied according to the dip-coating method (see next figure); a specimen of aluminum foam weight was impregnated by immersing it in the washcoat and ensuring a contact of 30 minutes.
4. After the immersion, the excess of washcoat was removed by air flow, the resulting sample was dried in an oven at 120 ° C for 2 hours and then calcined at 600 ° C for 3 hours.

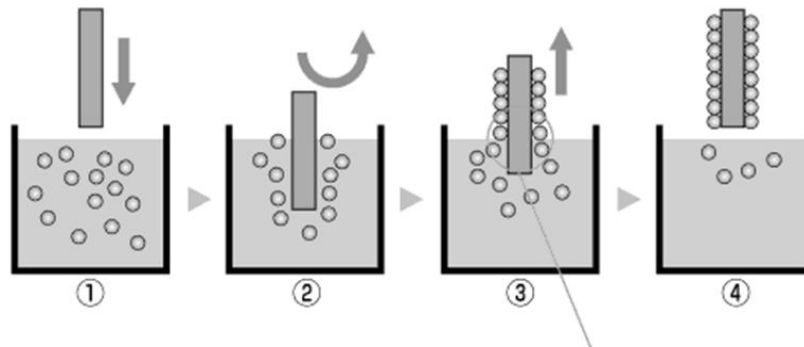


Figure 64 Dip-coating procedure

It was noted that after four successive impregnations the weight of the foam with washcoat is approximately doubled compared to the initial weight, and at the same time you do not notice any clogging of the free spaces of the foam.

VII.1.2 Characterization of the Ce-Zr washcoat

To test the bond strength between the washcoat and the foam the stability tests in petroleum ether were carried out at 25 ° C, with an ultrasonic bath set at 60% power, with 6 cycles of 5 minutes; it was recorded a loss of less than 10% in the first three cycles (15 min) and substantial stability in the following three cycles (Figure 65).

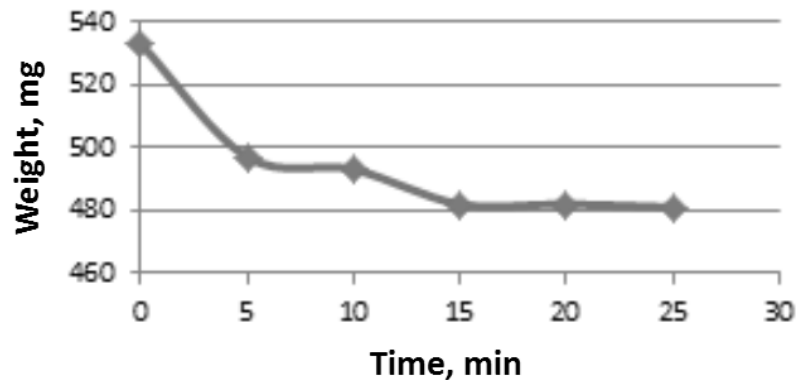


Figure 65 Mechanical stability of Ce-Zr washcoat on aluminum foam

Also the specific surface area was evaluated according to the B.E.T. method. In the Table 12 the main data are shown.

What immediately stands out in the eyes is that the washcoat increased significantly the specific surface area of the aluminium open cells foam, from 1 to 36 m²/g.

Table 12 BET characterization

Sample	BET surface (m ² /g)
CeO ₂ -ZrO ₂ powder	64,5
Aluminium Foam	1,5
Washcoat powder	76,9
Pt/Washcoat powder	75,7
Pt/Wcoat/AlFoam	36,4

Other considerations that can be made are that the alumina presence in the washcoat formulation (the precursor is pseudoboehmite) slightly increased the specific surface area of the ceria-zirconia washcoat; moreover, the adding of platinum on the washcoat was also made, this didn't caused a substantial decrease of the specific surface area.

VII.2 WGS test on the Ce-Zr washcoat in powder form, catalyzed with platinum

In order to test the performances of this new formulation, the washcoat obtained by the ceria-zirconia solid solution with alumina was dried and calcined at 450°C for 3 hours. The resulting powder was then impregnated in a solution of tetramineplatinum nitrate (by Sigma Aldrich), then dried at 120°C and calcined at 450°C for 3 hours.

The system used for this activity and selectivity test was constituted by a stainless steel tubular reactor (internal diameter equal to 22 mm) inserted in an oven with three thermal control zones. The tests were performed at atmospheric pressure, in a temperature range between 200°C and 400°C. The reactive mixture was composed by 8 vol% of CO, 30 vol% of H₂O and N₂ balance. The Weight Hourly Space Velocity (WHSV) was set to 1.2 h⁻¹, with respect to the CO mass flow rate. Water was vaporized before entering the reactor and previously mixed with the gas phase. The catalyst sample in powder form was crushed and sieved in order to have a particles dimension between 180 and 355 μm. The products mixture generated by the reaction was continuously analyzed by two different devices: the infrared detector "ABB Uras 14" for CO, CO₂ and CH₄, and the thermal conductivity detector "ABB Caldos 17" for H₂.

The results of the activity and selectivity tests are shown in Figure 66, which reports the CO conversion as function of reactor temperature. The experimental data were compared with those predicted by the thermodynamic equilibrium.

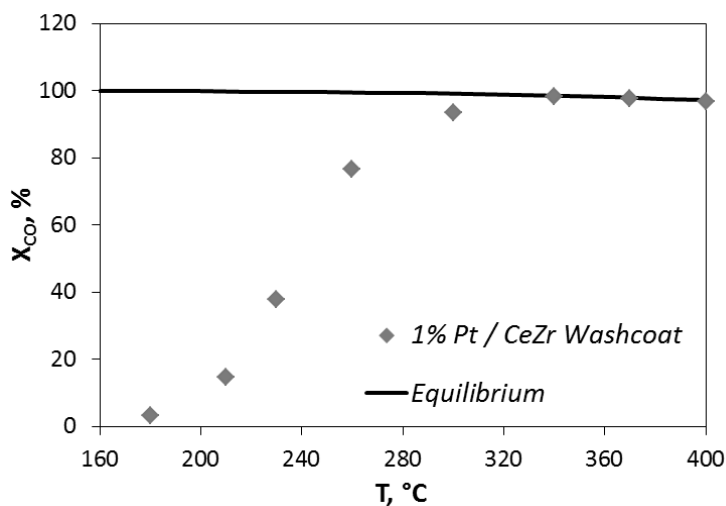


Figure 66 Activity and selectivity tests of 1%Pt/CeZr as function of reactor temperature

This catalyst showed equilibrium conversion in the temperature range between 320°C and 400°C. Below 300°C the catalyst was much less active (at 240°C the CO conversion was in the order of 40 %).

The performances shown by this tested formulation were totally different if compared with those of the 1%Pt/CeO₂-ZrO₂ catalyst tested in Section VI.2. In fact, it has to be considered that the chemical formulation sensibly changed, due to the presence of alumina in the washcoat composition. Alumina is essential in the formulation of the washcoat, but its presence could have determined the poor efficiency of this new formulation.

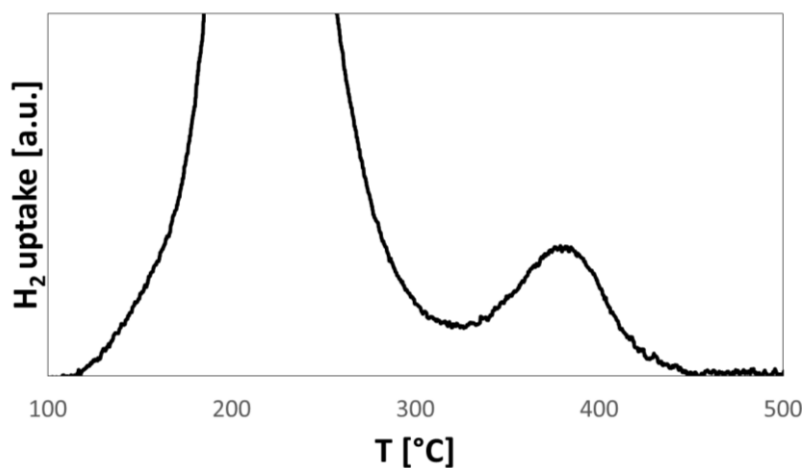


Figure 67 TPR profile of 1%Pt/CeO₂-ZrO₂ washcoat

In order to better understand the reasons for this behavior, a Temperature Programmed Reduction (TPR) was performed on the 1%Pt/CeZr Washcoat sample. The catalyst was reduced using a stream of 5% by volume of H₂ in N₂ with a GHSV of 15000 h⁻¹. The set temperature program included a step of heating by T_{amb} up to 500°C, with a speed of 10°C/min, and a step isotherm at 500°C for 1 h. The result is reported in Figure 67.

In the figure above, apart from the reduction peak characteristic of PtO_x reduction, set at 220°C, another peak, centered at 385°C, was ascribed at the reduction of platinum aluminate species (Dimas Rivera G.L., 2014). This results revealed that there was a strong interaction between platinum and alumina; taking this into account, it is well known that such interactions tends to deactivate a Water Gas Shift catalyst based on noble metals supported on irreducible oxides, by increasing the threshold temperature (Panagiotopoulou P., 2006).

So, the aim was to prepare a new chemical formulation, in order to avoid, or at least reduce, the interaction between platinum and alumina. It was decided to follow the same concept already used in Section IV.1, when preparing the 1%Pt/CeO₂/Al₂O₃. The aim was to cover the surface of alumina by using a certain amount of ceria to obtain at least a monolayer. The details of this new preparation will be discussed in the following paragraphs.

VII.3 Formulation, characterization and testing of the new

Alumina covered ceria washcoat

The new washcoat slurry was prepared by suspending, under mechanical stirring, 15,4 wt% of γ -alumina, previously powdered to obtain a set of particle less than 10 μm , in a colloidal solution of 4,6 wt% of pseudoboehmite and 1wt% of metilcellulose at pH=4. (Boukha Z., 2014). The washcoat mixture has been finally vigorously stirred for about 24 hours, to guarantee the perfect suspension of the solids content. The washcoat was then dried at 120°C for 2 h and calcined at 450°C for 3 h. The resulting powder was then impregnated in a solution of cerium nitrate (by Sigma Aldrich), to reach a loading of 20wt% of ceria on alumina; then, the sample was dried at 120°C and calcined at 450°C for 3 hours. After that, another impregnation step was performed, in a solution of tetramineplatinum nitrate (by Sigma Aldrich), to reach 1wt% of loading, then the sample as dried at 120°C for 2 h and calcined at 450°C for 3 h.

The catalyst sample was put into the reaction system and tested in the same conditions as Section VII.2. The results are reported below (Figure 68), in terms of CO conversion as function of temperature, and they were compared with those of the PtCeZr Washcoat sample.

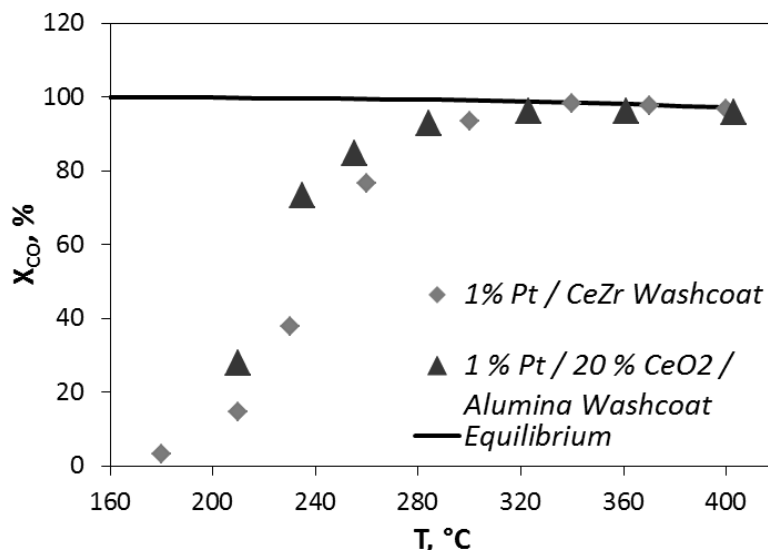


Figure 68 Comparison of activity and selectivity tests of 1%Pt/CeZr washcoat and 1%Pt/20%CeO₂ Alumina washcoat as function of reactor temperature

The new proposed formulation showed better activity, especially at low temperatures. In particular, at 240°C the new catalyst showed a CO conversion of 73%, while the PtCeZr Washcoat catalyst stood at 39%. So, it was decided to prepare a structured foam catalyst with this new chemical formulation.

VII.4 Preparation of the structured catalyst

Therefore, the Aluminum foam was loaded with an alumina-based washcoat, prepared as explained in the previous paragraphs, while, for what regards the catalytic formulation, a platinum/ceria based catalyst was chosen as the best compromise, from an economical point of view, between costs of materials and hydrogen productivity. In fact, platinum based catalysts allows to have high CO conversion and hydrogen yield even with very low metal loading (Jacobs G., 2005b); on the other hand, the use of alumina reduces the amount of ceria which is needed for supporting the active species. In this way, the catalyst materials supply becomes cheaper.

The structured catalysts were prepared in two subsequent steps, the first involves a dip-coating procedure, the second an impregnation of the active phase. A cylindrical monolithic Aluminum foam (purchased by ERG Materials and Aerospace, 40 pores per inch, relative density: 6-8%, diameter: 16 mm, length: 88 mm), previously treated in a HCl 0,1N solution for 20 minutes and then calcined at 500°C for 3 hours, was immersed into a

beaker containing the washcoat suspension for about 20 minutes, followed by air blowing, in order to remove the excess of washcoat; then the sample was dried in an oven set to 120°C for 2 hours. This procedure was repeated further until the weight of the washcoat reached the desired value (a loading of about 40wt% with respect to the total weight of the washcoated foam), and the resulting carrier was calcined in muffle at 450°C for 3 hours. The mechanical stability of the washcoat was then tested with the ultrasonic treatment (see Section VII.5.1).

The catalytic phases, Platinum/Ceria, were then added by the wet impregnation method. Firstly, the washcoated carrier was dipped at room temperature in an aqueous solution of $\text{Ce}(\text{NO}_3)_3 \cdot 6\text{H}_2\text{O}$ (purchased by Sigma Aldrich, 99.99% trace metals basis) for about 20 minutes, followed by drying at 120°C for 2 hours and calcination at 450°C for 3 hours. This procedure was repeated until the Ceria loading reached a value of about 20wt% with respect to the washcoat solely. The concentration of the cerium nitrate aqueous solution was chosen in order to have two impregnation steps before reaching the 20wt% loading.

Finally, the sample was impregnated into a $\text{Pt}(\text{NH}_3)_4(\text{NO}_3)_2$ aqueous solution (purchased by STREM Chemicals, 99%) for 15 minutes, followed by drying at 120°C for 2 hours and calcination at 450°C for 3 hours. The total amount of loaded platinum, 1wt% with respect to washcoat and Ceria together, was reached in one impregnation step. The final structured foam catalyst so obtained was: 1%Pt/20%CeO₂/γ-Al₂O₃.

In addition, as reference, a catalyst in powder form with the same formulation was prepared by wet impregnation of γ-Al₂O₃, obtained by drying and calcining an amount of the washcoat previously prepared, in a solution of cerium (III) nitrate hexahydrate, followed by impregnation in a solution of tetraamineplatinum (II) nitrate; both these two impregnation steps were followed by drying at 120°C for 2 hours and calcination at 450°C for 3 hours.

VII.5 Samples characterization

The catalysts were characterized by several techniques. The γ-alumina particles size dimension was checked by optical microscope analysis: a sample of about 20 mg was dispersed in 20 ml of ethylene glycol, the mixture was sonicated for about 5 minutes and then it has been analyzed by means of optical microscopy.

The mechanical stability of the washcoat deposited on the foam was evaluated by means of an ultrasonic adhesion tests performed by dipping the sample in petroleum ether and applying the ultrasounds for cycles of 5 minutes each. Specific surface area (BET) was evaluated by dynamic N₂ adsorption measurement at -196°C, performed by a Costech Sorptometer 1040 on samples pretreated at 150°C for 30 min in He flow. The effective

metal loading of the catalysts was determined through the Energy Dispersive X-ray fluorescence (EDXRF) spectroscopy (Thermo-Scientific Quant'X).

Wide-angle X-ray diffraction (WAXD) patterns with nickel filtered Cu-K α radiation were obtained with an automatic Bruker D8 Advance diffractometer, in reflection. Laser Raman spectra were obtained at room temperature with a Dispersive MicroRaman (Invia, Renishaw), equipped with 514 nm diode-laser, in the range 200-2000 cm⁻¹ Raman shift. Scanning electron microscopy (SEM) (Assing,mod. LEO 420) was used to characterize the morphology of the samples at an accelerating voltage of 20 kV. The latter was also coupled with an EDX, in order to study the deposition of the chemical species on the structured carrier.

VII.5.1 Investigation on the washcoat deposition

The washcoat particles dimensions were investigated by optical microscopy. It is, indeed, very important to have very small particles suspended in a washcoat slurry (Cristiani C., 2007). In Figure 69 it has been reported an image of the washcoat particles suspended in ethylene glycol. In particular, it was possible to observe different zones of about 300x300 μm . Definitely, in all the investigated zones, it has been found that particles dimension was never above 10 μm .

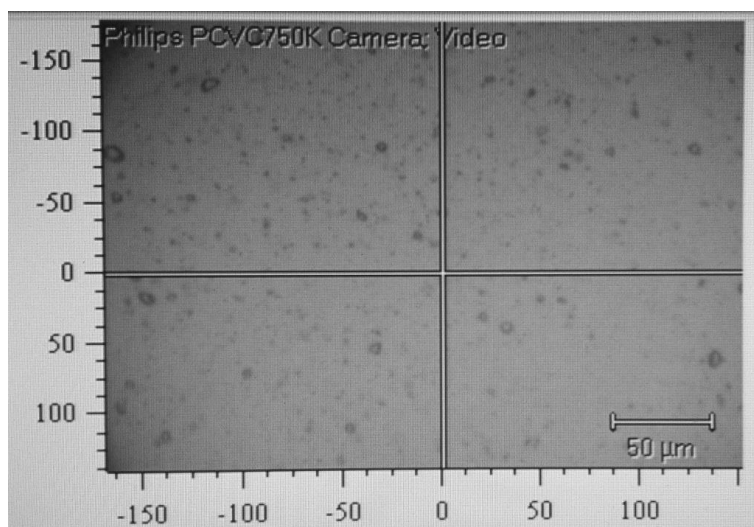


Figure 69 Imaging from optical microscopy of the alumina washcoat

The washcoat weight loss after sonication of the sample is shown in Figure 70. After an initial loss during the first 15 minutes, the weight of the sample did not change anymore. Moreover, the overall weight loss, with respect to the washcoat weight, was in the order of 2%, which is an evidence of a very good mechanical stability and reveals the very strong adhesion of

the alumina washcoat over the foam surface, comparing it to other similar formulations reported in the literature (González-Velasco J. R., 2003). In order to estimate the washcoat layer on the aluminum foam, it was applied the simplified method used by (Montebelli A., 2014), which provides for the estimation of the washcoat layer based on the knowledge of the washcoat density and the foam strut mean diameter. The washcoat density was calculated by pycnometer, while the strut diameter was estimated by processing the aluminum foam SEM image. Taking into account all this information, the estimated washcoat layer on the aluminum foam was in the order of 50 μm .

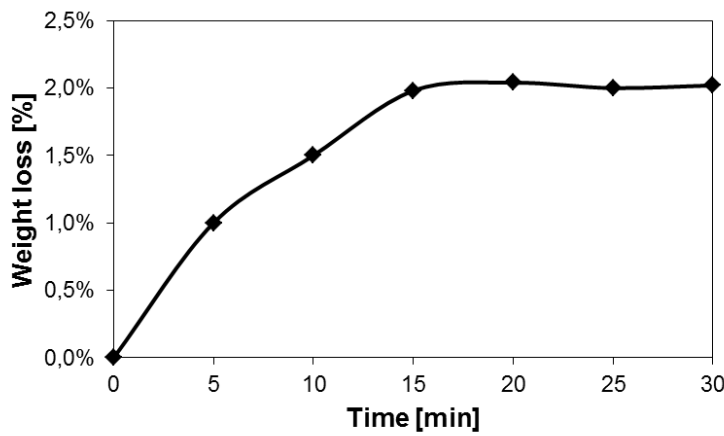


Figure 70 Washcoat weight loss after ultrasonic treatment: behavior during time

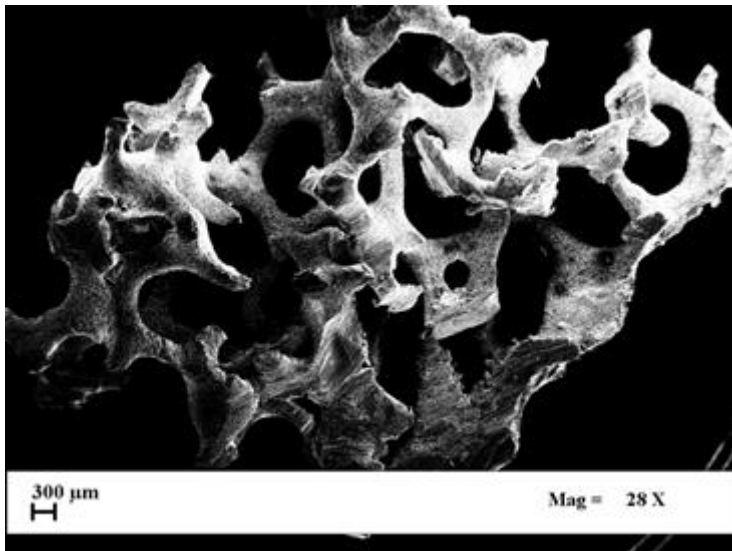


Figure 71 SEM of the structured washcoated sample. Magnitude: 28X

Chapter VII

The Scanning Electron Microscopy was also used to verify the homogeneous deposition of the washcoat on the structured carrier, which can be seen in Figure 71 that shows the SEM image of the washcoated sample.

A good and homogeneous deposition of a washcoat on a structured carrier is always something difficult to obtain (Cristiani C., 2009b). Besides, it is also crucial to verify the deposition of the active species. The EDX of the catalyzed structured sample (Figure 72) shows the mapping of Aluminum, Cerium and Platinum on a little portion of the sample. Here, in a qualitative way, it is possible to claim that ceria is well deposited, in a way such to cover Alumina, and moreover it seems also well dispersed. Furthermore, Platinum seems to be in turn well dispersed on the surface of ceria. Although this characterization doesn't give real and precise information about the dispersion of the active species, it is a good way to verify that there has been a good and homogeneous deposition.

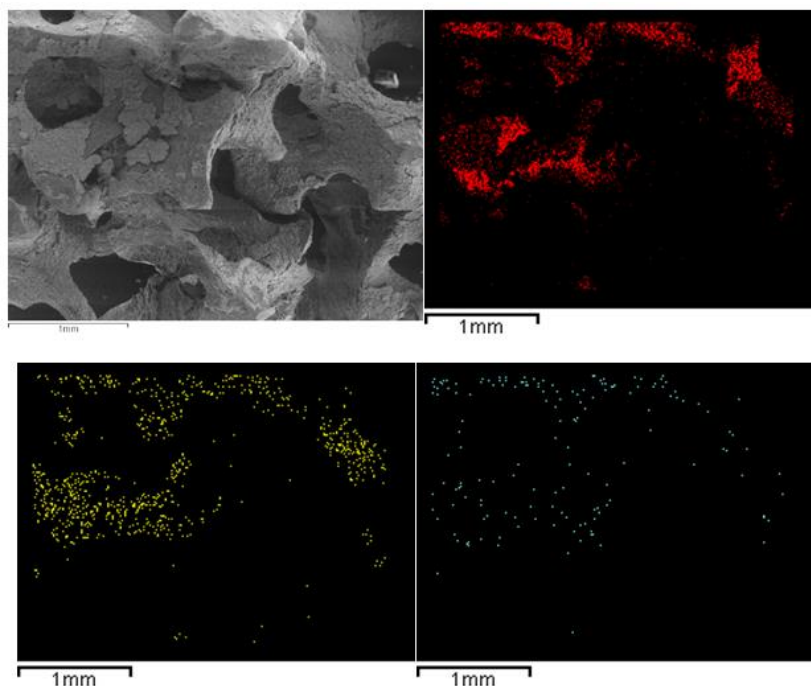


Figure 72 SEM/EDX of the structured catalyst. In red, the mapping of the Alumina washcoat, in yellow the Ceria support and in light blue the Platinum

VII.5.2 Characterization of the catalysts

From now on, it will be referred to “W.” for the washcoated samples, “W.Ce” for the 20%CeO₂/γ-Al₂O₃ samples and “W.Ce/Pt” for

1%Pt/20%CeO₂/γ-Al₂O₃ samples; letters in parentheses are “p” for powder samples and “s” for structured ones.

Table 13 reports the nominal loadings and the specific surface areas of the samples. In the powder catalyst, the instrument has detected a platinum loading a bit lower than expected (about 0.8wt%), while ceria loading is actually a bit higher (about 20.7wt%). Actually, for what regards the structured catalyst, the platinum loading is very close to the expected value (0.9wt%), while ceria is about 22wt%. The measured values of the specific surface area of the samples, obtained by means of the BET method, reveal that the deposition of the washcoat on the foam surface allows to increase the BET surface area of about two orders of magnitude. Actually, this data confirm what it has been expected. Indeed, by considering that the loaded quantity of washcoat and active species is about 40wt%, the measured BET surface area seems to be a weighted average between the foam and the total amount of the loaded species.

Table 13 Nominal loadings and the specific surface areas of the samples

Sample	Nominal weight % (from XRF)			Typology	B.E.T. [m ² g ⁻¹]
	Al ₂ O ₃	CeO ₂	Pt		
Aluminum foam, 40 PPI	0.0	0.0	0.0	Structured	n.a. (~0)
W.(s)	100.0	0.0	0.0	Structured	63.8
W.Ce(s)	79.1	20.9	0.0	Structured	55.3
W.Ce/Pt(s)	78.5	20.7	0.8	Structured	54.5
W.(p)	100.0	0.0	0.0	Powder	156.5
W.Ce(p)	77.7	22.3	0.0	Powder	138.4
W.Ce/Pt(p)	77.0	22.1	0.9	Powder	132.1

The XRD patterns of the powder samples is reported in Figure 73. Pseudoboehmite and γ-Alumina patterns have been reported as reference. In all the prepared samples the diffraction lines corresponding to cubic ceria fluorite type structure (JCPDS# 00-004-0593) and to γ-Alumina phase (JCPDS# 00-048-0367) have been detected. No signals about platinum were observed; the reasons for this fact could be the too low loading of noble metal, or eventually its high dispersion. More in particular, the analysis of the spectra of the washcoat sample and its precursors revealed that γ-Alumina phase corresponds to the totality of the washcoat composition. This result is due to the fact that when pseudoboehmite is calcined at 450°C, its structural configuration changes as to form the γ-Alumina phase. The difference between the calcined pseudoboehmite spectra and γ-Alumina spectra is that the first one showed a bit less defined peaks, probably due to a more evident amorphous behavior.

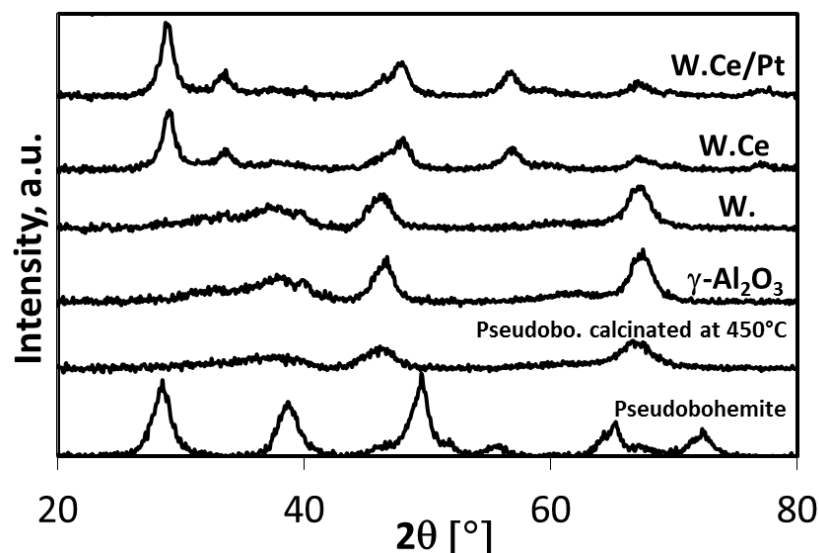


Figure 73 XRD pattern of the powder samples, obtained by the washcoat precursors (pseudoboehemite and γ -Alumina), followed by the washcoat, ceria/washcoat and 1% Pt/ceria/washcoat (fresh and exhausted) catalysts

The mean crystallites size of the calcined samples has been calculated by the Scherrer equation ($k = 0.9$), as reported in Table 14.

Table 14 Crystallites size from Scherrer equation

Sample	Crystallites size (from XRD) [nm]			
	Pseudoboehemite	γ -Al ₂ O ₃	CeO ₂	Pt
Pseudoboehemite	3			
γ -Al ₂ O ₃		5		
W.(p)		5		
W.Ce(p)		6	7	
W.Ce/Pt(p)		6	7	n.d.

It was possible to calculate the mean crystallites size of γ -Alumina and ceria, together with pseudoboehemite as reference. In all cases, the calculated size was in the order of few nanometers; in particular, the pseudoboehemite sample showed the smallest dimension, 3 nm, while the γ -Alumina showed a mean dimension of 5 nm, the same as the washcoat sample, which is all composed by γ -Alumina. The deposition of ceria on γ -Alumina caused a little increase in mean crystallites size of γ -Alumina (6 nm), but in general it can be assumed that ceria addition did not cause a drastic increase. Ceria crystallites were in the order of 7 nm, and platinum addition did not cause changes in dimensions both for γ -Alumina and for ceria. These results

indicate a good dispersion of active species, and could also confirm what has been observed from EDX analysis..

Complementary structural information is obtained by Raman spectroscopy technique. In Figure 74 the Raman spectra of 20%CeO₂/γ-Al₂O₃ and 1%Pt/20%CeO₂/γ-Al₂O₃ structured samples is shown.

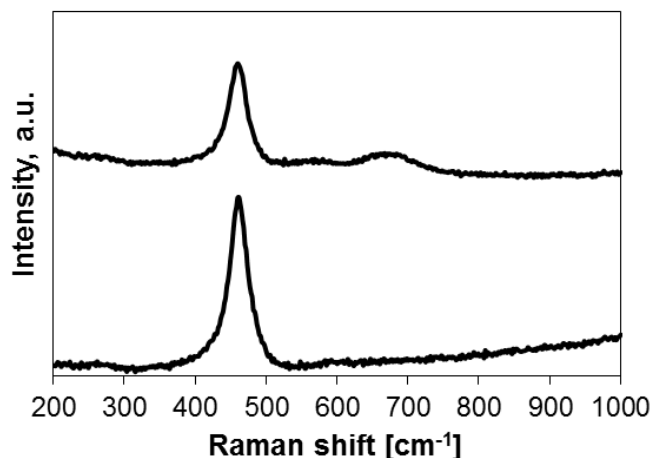


Figure 74 Raman shift of the 20%CeO₂/Al₂O₃ and 1%Pt/20%CeO₂/Al₂O₃ samples

In both samples a band centered at 460 cm⁻¹ appeared. This band was ascribed to the F_{2g} Raman mode of ceria fluorite cell, corresponding to oxygen symmetric breathing vibration around Ce⁴⁺ (Reina T. R., 2012). Looking at the platinum containing sample, a broader band centered at 675 cm⁻¹ appeared. This band can be due to two possible phenomena. According to Murrell et al. (Murrell L.L., 1993), Pt form a surface phase with metal oxide structure which interacts strongly with the surface of bulk CeO₂. Differently, (Brogan M. S., 1994) stated that the band at 675 cm⁻¹ is due to a surface distortion of ceria structure, actually due to the strong bond formed with platinum. Moreover, there was no shift of the ceria peak at 460 cm⁻¹; so, it can be stated that platinum addition did not cause a substantial distortion of ceria structure.

VII.6 Water Gas Shift activity tests: comparison between powder and structured catalyst

In order to compare the catalytic activity of the different prepared formulations, the catalysts performances for the WGS were tested in a stainless steel tubular reactor (internal diameter equal to 22 mm). The tests were performed at atmospheric pressure, in a temperature range between

200°C and 400°C. The reactive mixture was composed by 8 vol% of CO, 30 vol% of H₂O and N₂ balance. The 1%Pt/CeO₂/γ-Al₂O₃ foam catalyst was surrounded by a thermo-expanding pad and then inserted into the reactor, in order to avoid gaseous reactants mixture by-pass. The Weight Hourly Space Velocity (WHSV) was set to 1.2 h⁻¹, with respect to the CO mass flow rate. Water was vaporized before entering the reactor and previously mixed with the gas phase. For what regards the catalyst sample in powder form, it was crushed and sieved in order to have a particles dimension between 180 and 355 μm, then mixed with quartz (500-700 μm) in a proper amount in order to achieve the same bed volume as the foam catalyst. Moreover, it was also surrounded by a thermo-expanding pad, as done for the structured sample. The products mixture generated by the reaction was continuously analyzed by two different devices: the infrared detector “ABB Uras 14” for CO, CO₂ and CH₄, and the thermal conductivity detector “ABB Caldos 17” for H₂.

Figure 75 shows the activity results of the structured catalyst, in terms of species molar fractions measured on a dry base, at the reactor outlet as function of temperature.

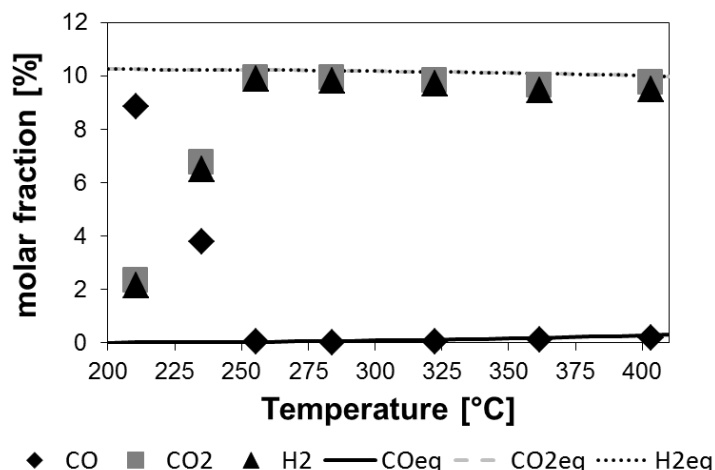


Figure 75 WGS activity of the structured catalyst (aluminum foam: 40 PPI, rel. dens.: 6-8%). Temperature dependence of molar fraction of the components (based on a dry mixture). CO inlet molar concentration: 8 %; H₂O/CO ratio: 3.75; N₂ balance; WHSV = 1.2 h⁻¹

The experimental data were compared with the equilibrium line, for a mixture of 8 % CO, 30 % H₂O and N₂ balance. The catalyst showed optimal performances in the range 250°C-400°C, in which the experimental data approximately followed the WGS equilibrium value. In particular, following the trend of CO₂ and H₂ concentrations, there is a slight difference in the measured values, with the H₂ that lies just below the carbon dioxide values. This behavior may be explained considering that the system investigated is

the result of two different reactions: the first one is the WGS reaction and the second one is the methanation reaction. In the range of temperature between 200°C and 300°C, the methanation reaction contribution is very low, and the hydrogen concentration value is very close to the carbon dioxide value. By increasing the temperature, above 300°C, the methanation reaction contribution is higher, because the difference between hydrogen and carbon dioxide signals increased. Actually, the methanation reaction, even at high temperatures (above 300°C) didn't give a significant contribution (in the order of 100 ppm) to the products mixture composition. So, it can be stated with fair approximation that this catalytic formulation has a good selectivity towards the water gas shift reaction, both at the low and the high temperatures, as well as a very good activity. The activity of W.Ce/Pt(s) catalyst reflected the data of a supported ceria/alumina platinum catalyst in powder form already tested in WGS reaction in the previous chapters. In order to appreciate the efficiency of the catalytic species deposition on the structured foam, a comparison between the W.Ce/Pt(s) and the W.Ce/Pt(p) was done. Figure 76 shows the steady state CO conversion as function of temperature both for W.Ce/Pt(s) and the W.Ce/Pt(p).

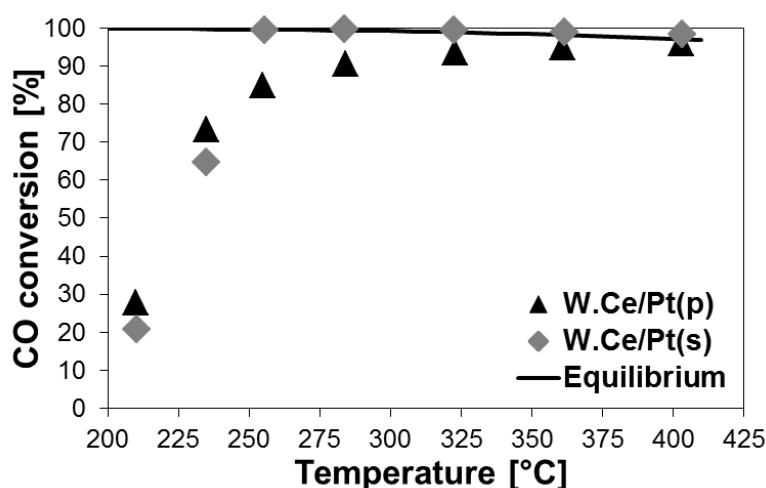


Figure 76 Influence of the Aluminum foam (40 PPI, rel. dens.: 6-8%) on the CO conversion. CO inlet molar concentration: 8 %; H₂O/CO ratio: 3.75; N₂ balance; WHSV = 1.2 h⁻¹

Indeed, the test of the catalytic activity data of the catalyst in powder form and the structured one are very similar. This result confirmed that the deposition of the catalytic formulation on the structured carrier did not cause any appreciable decrease in the performances of the final system. Moreover, it has been observed that the W.Ce/Pt(s), at the higher temperatures, seemed to be more active than the W.Ce/Pt(p). This phenomenon may be explained by considering the high thermal properties of the foam carrier, as evidenced

in Chapter V. In fact, the high thermal conductivity of the foam can play a crucial role in increasing the carbon monoxide conversion at the reactor outlet; the high conduction that is exploited in the catalytic structure ensures that the heat generated locally by the reaction can be partially removed and dispersed through the entire structured bed, while in a conventional powder or pellets catalyst it cannot be removed so easily. In fact, by considering that the reaction takes place on the surface of the catalyst, and, as well known, the WGS process is an exothermic reaction, the temperature of the catalyst increases, limiting the equilibrium conversion theoretically achievable. So, when the catalyst is in powder form, the heat of reaction cannot be removed because of the low conductivity, while when the catalyst is dispersed on the Aluminum foam, this limitation can be overcome; in particular, by considering that the thermal conductivity of the Aluminum structure increases of one order of magnitude between 200°C and 400°C, this phenomenon can be more incisive. This is reflected on the reachable equilibrium conversion of the WGS, causing a lower product temperature in the case of the W.Ce/Pt(s). Further details on the effect of the high thermal properties of the foam catalyst will be explained in the following part of this Chapter.

VII.7 Stability of the structured foam catalyst

The behavior under time on stream of the W.Ce/Pt(s) has been investigated, in order to study the catalyst deactivation.

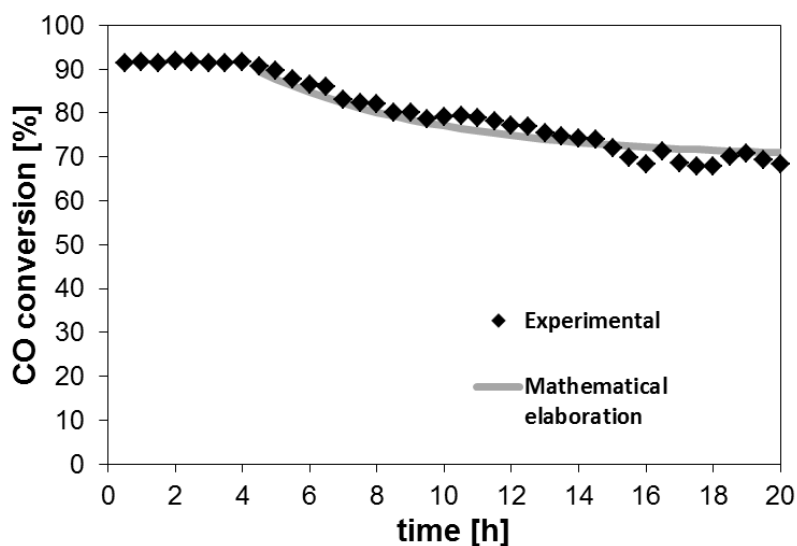


Figure 77 Stability test on the W.Ce/Pt (s) structured catalyst: experimental data and mathematical elaboration

The test has been conducted at atmospheric pressure and at an inlet temperature of 260°C. The reactant mixture was composed by 8 vol% of carbon monoxide, 30 vol% of water and nitrogen balance, and the WHSV, with respect to the carbon monoxide mass flow rate, was set up to 1.7 h⁻¹; these operative conditions were chosen in order to accelerate deactivation.

The results of the stability test are reported in Figure 77.

Overall, the W.Ce/Pt(s) showed only a partial deactivation, and this behavior is largely confirmed in other works already present in the literature (Luengnaruemitchai A., 2003). More in details, the W.Ce/Pt(s) was quite stable during the first 4 hours of reaction, showing a conversion around 91 %, then deactivation started to occur, up to a CO conversion value of about 70 % after 20 hours, after that the system become stable. In particular, the curve of deactivation, which goes from 4th to 20th hour of time on stream, can be simulated by a mathematical equation that can be represented by a negative exponential behavior (22).

$$X_{CO} = A * \exp (-kt) + B \quad (22)$$

Where:

$$A = 44; B = 69.8; k = 0.18 \text{ h}^{-1}.$$

These numerical coefficients were calculated by means of an optimization step driven by the Least Squares Method. By using this mathematical equation, it is possible to understand that the minimum conversion reachable is 69.8%; this value is very close to the conversion value reached after 20 hours of time on stream. So, it can be assumed with high confidence that the experimental results are compatible with a steady state situation in which the catalyst becomes stable.

The reason of the partial deactivation of W.Ce/Pt(s) may be due to the active species crystallites sintering, as reported in the literature for ceria supported platinum based catalysts, when Pt loading is more than 0.5%. In order to understand the reason of the partial deactivation of W.Ce/Pt(s), after the stability test the exhausted sample was analyzed by XRD analysis. In Figure 78 the XRD pattern of this sample is shown, compared with the fresh one.

For the exhausted sample it is possible to observe around 38.5° of 2θ a new peak, which is not present in the pattern of the fresh catalyst. This peak has been attributed to platinum. Moreover, by applying the Scherrer equation to this peak, it is possible to evaluate the mean crystallites dimension.

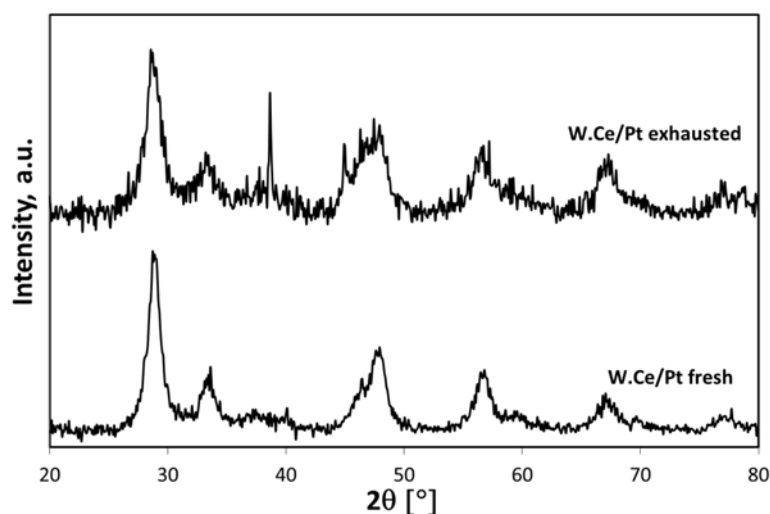


Figure 78 X-Ray Diffraction of the exhausted structured catalyst, compared to the fresh catalyst.

In this case, the platinum presented crystallites dimension in the order of 31 nm. No change was found in the crystallites dimension of ceria and alumina with respect to the fresh catalyst. From these results, it can be affirmed that the main deactivation cause of the W.Ce/Pt(s) sample is the sintering of the platinum particles, this partially covering the active sites of the active species of the catalyst, and loss of active surface area for the WGS reaction.

VII.8 Influence of the structured carrier on the performances of the WGS process in a “quasi-adiabatic” system

VII.8.1 Development of the “quasi-adiabatic” system

In order to evaluate the influence of the thermal transport properties of the foams on the WGS reaction, a laboratory system able to avoid thermal dispersions was set up.

The thermal dispersions in a typical set up can be divided in two types: radial and axial dispersions. In order to limit radial dispersions, the reactor (the same one already used for the activity and selectivity tests) was inserted inside a furnace (40 cm) with three independent thermally controlled zones. The thermal control was used to guarantee the minimum driving force, or the temperature difference between the reactive mixture and the surface of the reactor. On the other hand, in order to limit the axial dispersions, which are very crucial to be reduced because of the inertial motions of the gaseous flow, the system was built as here explained. For what concerning the feed

section, the reactants, both liquid and gaseous ones, were mixed and passed into a metallic tube heated by a constant heat flux. The length of the metallic tube was developed with the aim of ensuring the complete vaporization of the liquid water and the perfect mixing between reactants at the reactor inlet section.

Instead, also the reactor outlet zone was heated by a constant heat flux, and the length of this zone was set up in order to limit or avoid the dispersions in this section.

VII.8.2 WGS reaction in the “quasi-adiabatic” system: influence of the foams and foams density comparison

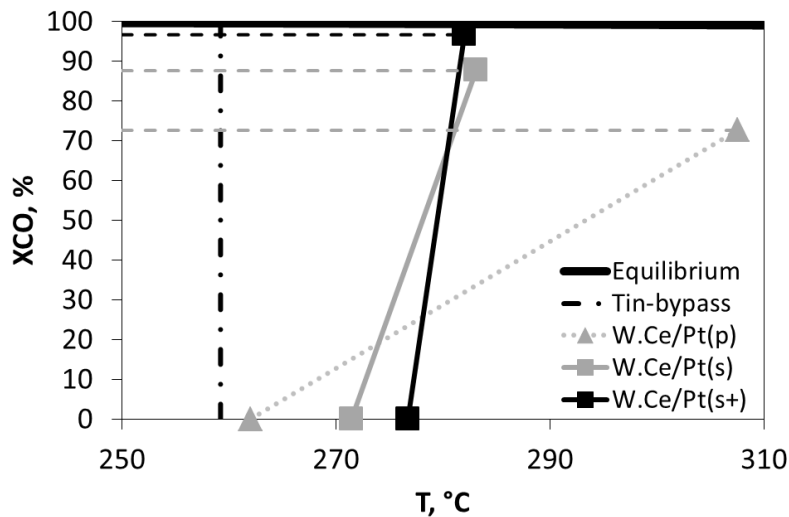


Figure 79 CO conversion versus temperature; comparison between W.Ce/Pt(p), W.Ce/Pt(s) and W.Ce/Pt(s+). Nearly adiabatic conditions (reactor diameter, D : 0.17 m; L/D : 5.2; CO molar concentration at the reactor inlet: 8%; water / CO ratio: 3.75; N_2 balance; linear flow velocity: $18.2 \text{ cm} \cdot \text{s}^{-1}$; gas inlet temperature: 259°C).

The experimental set up illustrated in Section VII.8.1 was used to drive a WGS reaction in the following conditions: inlet $T = 260^\circ\text{C}$, $P = 1 \text{ atm}$, CO molar fraction = 8 vol%, H_2O molar fraction = 30 vol%, N_2 balance, $WHSV = 2.4 \text{ g}_{CO} \cdot \text{g}_{cat}^{-1} \cdot \text{h}^{-1}$, linear flow velocity = $18.2 \text{ cm} \cdot \text{s}^{-1}$.

Figure 79 shows the comparison, in terms of CO conversion, between the catalyst in powder form and the structured catalysts on two different foams. As concerns the catalyst in powder form (W.Ce/Pt(p)), the CO conversion is about 70 % and the temperature difference between outlet and inlet is around 45°C . Moreover, the foam catalyst W.Ce/Pt(s) showed a

higher conversion, around 90 %, and the temperature difference is equal to 12 °C. This behavior is due to the presence of the metallic foam, which is able to axially redistribute the heat generated during the reaction, by increasing the inlet temperature and decreasing the outlet temperature. This condition leads to faster kinetics at the inner part of the catalyst, and this reflects on a higher CO conversion with respect to the catalyst in powder form.

In order to enhance the heat redistribution along the catalytic bed, W.Ce/Pt(s+) was performed in the same system and the same conditions. The main differences between the two types of foams is due to its density, which is higher (rel. dens.: 10-12%). In fact, as shown in Figure 79, the W.Ce/Pt(s+) showed a temperature difference between outlet and inlet of about 5 °C, and a CO conversion which was next to the equilibrium value. In this case, the catalyst inlet temperature was even higher than the W.Ce/Pt(s), and this condition has been the main reason for the high CO conversion. In fact, it has to be considered that the kinetics is faster in the inner zone and the most of the CO conversion occurs in that zone. So, by increasing the redistribution of the heat of reaction through the use of high conductive Aluminum carriers (high relative density), it is possible to obtain an adiabatic “quasi-isothermal” system, leading to higher CO conversion by processing the same reactive flow and the same catalytic mass.

VII.9 Study on the influence of the foam geometry on the

backdiffusion of the heat of reaction

VII.9.1 Activity and selectivity tests on aluminum foams with constant density and different porosity

This important characteristic of structured foam catalysts was investigated. In particular, the performances of different types of foam were investigated, with the same relative density but different porosity. The aim of this tests was to verify how the geometric parameters of the foams can influence the backdiffusion of the heat of reaction along the structured catalyst.

So, three different structured catalysts were prepared, by means of using three aluminum foams, in particular:

- 40 pores per inch (PPI), relative density: 10-12 %;
- 20 pores per inch (PPI), relative density: 10-12 %;
- 10 pores per inch (PPI), relative density: 10-12 %.

The chemical formulation of the catalysts was, as usual, 1%Pt/20%CeO₂/γ-Al₂O₃.

The tests were performed at atmospheric pressure, in a temperature range between 200°C and 400°C. The reactive mixture was composed by 8 vol% of CO, 30 vol% of H₂O and N₂ balance. The 1%Pt/CeO₂/γ-Al₂O₃ foam catalysts were surrounded by a thermo-expanding pad and then inserted into the reactor, in order to avoid gaseous reactants mixture by-pass. The Weight Hourly Space Velocity (WHSV) was set to 1.2 h⁻¹, with respect to the CO mass flow rate. Water was vaporized before entering the reactor and previously mixed with the gas phase. The products mixture generated by the reaction was continuously analyzed by two different devices: the infrared detector “ABB Uras 14” for CO, CO₂ and CH₄, and the thermal conductivity detector “ABB Caldos 17” for H₂.

The results of these tests are shown in Figure 80, in terms of CO conversion as function of the reaction temperature.

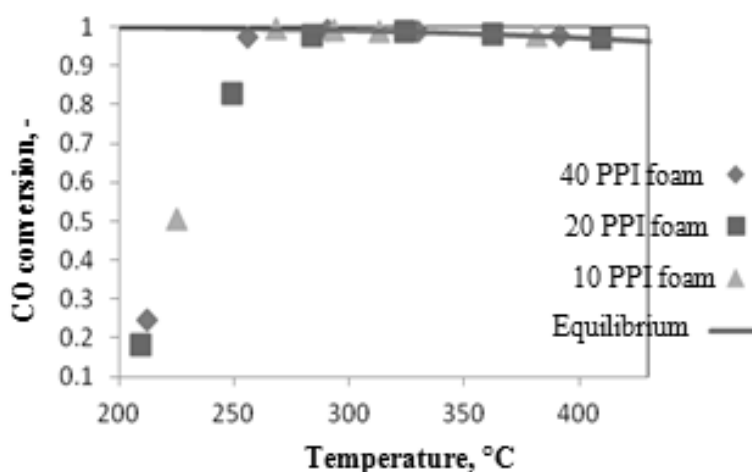


Figure 80 Activity and selectivity tests on aluminum foams with constant density and different porosity

The activity shown by the different structured foam catalysts by using these operative conditions are in general very similar. The main difference can be noted in a temperature range around 250°C. Indeed, at this temperature the 10 PPI foam catalyst reached a CO conversion very close to the equilibrium value (97%), while the 20 PPI foam catalyst stood at a lower conversion value (between 80% and 90%), reaching the equilibrium only above 270°C. Moreover, the 40 PPI foam catalyst showed a similar behavior to the 10 PPI catalyst. Overall, the behavior shown by these three foam catalysts could in some way be influenced by the different geometric conformation, which might also influence the thermal conductivity of the carriers. Anyway, this feature will be investigated deeper in the following paragraphs.

In addition to what already presented, in Figure 81 the molar concentration trend of the gas species, as function of temperature, is shown.

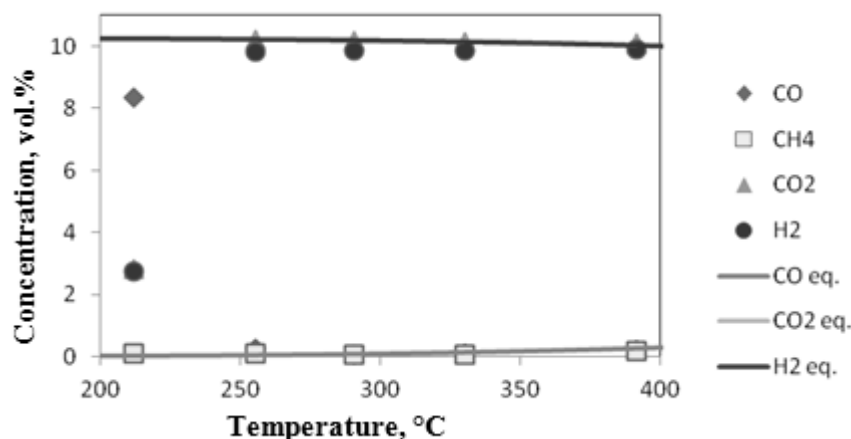


Figure 81 WGS activity of the structured catalyst (aluminum foam: 40 PPI, rel. dens.: 10-12%). Temperature dependence of molar fraction of the components (based on a dry mixture). CO inlet molar concentration: 8 %; H_2O/CO ratio: 3.75; N_2 balance; $WHSV = 1.2 h^{-1}$

The data shown in the Figure 81 are from 40 PPI foam catalyst. They reflect the CO conversion data. In addition, it can also be noted that only few ppm of methane were detected, this being a sign that the catalyst was very selective for the Water Gas Shift reaction. The gas species concentration trend of the 20 PPI and 10 PPI foams are not shown, but they are qualitatively similar to those of the 40 PPI, also in terms of WGS selectivity.

VII.9.2 WGS reaction in the “quasi-adiabatic” system: influence of the geometric parameters (porosity) of the foams

The “quasi-adiabatic” system already developed in Section VII.8.1 was used to perform a Water Gas Shift reaction in the same operative conditions as Section VII.8.2. These tests were made in order to study how the different open-celled structure of the foams can influence the back distribution of the heat of reaction. The results of these tests are shown in Figure 82.

It is clear by looking at the figure above that the 10 PPI foam catalyst showed the best performances, followed by the 40 PPI and the 20 PPI in turn. In particular, the results can be summarized as follows: the 10 PPI reached a CO conversion of 98.9% with a ΔT of 4°C ($T_{in} = 279^\circ C$; $T_{out} = 283^\circ C$); the 40 PPI showed a ΔT of about 6.5°C ($T_{in} = 277.5^\circ C$; $T_{out} = 284^\circ C$) and a CO conversion of 98%; the 20 PPI stood at a CO conversion of about 95%, with a ΔT of more than 10°C ($T_{in} = 274^\circ C$; $T_{out} = 284.5^\circ C$).

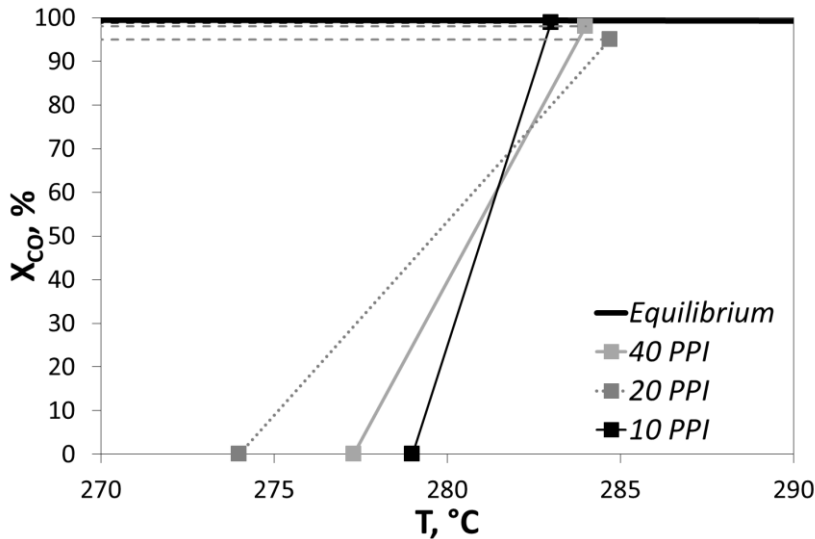


Figure 82 CO conversion versus temperature; comparison between 40 PPI, 20 PPI and 10 PPI foams. Relative density: 10-12% for all foams.

Actually, the 40 and 10 PPI foam catalysts showed similar behavior, with the collected data which can be considered equal if considering the experimental error; on the contrary, the 20 PPI foam catalyst showed a sensibly higher ΔT , associated with a lower CO conversion.

The obtained results can appear surprising, considering that the tested samples had the same amount of solid aluminum (the density was the same for all the foams). So, the only reason for such different performances could lie into the geometric parameters linked to the porosity of the foams. In fact, it is well known that two metal foams with the same relative density but different PPI could have very different thermal conductivity (Groppi G., 2007).

A typical high porosity metal foam has an open-celled structure composed of dodecahedron like cells, known as “the Kelvin Cell”, which as 12-14 pentagonal or hexagonal faces. The edges of these cells are composed of metal fibers and, typically, there is a lumping of solid material at the intersection of fibers. The cross-section of a metal fiber is a function of porosity, and changes from a circle at $\varepsilon = 0.85$ to an inner concave triangle at $\varepsilon = 0.97$ (Leyda B., 2000)

Mainly, there are four geometric parameters that can influence the conduction in a high porosity metal foam (Table 15):

- The cell size (D);
- The fiber length (L);
- The fiber thickness (t);
- The radius of the lumping of solid at the intersection between two or more fibers (R).

Table 15 Mainly geometrical parameter of metal foam

Foam	D, mm	L, mm	t, μm	R, mm	t/R
10 PPI	3.24	4.52	73.8	0.84	0.088
20 PPI	2.10	5.04	53.8	0.73	0.074
40 PPI	1.36	2.42	48.8	0.48	0.102

(Bhattacharya A., 2002) proposed a model for estimating the effective thermal conductivity coefficient of high porosity metal foams, based on the knowledge of the parameters reported above. They considered the lumping of solid aluminum at the intersection having a spherical shape, and considered that the unit cell of the foam consisted of 5 different layers in series. In each layer the solid and the fluid phase are in parallel. The effective thermal conductivity, k_e , is then simply the thermal conductivities of the individual layers in series. A geometric representation of an exagonal cell with a circular lumping of solid aluminum at the intersection of two cells is shown in Figure 83.

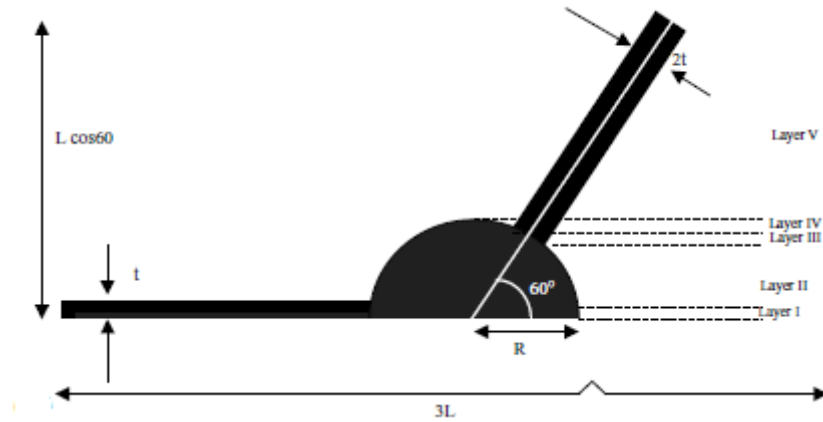


Figure 83 Unit cell for the circular intersection (Bhattacharya A., 2002)

So, by considering the different features of the three aluminum carriers, in terms of cell size, fiber length and thickness, and radius of the lumping of solid, the effective thermal conductivity coefficient of the foams can be estimated by means of using the model described above. The results are reported in Table 16.

It is clearly evident that the 40 and 10 PPI foams had very similar thermal conductivity, while the 20 PPI foam is much less conductive than the other ones.

Table 16 Foams thermal conductivity

Foam	Conductivity [W/m/K]
10 PPI	30.9
20 PPI	8.3
40 PPI	31.1

This result reflects exactly what already observed for the WGS tests in the “quasi-adiabatic” system. In fact, the 20 PPI foam catalyst, which is the less conductive sample, showed the lower CO conversion and the higher ΔT . The reason for this behavior lies in the size of the lumping of aluminum material at the fibers intersection. In fact, by doing investigations with the optical microscope, the 20 PPI foam showed the lower ratio between fiber thickness and radius of lumping at the intersection (0.074) compared to that of the 40 and 10 PPI (0.102 and 0.088 respectively).

This result indicates that, by keeping constant the solid material in the foams, the t/R ratio highly influence the conduction inside the structure. In fact, when the solid material agglomerates in the intersection points between the fibers, the t/R ratio becomes lower, and so the thermal conductivity.

Anyway, although differences have been registered in the performances of these types of aluminum foam catalysts, the tests made have demonstrated the very efficient activity of the prepared structured catalysts, which are all able to reach very high CO conversion, close to the equilibrium value, by operating at relatively low temperatures, and with a very reduced ΔT , approaching the concept of “WGS adiabatic quasi-isothermal reactor”

Chapter VIII. CFD modeling of the WGS adiabatic system

In this chapter a CFD modeling, based on the finite elements method, of the WGS adiabatic system is presented. It is just a basic modeling, based on standard assumptions, and the aim of this chapter is to validate what has been obtained in the last chapter, i.e. to demonstrate that the use of a high conductive aluminum foam catalyst can lead to a redistribution of the WGS heat of reaction along the structured bed, with an increasing in CO conversion in only one adiabatic stage. The comparison, as usual, will be done between the structured foam catalyst (with high thermal conductivity) and a conventional packed bed adiabatic reactor. The efficient modeling of the system, though it might be basic, could be a good benchmark for the design of a scalable system in view of an application of the investigated technology. The process has been modeled coupling transport phenomena and reaction kinetics. The reactor model is implemented exclusively with the CFD.

In the reactor modeling several advancements have been achieved in the last 15 years, simultaneously with the spreading of more and more powerful calculators. Often, theories used in these works are being seized from the past, when reduced computational equipments forced researchers to develop simplified models. Nowadays, many of those simplifications are dropped, and efforts are being made to renew some well-established techniques based on outdated hypotheses. Furthermore, a modern approach to reactor modeling bases its fundamentals on Computational Fluid Dynamics (CFD), approaching the equipments characterization with a detailed, multi-dimensional description, as a continuum, of the whole flow field and other phenomena occurring; adjusting the new multiphase or reactive flows tools, as well as turbulence and particle description.

The actual geometry of the reactor is responsible for the changes taking place in the fluid flowing through it. The complete description of the flow field would give a very precise solution of all the phenomena occurring in the reactor. Unfortunately that requires handling a complex system of partial

Chapter VIII

differential equations, which is sometimes hard to solve, particularly if the geometry is complicated.

For chemical engineering needed anyway solutions, traditionally the problem was dealt using lumped models, where all the dimensions but one were discarded and replaced by a description of what happens near the surface and in the bulk of the fluid. The farther the particles move away from the surface, the fewer it affects them. This produces a thin layer of fluid near the surface, called boundary layer, in which either the velocity or the composition or the temperature changes from zero at the surface to the free stream value (the mean bulk gas) away from the surface. Constituent quantities describing these zones are related with a function of the driving force between them, namely a linear contribution in the constituent equations such as a transport coefficient times the difference in the balanced quantity. Transport coefficients can then be obtained either from experiments on the actual facility or from the literature correlations, given as generalized coefficient through dimensionless numbers.

In the past century this analysis was made for simplified reacting systems: a single first order kinetic. This way, it was straightforward to extend heat transport coefficients (the more easily and extensively investigated) to the mass transport ones. This 1st order kinetic assumption is very particular, and can no longer be borne. Modern techniques are now available and allow looking inside the problem in a more general and realistic way, deriving correlations for mass transfer in reacting and developing laminar flow with arbitrary kinetics.

VIII.1 Modeling of the system: CAD and geometry

The system has been modeled by using the finite element software COMSOL Multiphysics 5.0 (the license is available at the Department of Industrial Engineering of the University of Salerno, License number: No.13073437,00-0f-fe-0a-73-34). COMSOL Multiphysics is a finite element analysis, solver and Simulation software / FEA Software package for various physics and engineering applications, especially coupled phenomena, or multiphysics. The package is cross-platform (Windows, Mac, Linux). In addition to conventional physics-based user interfaces, COMSOL Multiphysics also allows for entering coupled systems of partial differential equations (PDEs).

By using the COMSOL CAD environment, a simplified geometry of the real system has been built. Indeed, because of a cylindrical geometry, by assuming that transport parameters do not change along the tangential coordinate, it was possible to reduce the volume domain to $\frac{1}{4}$ of the real one. The built geometry is shown in Figure 84

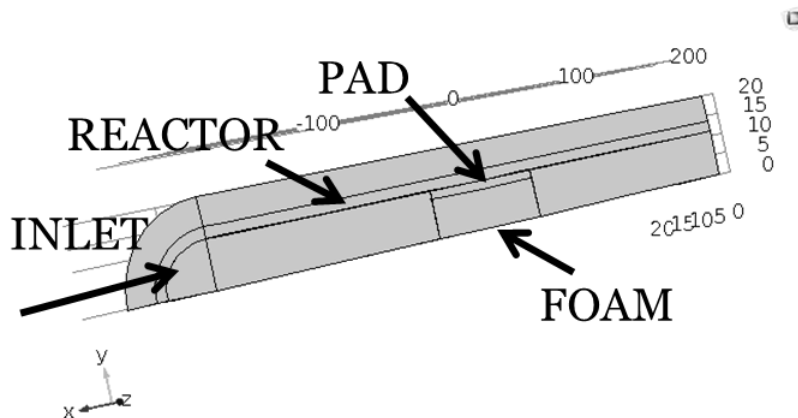


Figure 84 Simplified geometry of the real system

In the picture above, the gas stream flows axially, along the z-coordinate, through the reactor (internal diameter of 22 mm, thickness of 2.5 mm). The oven has been simulated by a cylinder with a diameter of 40 mm. The catalytic zone was put in the middle of the reactor (catalyst diameter of 16.5 mm), surrounded by the thermo expanding pad. The length of the catalytic zone was set to 88 mm, while the total length of the reactor was 400 mm.

The final mesh, after an independent study based on the knowledge of the physics indicated in the following paragraphs, was constituted by 110882 volume elements, 16408 boundary elements and 945 elements on edges.

Another important feature of COMSOL is that any domain, or part of it, can be assigned to an appropriate material, and COMSOL has a very big library of materials with also a lot of chemical and physical properties already implemented. In particular, the most of these properties are implemented in COMSOL also with their dependence from variables such as temperature, pressure, etc. For what regards the specific case of the system under investigation, the oven atmosphere was simulated as it contains still air (in this environment only natural convection can exist). The reactor was composed by a steel AISI 310 alloy, and properties such as density, thermal conductivity and heat capacity were known, as function of temperature. The thermo expanding pad was constituted by a Delrin 577 glass fibers, which is a material that has similar properties to the real one.

Talking about the catalytic material, it was simulated by different types of materials, depending on the nature of the catalyst. Indeed, the run set of simulations was composed by tests on a packed bed reactor and tests on a structured foam catalytic reactor. In the first case (powder catalyst), the material properties needed for the CFD simulations were:

- Thermal conductivity, k : 0.5 W/m/K;
- Density, ϵ : property derived from a material composed by ceria and alumina, as function of temperature;

Chapter VIII

- Heat capacity, cp: 0.204 J/kg/K;
- Porosity, ε : 0.4;
- Permeability, K: $1e-5 \text{ m}^2$;

In the second case (structured aluminum foam catalyst) the catalyst was simulated by a 6101 Aluminum alloy; the material properties were:

- Density, ρ : from material, as function of temperature;
- Heat capacity, cp: 895 J/kg/K;
- Porosity, ε : 0.93
- Permeability, K: $1e-6 \text{ m}^2$
- Thermal conductivity, k: 218 W/m/K.

The remaining part of the entire domain was filled by the gas stream flowing through the reactor. To better model the system, it was decided to simulate only the fluid dynamic first, in order to find the best geometric configuration to apply for the adiabatic system.

VIII.2 Fluid-dynamic modeling

The fluid dynamics simulation was performed by assuming incompressible and isothermal flow (the temperature was set up to 473.15 K), by using the following physics:

FREE AND POROUS MEDIA FLOW: modeling of the structured catalyst bed, together with the reactor zones free from filling components, from the point of view of a thermo-fluid problem, from which the fluid velocity components and pressure can be calculated;

In order to determine the velocity profiles for the domain flow regime, inside the zones free from filling components, steady-state incompressible Navier–Stokes equations (23-24) are used for the momentum balance. So, the governing equations for continuity and the momentum balances could be written as follows:

$$\nabla \cdot u = 0 \quad (23)$$

$$\rho(v \cdot \nabla)v = \nabla \cdot [-pI + \mu(\nabla v + (\nabla v)^T)] \quad (24)$$

Where:

ρ = fluid density, kg m^{-3}

v = velocity vector, m s^{-1}

p = pressure, Pa

I = identity matrix

μ = fluid dynamic viscosity, Pa s

The boundary conditions are as follows: in the inlet section the normal average velocity was fixed (1.3 l/min); on the contrary, at the outlet section atmospheric pressure was fixed. Moreover, no slip boundary condition was considered for all walls of the reactor and the structured catalyst. The porous medium was modeled using the Brinkman equation (25), which can be written as follows:

$$\frac{\rho}{\varepsilon_p} \left((v \cdot \nabla) \frac{v}{\varepsilon_p} \right) = \nabla \cdot \left[-pI + \frac{\mu}{\varepsilon_p} (\nabla v + (\nabla v)^T) - \frac{2\mu}{3\varepsilon_p} (\nabla \cdot v) I \right] - \frac{\mu}{k} v \quad (25)$$

Where:

ε_p = bed porosity

k = bed permeability, m^2

The latter can be calculated easily by the Rump-Gupte equation (26) (Fatehi M., 1994):

$$k = \frac{\varepsilon_p^{5.5}}{5.6} d^2 \quad (26)$$

Where:

d = characteristic dimension of the porous medium.

The main results of the simulation are shown in Figure 85.

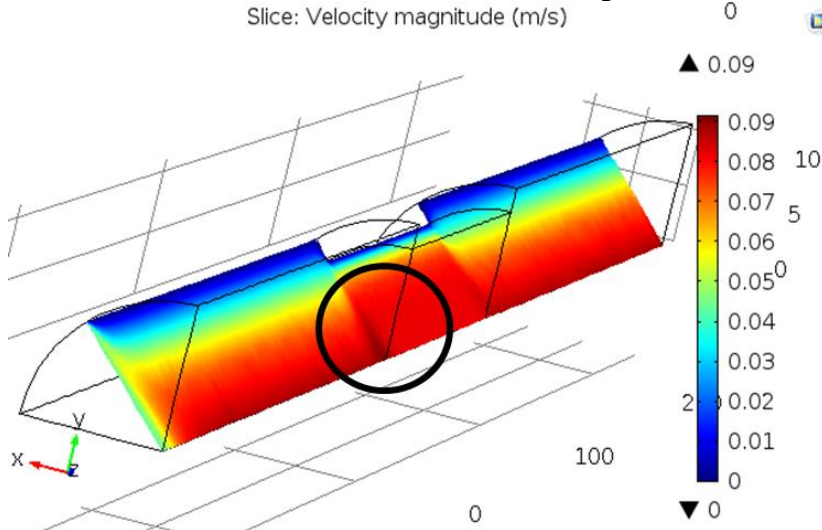


Figure 85 Fluid dynamics simulation (FREE AND POROUS MEDIA FLOW)

Chapter VIII

It is clearly visible (and circled) that with this geometric configuration it appeared an important entrance effect, due to the abrupt restriction of the flow section. Anyway, an important remark is that the velocity profile inside the porous domain is almost completely flat, and the maximum velocity inside it tends to decrease. This is also sign of a flow redistribution, which of course help to increase the heat exchange inside the porous domain.

Anyway, in order to overcome the problem due to the entrance effect, it was run another simulation by changing the geometry; another material was added, in particular one couple of hollow cylinders before and after the porous domain. The results of the simulation of this new configuration are visible in Figure 86.

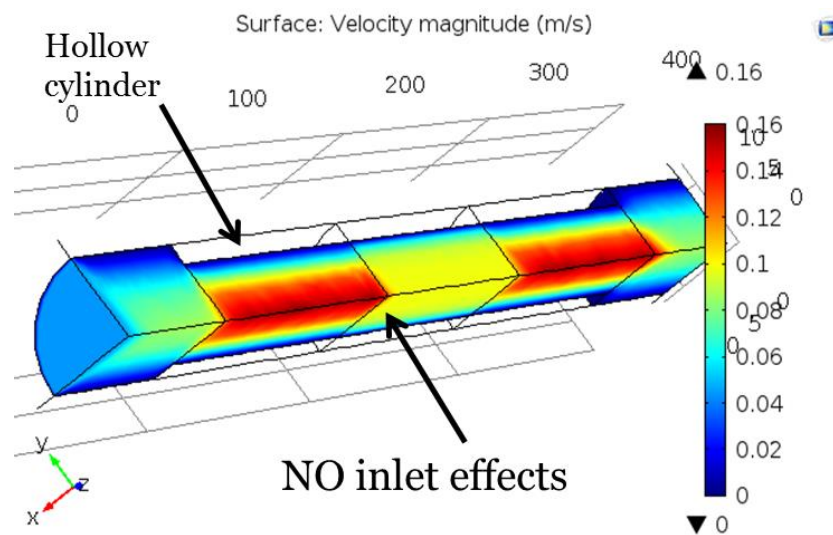


Figure 86 Fluid dynamics simulation couple of hollow cylinders before and after the porous domain

So, it is clear that the addition of the two hollow cylinders allowed to greatly reduce the entrance effect, guaranteeing a more constant axial velocity profile along the porous domain. This result permitted to make sure that effects on the mass transfer due to the flow regime can be neglected.

This developed system was used to model the adiabatic reactor. This modeling will be explained in details in the next paragraphs.

VIII.3 Finite element modeling of the adiabatic reactor

With the new geometric configuration, another simulation was set up, in which the model of the adiabatic reactor was put. The geometric domain that was used for these simulations is shown in Figure 87.

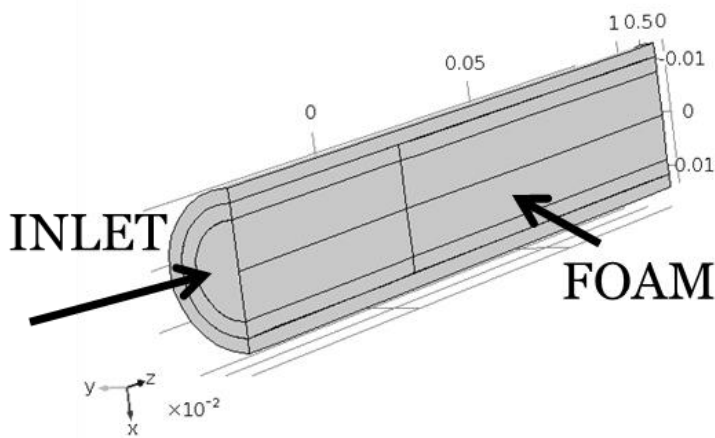


Figure 87 Simplified geometry for modelling the adiabatic system

The model considered the contemporary presence of the 3 transport phenomena: the momentum transfer, the heat transfer and the mass transfer. The equations for the momentum balance are those already shown in Section VIII.2. In order to test the performances of this adiabatic system, the volumetric flow rate of the reactants was increased up to 2400 Ncm³/min.

For what regards the mass (26-27) and energy balance (28-29), the equations are as follows:

MASS BALANCE

$$\nabla \cdot (-D_i \nabla c_i) + u \cdot \nabla c_i = R_i \quad (26)$$

$$N_i = -\nabla D c_i + u c_i \quad (27)$$

Where:

D_i = Diffusivity coefficient of the $-i$ component;

c_i = volume concentration of the $-i$ component;

u = velocity vector;

R_i = reaction velocity of the $-i$ component;

N_i = mass flux of the $-i$ component;

Chapter VIII

ENERGY BALANCE

$$\rho C_p u \cdot \nabla T_i = \nabla \cdot (k_{eff} \nabla T) + Q + Q_{vd_i} \quad (28)$$

$$k_{eff} = \mathcal{G}_p k_p + (1 - \mathcal{G}_p) k \quad (29)$$

Where:

ρ = gas density;

C_p = gas heat capacity;

T = temperature;

k_{eff} = effective thermal conductivity of the porous domain;

Q = heat source of reaction;

Q_{vd} = exchanged heat with external environment;

$1 - \theta_p$ = void fraction of the porous domain;

k_p = thermal conductivity of the porous material;

k = thermal conductivity of the gas phase.

The boundary conditions for the mass balance are as follows:

$$z = 0 \rightarrow y_{CO} = 0.08; y_{H_2O} = 0.3(N_2 \text{ balance}) \quad (30)$$

$$z = L \rightarrow -n \cdot D_i \nabla c_i = 0 \quad (31)$$

Furthermore, the boundary conditions for the energy balance are:

$$z = 0 \rightarrow T = T_{in} = 473K \quad (32)$$

$$z = L \rightarrow -n \cdot k \nabla T = 0 \quad (33)$$

$$Q = R_i \cdot (\Delta H_r) \quad (34)$$

$$Q_{vd} = 0(\text{adiabatic}) \quad (35)$$

The term R_i which appears in the mass balance refers to the reaction velocity of the chemical components that participate to the reaction. So, this term is strictly related to the catalyst kinetics.

In order to make the comparison between the powder and the structured catalyst performances in the adiabatic system, it was decided to hypothesize an elemental kinetics for the simulated system, and the principle kinetic parameters were:

- Pre-exponential factor, $k_0 = 5.06 \text{ e}7 \text{ mol/m}^3/\text{bar}^2/\text{s}$;
- Activation energy, $E_a = 49.75 \text{ kJ/mol}$;
- Heat of reaction, $\Delta H_r = -41.17 \text{ kJ/mol}$.

The used relations are(36-37):

$$R_i = k_r \cdot \left(p_{CO} \cdot p_{H_2O} - \frac{1}{K_{eq}} p_{CO_2} \cdot p_{H_2} \right) \quad (36)$$

$$K_{eq} = \exp\left(\frac{4577.8}{T} - 4.33\right) \quad (37)$$

Where:

K_{eq} = equilibrium constant;

p_i = partial pressures;

k_r = kinetic constant.

VIII.3.1 Modeling of the adiabatic reactor: powder catalyst results

In Figure 88 the results of the mass balance simulation, with regards to the CO, are shown for the powder catalyst modeling. The picture is obtained in terms of CO molar fraction, in a 2D plot built on the same direction as the reactor radius. The most of the reaction happened at the beginning part of the catalyst bed, this phenomenon mainly due to the kinetics. Another thing that can be noted is that the concentration profile along the radial coordinate is not constant, but it describes a parabola, with the maximum in the center of the reactor. This situation could probably have been due to the velocity profile, which is not flat, but also the influence of the mass transfer inside the packed bed (which in turn depends on the velocity vector) can have played a big role. In fact, if looking at Table 17, which reports the diffusion

Chapter VIII

coefficients magnitude of the reactants and products of the WGS reaction, it can be seen that they are very different one from each other.

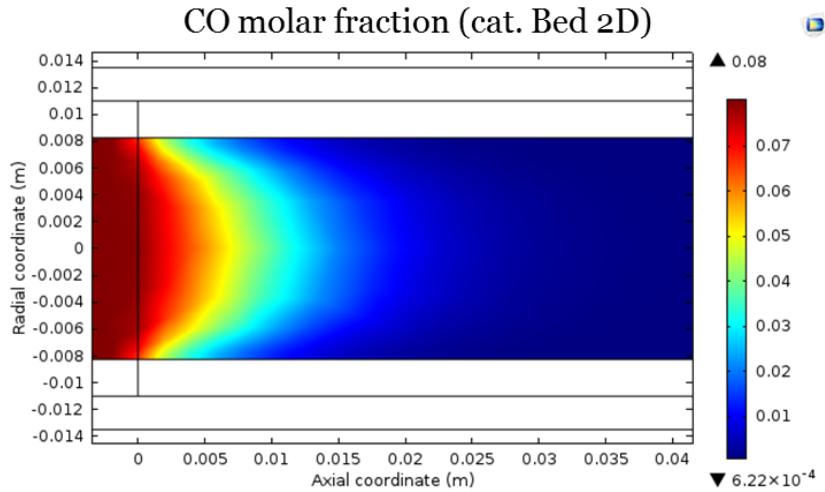


Figure 88 Mass balance 2D simulation, with regards to the CO (powder catalyst)

In particular, the diffusion of H_2 is of one order of magnitude higher than the other species. This leads to a flatter concentration profile for hydrogen with respect to the other species, as can be seen in Figure 89, and this effect of course influence also the conversion of the process.

Table 17 Diffusion coefficients magnitude of the reactants and products of the WGS reaction

	Number	Units of measure
D_{CO}	0.07	m^2/h
D_{H_2O}	0.092	m^2/h
D_{CO_2}	0.058	m^2/h
D_{H_2}	0.26	m^2/h

In Figure 90 a surface plot with the main results of the energy balance for the powder catalyst is reported. It is clearly visible the increase of temperature at the beginning of the catalytic zone. The reactants are at 473 K while the products come out at 586 K (so a $\Delta T > 100$ K). This is what conventionally happen in a WGS adiabatic Low Temperature stage.

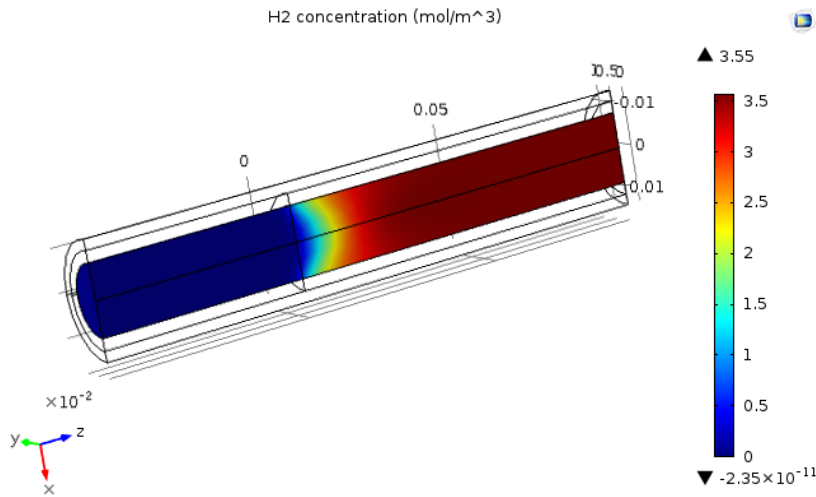


Figure 89 powder catalyst simulation: hydrogen concentration

The black arrows in Figure 90 indicate the verse of the heat flux in the entire domain. It can be seen that the flux is almost zero all inside the catalytic zone, because the catalyst has a poor thermal conductivity and this feature doesn't allow it to walk off the heat of reaction easily. The only backward flux is inside the thickness of the reactor, which in turn tends to heat up the inlet stream, but this is only a weak contribution.

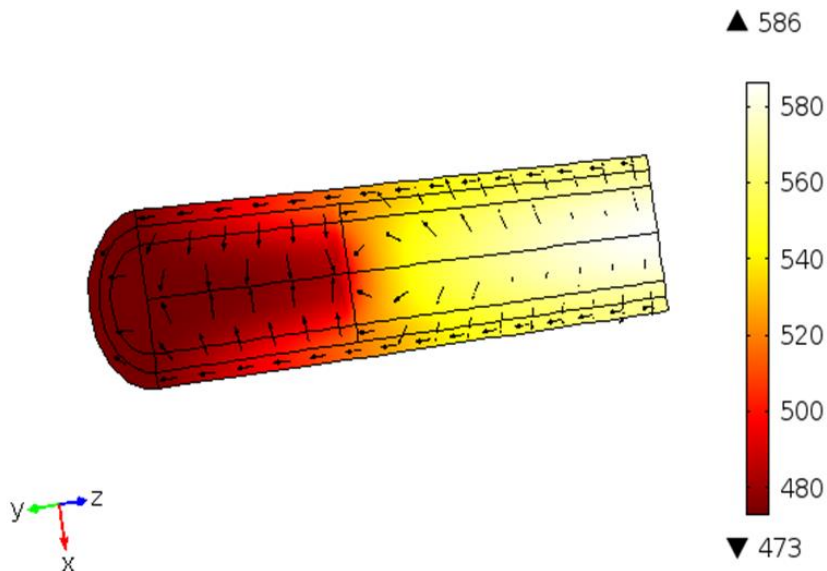


Figure 90 Surface plot of temperature: simulation of the powder catalyst

In Figure a 1D plot along the axial coordinate (Figure 91) makes soon visible the increasing in temperature along the catalytic zone. It can also be

Chapter VIII

noted that the increase in inlet temperature is lower than 10 K, this effect due to the weak contribution of the reactor stainless steel material.

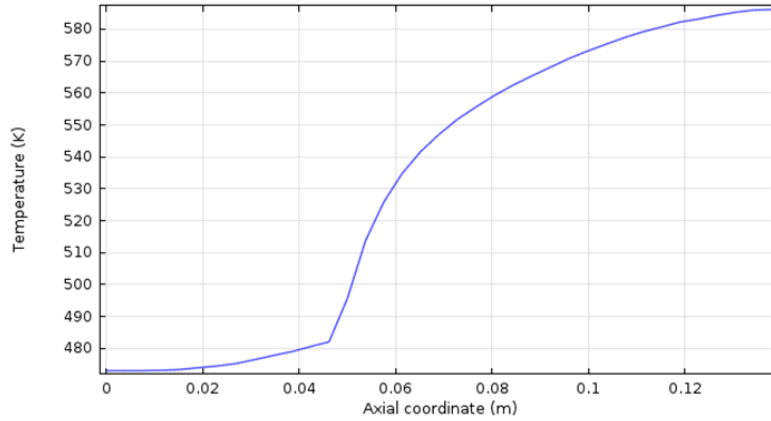


Figure 91 Temperature profile: simulation of the powder catalyst

Overall, this simulation confirmed what conventionally happens in industrial adiabatic WGS reactors, so it can be a good basis for the modeling of the structured foam catalyst.

VIII.3.2 Modeling of the adiabatic reactor: structured foam catalyst

results

In Figure 92 the 2D plot of the CO molar fraction for the case of the structured catalyst is presented.

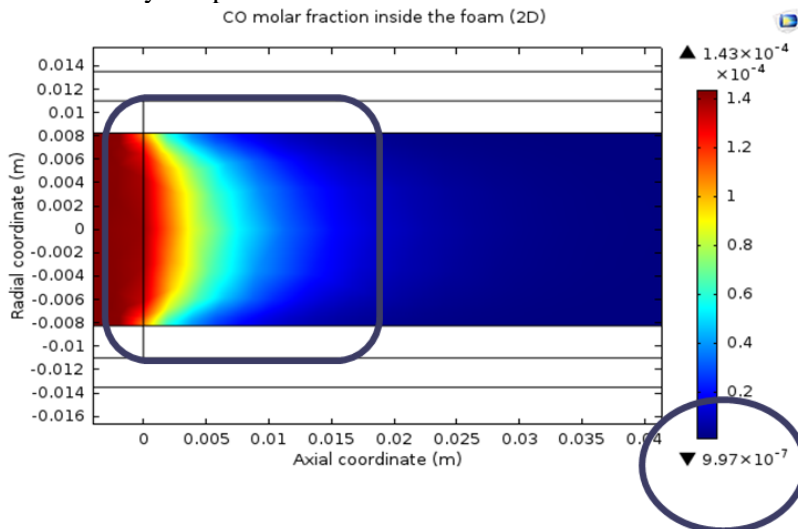


Figure 92 CO molar fraction inside the foam (2D plot)

Actually, this simulation revealed better results for the structured catalyst. Indeed, the high porosity of the foam favors the mass transfer, in terms of diffusion, along the catalytic domain. Moreover, the almost total conversion is reached, and only a little part of the catalyst is needed to obtain it. In fact, the 99% of the conversion is reached after 1.7 cm of catalyst (2.5 cm in the case of powder), this making irrelevant the presence of the remaining part of the foam, with a saving in catalytic volume.

The real advantage of using open cell high conductive aluminum foam is more clear if looking at Figure 93 and Figure 94, which show the main results of the energy balance.

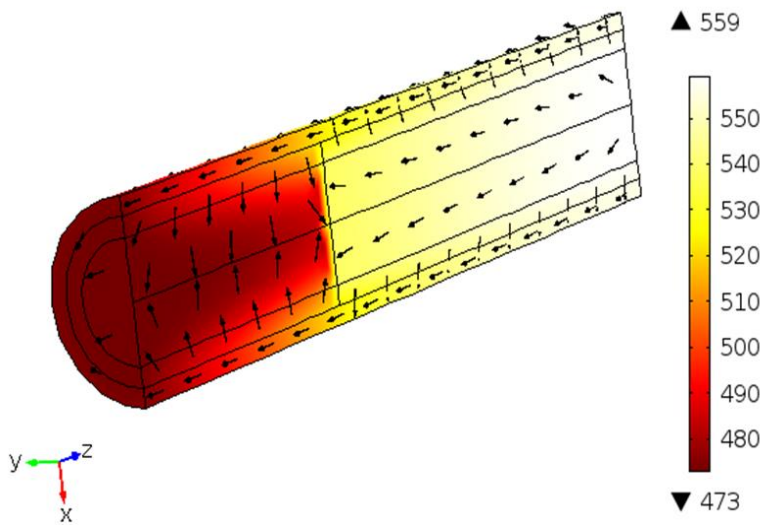


Figure 93 Aluminum foam effect: redistribution of the heat flux

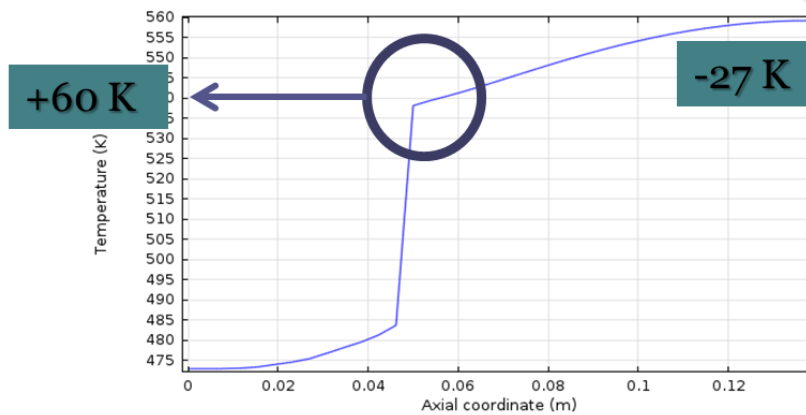


Figure 94 temperature profile: inner and foam section

In particular, in Figure 93 it is clearly visible (black arrows) the back diffusion of the heat of reaction promoted by the presence of a high

Chapter VIII

conductive carrier such as the open cell aluminum foam. This effect reflects on the higher CO conversion reached in a lower catalytic volume, as already explained in Figure 92. Moreover, if looking at Figure 94 it is really evident that the high conduction across the aluminum fibers allowed to increase the inlet temperature of about 60 K and decrease the outlet temperature of about 27 K. So, the ΔT was lower than 20 K (while in the case of the powder catalyst it was higher than 100 K); this result, not only increases the equilibrium conversion, but also ensures that the whole catalytic mass didn't suffer the high temperature differences between inlet and outlet, wherefore this situation can greatly affect the efficiency and the durability of the catalyst.

For completeness, in Figure 95 a comparison in terms of total conductive flux is made between the powder catalyst and the foam catalyst.

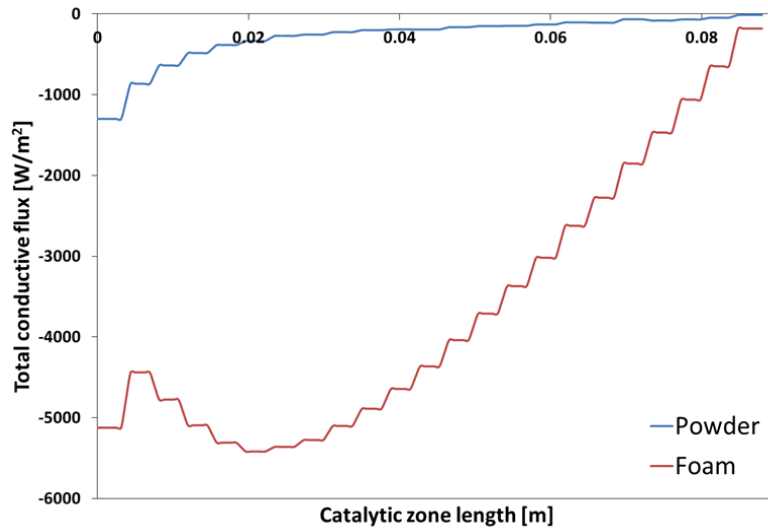


Figure 95 Comparison between the conductivity flux of the catalysts in powder form and structured on foam

While the powder catalyst didn't show any conductive flux (only a weak contribution of the reactor surface in the inlet section), the foam catalyst showed a huge backward conductive flux, which had its maximum of 5500 W/m^2 after 2 cm of catalytic structure. These results are very powerful, and make the application of the structured foam catalysts very promising for the investigated process.

VIII.4 Validation of the adiabatic reactor model: Parametric

Sweep

In order to verify the accuracy of the model explained in the previous paragraphs, a parametric sweep was performed by COMSOL. A lot of parameters were varied, including molar concentrations, temperature, geometric parameters and material properties. Known that it would be long and redundant to show all the results obtained by these parametric sweep, only the variation of CO inlet molar concentration and inlet temperature will be shown.

In Figure 96, the CO conversion (at an inlet temperature of 473 K) as function of foam length and CO inlet molar concentration is shown.

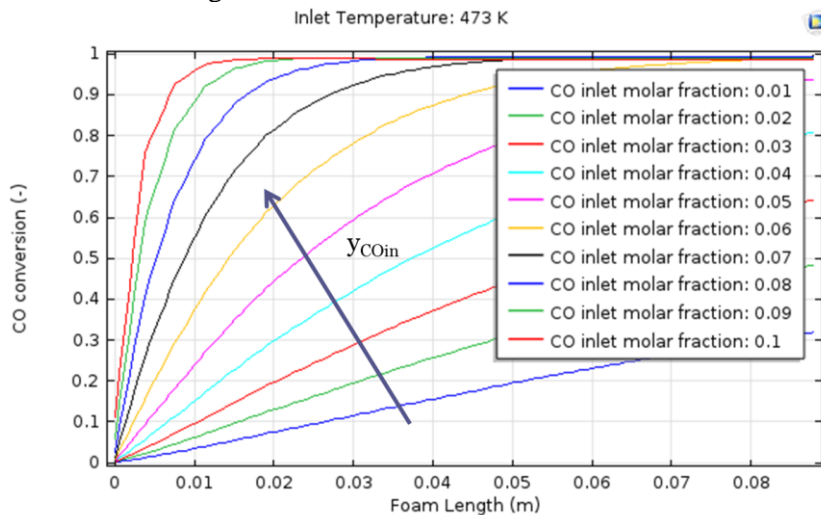


Figure 96 CO conversion along the foam length with different inlet CO molar fraction (inlet $T=473K$)

As it can be observed by looking at the plot, by increasing the CO molar inlet concentration, the CO conversion increased and also the kinetics increased.

Moreover, in Figure 97 the axial temperature profile, as function of the inlet temperature (at constant inlet CO molar concentration) is shown.

The trend of the plot above shows how an increasing in the inlet temperature causes a proportional increase in the absolute temperature profiles (in the range 473-493 K).

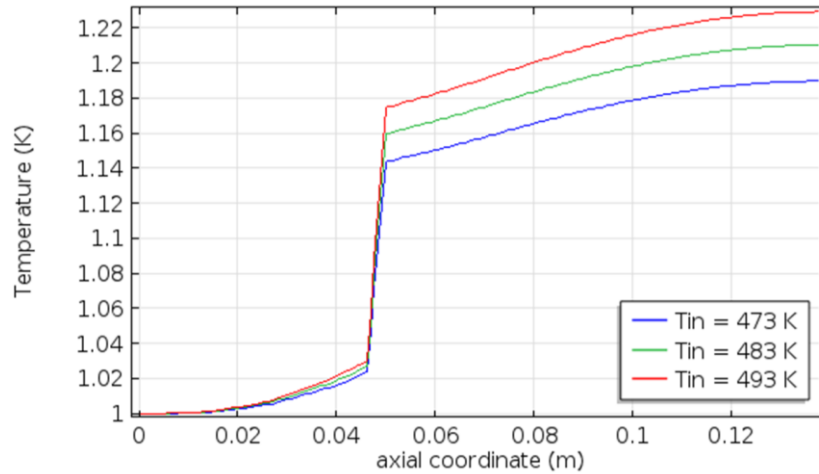


Figure 97 Temperature profile along the axial coordinate with different inlet temperature ($y_{CO,in}=0.08$)

VIII.5 Comparison between the performances of the two reactor systems in view of a process intensification

In this paragraph a comparison between the simulation of the packed bed and the simulation of the structured foam catalyst is presented. A new set of simulations has been run, by varying the mass of catalytic domain while keeping the flow rate constant. In this way, it was possible to simulate different contact times, to see how the two reactor systems answered to this variation. The total flow rate was set up to $2400 \text{ Ncm}^3/\text{min}$ and the CO molar concentration was 8%, with a 30% of water and N_2 balance.

A first set of simulations has been run by fixing the inlet temperature at the value of 200°C . Some results are shown in Figure 98 and Figure 99.

In the first plot (Figure 98), which is obtained for a contact time of 214 ms, the performances of the two systems, at least in terms of CO conversion, seemed to be very similar. In fact, although the foam catalyst allowed to reduce the adiabatic ΔT from 71°C to about 13°C , the conversion value remained very close (99.1% for the foam, 98.8% for the powder). Here the only difference is due to the maximum equilibrium conversion that the outlet temperature allowed to reach; in this range of T, the equilibrium conversion doesn't change drastically.

In order to stress the catalytic system, the contact time was then set to 107 ms (Figure 99). With this operative condition, the advantages arising from the use of a high conductive foam begin to glimpse. The low contact time exploit the fast heat transfer inside the high conductive material.

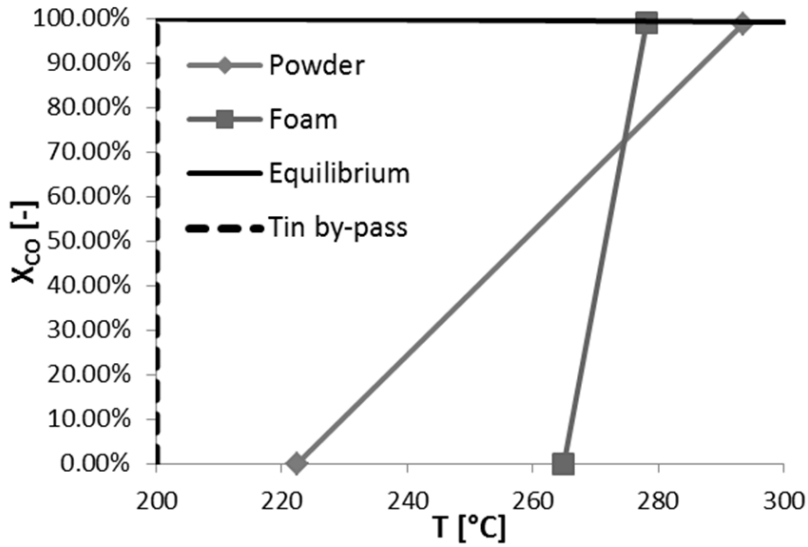


Figure 98 COMSOL simulation: comparison between foam and powder ($T_{in} = 200^{\circ}\text{C}$; contact time: 214 ms)

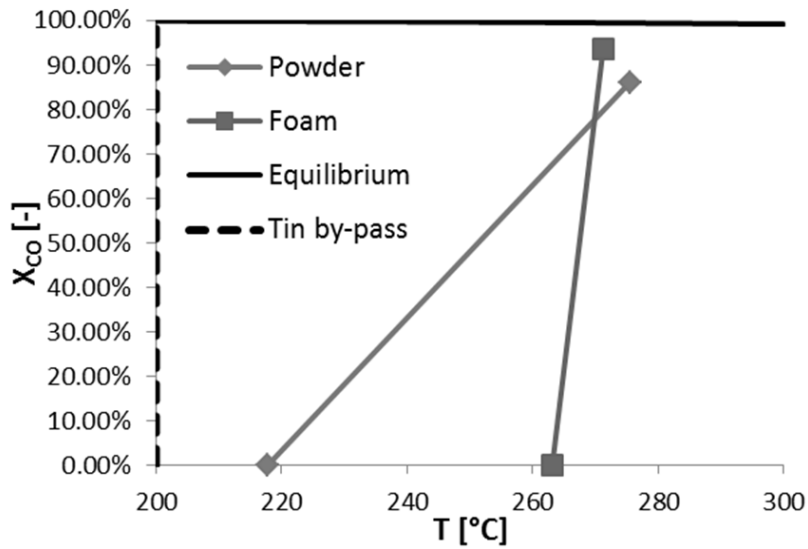


Figure 99 COMSOL simulation: comparison between foam and powder ($T_{in} = 200^{\circ}\text{C}$; contact time: 107 ms)

Indeed, the powder system reached an adiabatic ΔT of about 58°C , and a CO conversion of 86.1%. However, the foam system reduced the adiabatic ΔT to 8°C , and the CO conversion was sensibly higher than that showed by the powder system (93.7%).

Chapter VIII

Moreover, the difference between the performances of these two reactor systems can be more visible by increasing the “ T_{in} by-pass”, i.e the temperature at which the reactants enter the reactor, from 200°C to 220°C. The main results are reported in Figure 100 and Figure 101.

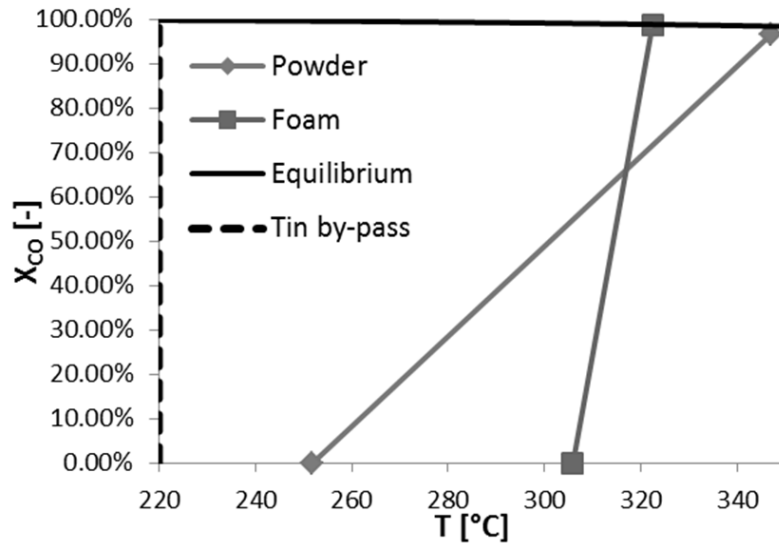


Figure 100 COMSOL simulation: comparison between foam and powder ($T_{in} = 220^{\circ}\text{C}$; contact time: 214 ms)

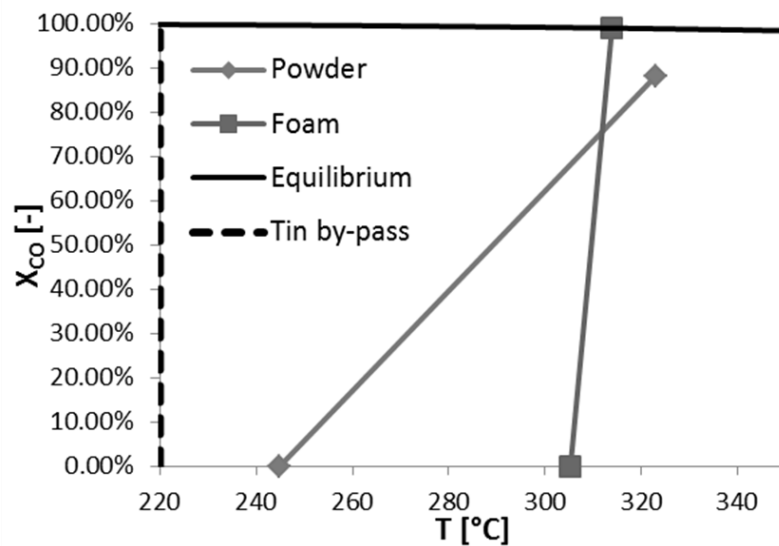


Figure 101 COMSOL simulation: comparison between foam and powder ($T_{in} = 220^{\circ}\text{C}$; contact time: 107 ms)

In particular, at 214 ms the powder reached a CO conversion of 96.5%, while the backdiffusion of the heat of reaction made by the aluminum foam brought this system to a conversion of about 98.8%. The difference was even more pronounced at a lower contact time (107 ms), where the CO conversion reached by the powder system was 88%, while the foam still showed equilibrium conversion (98.85%).

This results obtained by the simulation modeling made with COMSOL indicate that an intensification of the Water Gas Shift process made by the use of a structured catalyst with high thermal conductivity is possible, and the simulations also confirmed what already observed in the experimental tests made in Chapter VII. The application of this relatively new technology could bring to a reduction in fixed and operating costs (only one WGS stage and no inter-cooling) in the Water Gas Shift section of a hydrogen production plant, being a springboard for the use, in future, of hydrogen as commonly used fuel.

Chapter IX. Conclusions

The influence of using a high thermal conductivity structured catalyst for the intensification of the Water Gas Shift process was investigated. In order to reach the desired heat transfer properties, metal foams were chosen as structured carriers.

A mathematical model, developed on the basis of other similar heat transfer models accounted for honeycomb monoliths, was used to estimate the thermal conductivity and the gas phase heat transfer coefficient of the structured supports. An experimental set up was built to make heat transfer tests on different types of metal foams. Between the investigated samples, aluminum showed the most flat thermal profile, sign of a good redistribution of the heat along the monolithic bed. The alumina foam also showed a quite flat thermal profile, but it must be considered that its relative density is much higher than the other samples, and its pore density is very high. From the results obtained by the optimization of the mathematical model, aluminum foam (relative density: 6-8%, pore density: 40 PPI) was the most conductive sample (30 W/m/K at 200°C), and its thermal conductivity was of one order of magnitude higher than the other metallic sample's one

So, aluminum foam was chosen as the most promising structured carrier, showing an excellent heat exchange with heat redistribution along the fibers structure.

A second phase of the PhD project was dedicated to set up an experimental campaign in order to find the best catalytic phase to anchor to the aluminum structure. Different platinum based catalysts, supported on ceria, ceria-zirconia and ceria-alumina were prepared, through the wet impregnation method, followed by drying at 120°C and calcination in muffle at 600°C. From the characterization of the samples, it was detected that the specific surface areas recorded for all catalysts showed that the addition of the active species did not involve a substantial decrease of the s.s.a. Moreover, the crystallite size of all samples was lower than 10 nm, this indicating a good dispersion of platinum in all the prepared catalysts. The TPR profile of the 1%Pt/CeO₂-ZrO₂ sample revealed a higher reducibility of this catalyst with respect to the other investigated samples. This last feature reflected on the results of the WGS tests, made at atmospheric pressure, with

Chapter IX

a CO inlet molar concentration of 5 % ($\text{H}_2\text{O}/\text{CO}$ at inlet: 5; helium balance) in a range of temperature between 150°C and 400°C, with a gas hourly space velocity of 5000 h^{-1} . All the samples showed a very good activity for the WGS, but the 1%Pt/CeO₂-ZrO₂ sample showed the best performances (at 180°C still equilibrium conversion). In particular, 1%Pt/14%CeO₂/ γ -Al₂O₃ approached the equilibrium in the range 240-400°C, but at 200°C the conversion was 5 %. The same happened for the 1%Pt/CeO₂ sample; at 200°C its conversion was still very high (> 90%), but at 180°C it decayed to lower than 20%.

The 1%Pt/CeO₂-ZrO₂ catalyst was then tested under different flowing condition (at different GHSV), and under 80 hours of time on stream. This catalyst showed an excellent activity, also at high space velocity, both in terms of conversion that selectivity. A slight reduction in catalytic activity did not affect the very good performance of the proposed formulation. Moreover, the results of the time on stream test revealed that, under the selected operative conditions, typically very stressful for the WGS catalyst, the CO conversion during the first 40 h decreased from an initial value of 75 % to a value of 50 %, then the conversion did not change anymore. The main reasons for this behavior were assumed to be due to sintering phenomena, which may have causes the initial deactivation, leading to a constant value of the CO conversion when sintering was completed, so stabilizing the catalyst.

The structured catalysts are usually prepared by deposition of a catalytic formulation on the structured carrier, sometimes modified by the deposition of a washcoat formulation. So, another aim of this PhD thesis was to find the best formulation for a washcoat, in order to allow the deposition of the active species on the aluminum foam. A first washcoat formulation was prepared by employing the ceria-zirconia solid solution mixed with alumina (ratio: 8/1). Then this slurry was dried and calcined, and platinum was added to obtain a 1%Pt/CeO₂-ZrO₂/Al₂O₃ washcoated catalyst sample. This catalyst was tested in typical WGS conditions (CO inlet molar concentration of 8 %, $\text{H}_2\text{O}/\text{CO}$ at inlet: 3.75, nitrogen balance, a range of temperature between 200°C and 400°C, a gas hourly space velocity of 5000 h^{-1}) but showed a bad activity. This result was attributed to the strong interaction between Pt and alumina, as detected by the TPR. So, another procedure was followed, in order to avoid this interaction. A washcoat of alumina solely was prepared, followed by deposition of ceria in a way to obtain a monolayer over alumina, and finally the deposition of platinum. This new catalytic washcoated formulation (1%Pt/20%CeO₂/ γ -Al₂O₃) showed better performances than the previous one (at T = 240°C: CO conversion of 73%, while the 1%Pt/CeO₂-ZrO₂/Al₂O₃ washcoated catalyst sample stood at 39%), so it was decided to coat the aluminum foam with the new catalytic phases. The dip coating procedure was used to deposit the alumina washcoat; many steps of coating were done, each of one followed by drying at 120°C for 2 h and calcination at 450°C for 3 h. these steps were repeated until the alumina washcoat

reached the desired loading (40% with respect to the final weight). The same catalyst formulation was also prepared in powder form, and employed as reference. The characterization of the washcoat deposited on aluminum foam revealed a very good adhesion (weight loss of 2% with respect to the initial weight of the washcoat solely) and the SEM images revealed a very good dispersion, both the washcoat and the active species. The WGS tests were made on the prepared structured foam catalyst, which was compared to a powder catalyst with the same chemical formulation. The results showed that the deposition of the catalytic formulation on the structured carrier did not cause any appreciable decrease in the performances of the final system. Moreover, it was observed that the structured catalyst, with respect to the powder one, at the higher temperatures was even more active (in particular, at 250°C the structured reached the equilibrium conversion, while the powder was at a conversion of about 83%). This phenomenon could be explained by considering the high thermal properties of the foam carrier, because the high conduction that is exploited in the catalytic structure ensures that the heat generated locally by the reaction can be partially removed and dispersed through the entire structured bed, while in a conventional powder or pellets catalyst it cannot be removed so easily.

In order to evaluate the influence of the thermal transport properties of the foams on the WGS reaction, a laboratory system able to avoid thermal dispersions was set up, by obtaining a “quasi” adiabatic system. These tests were made in the following conditions: inlet $T = 260$ °C, $P = 1$ atm, CO molar fraction = 8 vol%, H_2O molar fraction = 30 vol%, N_2 balance, $WHSV = 2.4$ $g_{CO}/g_{cat}/h$, linear flow velocity = 18.2 cm/s. A first comparison was made between the conventional powder catalyst and a structured catalyst where the foam had the following properties: relative density = 6-8%; pore density = 40 PPI. The powder catalyst reached a conversion of about 70% with a ΔT of 45°C, while the structured showed a ΔT of 12°C with a conversion of about 90%. This result was made possible because of the presence of the high conductive carrier, which is able to redistribute the heat of reaction by increasing the inlet temperature and decreasing the outlet temperature, also obtaining a kinetically more efficient catalyst.

Once the “quasi” adiabatic system was developed, a new set of experimental tests was programmed (with the same operative conditions as above), in which the influence of the foams parameters (relative density and pore density) was evaluated. The results of these experiments showed that an increase in foam density caused better performances. In fact, by using a 40 PPI foam with relative density equal to 10-12%, the structured catalyst allowed to reach a ΔT of 5°C and almost an equilibrium conversion. Moreover, the effect of pore density was also evaluated, by testing three different structured catalysts: 40, 20 and 10 PPI. These three catalysts showed sensibly different performances. The most active foam was the 10 PPI (equilibrium conversion and a ΔT of 4°C ($T_{in} = 279$ °C; $T_{out} = 283$ °C);

Chapter IX

the 40 PPI showed a ΔT of about 6.5°C ($T_{\text{in}} = 277.5^{\circ}\text{C}$; $T_{\text{out}} = 284^{\circ}\text{C}$) and a CO conversion of 98%; the 20 PPI stood at a CO conversion of about 95%, with a ΔT of more than 10°C ($T_{\text{in}} = 274^{\circ}\text{C}$; $T_{\text{out}} = 284.5^{\circ}\text{C}$). Since the three samples had the same amount of solid, this result can seem a bit surprising. But, it has to be considered how the metallic fibers are inter-connected one to each other. In fact, by considering a geometric model found in the literature, it was possible to estimate the thermal conductivity of these three foams. The values found for them reflected the WGS performances, revealing that it is very important to use a foam with a low t/R ratio (where t is the fiber thickness and R is the radius of the lumping of solid material at the intersection of two or more fibers).

At the end of the PhD project an adiabatic reactor model was developed with the aid of the software COMSOL Multiphysics, with the aim of validating the experimental results obtained with the “quasi” adiabatic system. The comparison between the structured foam catalyst and the catalyst in powder form revealed that with the use of a structured catalyst with high thermal conductivity it is possible to reduce greatly the adiabatic ΔT , and increase the CO conversion with respect to a conventional packed bed.

The use of COMSOL allowed to simulate the packed bed adiabatic reactor and the structured foam catalyst, in order to exploit the high thermal properties of the latter in view of an intensification of the Water Gas Shift process. This model has been configured as a basis for the design of a reactor, in order to make the new technology of the structured foam catalyst applicable for the industrial process of the Water Gas Shift.

References

- Ahniyaz A., W. T. Y. M., 2005. Tetragonal Nanocrystals from the $Zr_{0.5}Ce_{0.5}O_2$ Solid Solution by Hydrothermal Method. *The Journal of Physical Chemistry B*, Volume 109, pp. 6136-6139.
- Andreeva D., I. I., 2007. Nanosized gold catalysts supported on ceria and ceria-alumina for WGS reaction: Influence of the preparation method. *Applied Catalysis A: General*, Volume 333, pp. 153-160.
- Azzam K.G., B. I., 2007. A bifunctional catalyst for the single-stage water-gas shift reaction in fuel cell applications. Part 2. Roles of the support and promoter on catalyst activity and stability. *Journal of Catalysis*, Volume 251, pp. 163-171.
- Azzam K.G., B. I. S. K. L. L., 2008. Single stage water gas shift conversion over Pt/TiO₂—Problem of catalyst deactivation. *Applied Catalysis A: General*, Volume 338, pp. 66-71.
- Balat M., 2008. Potential importance of hydrogen as a future solution to environmental and transportation problems. *International Journal of Hydrogen Energy*, Volume 33, pp. 4013-4029.
- Banhart J., 2001. Manufacture, characterisation and application of cellular metals and metal foams. *Progress in Materials Science*, Volume 46, pp. 559-632.
- Bao Z., D. W., 2012. Effect of Fe/Cu ratio on the activity of Fe/Al/Cu catalysts for water gas shift reaction under hydrogen-rich atmosphere. *International journal of hydrogen energy*, Volume 37, pp. 951-955.
- Barreto L., M. A. R. K., 2003. The hydrogen economy in the 21st century: a sustainable development scenario. *International Journal Hydrogen Energy*, Volume 28, pp. 267-268.
- Bartolomew C.H., F. R., 2006. Fundamentals of Industrial Catalytic Processes. In: s.l.:s.n., p. 909.
- Basinska A., M. T., 2006. Catalytic activity in water gas shift reaction of platinum group metals supported on iron oxides. *Reaction Kinetic and Catalysis*, 89(2), pp. 319-324.
- Bhattacharya A., C. V. M. R., 2002. Thermophysical properties of high porosity metal foams. *International Journal of Heat and Mass Transfer*, Volume 45, pp. 1017-1031.

References

- Boaro M., V. M., 2009. A comparative study of water gas shift reaction over gold and platinum supported on ZrO₂ and CeO₂-ZrO₂. *Applied Catalysis B: Environmental*, Volume 88, pp. 272-282.
- Boukha Z., A. J. L. I.-G. A. P.-A. B. G.-O. M. A. G.-V. J. R., 2014. Preparation and characterisation of CuO/Al₂O₃ films deposited onto stainless steel microgrids for CO oxidation. *Applied Catalysis B: Environmental*, Volume 160-161, pp. 629-640.
- Brogan M. S., D. T. J. C. J. A., 1994. Raman spectroscopic study of the Pt-CeO₂ interaction in the Pt/Al₂O₃-CeO₂ catalyst. *Journal of the Chemical Society*, Volume 90, pp. 1461-1466.
- Buitrago R., R.-M. J., 2012. Water gas shift reaction on carbon-supported Pt catalysts promoted by CeO₂. *Catalysis Today*, Volume 180, pp. 19-24.
- Callaghan C.A., 2006. *Kinetics and Catalysis of the Water-Gas-Shift Reaction: A Microkinetic and Graph Theoretic Approach*, s.l.: WORCESTER POLYTECHNIC INSTITUTE.
- Chen Z., Y. Y. E. S. S. E. H., 2004. Catalyst Deactivation and Engineering Control for Steam Reforming of Higher Hydrocarbons in a Novel Membrane Reformer. *Chemical Engineering Science*, Volume 59, pp. 1965-1978.
- Cristiani C., G. A. F. P., 2007a. Study of the physico-chemical characteristics and rheological behaviour of boehmite dispersions for dip-coating applications. *Topics in catalysis*, Volume 42-43, pp. 455-459.
- Cristiani C., V. C. G. F. E. G. S. P. F. P., 2009b. Towards the rationalization of the washcoating process conditions. *Catalysis today*, Volume 147, pp. S24-S29.
- de la Osa A.R., D. L. A., 2012. High pressure Water Gas Shift performance over a commercial non-sulfide CoMo catalyst using industrial coal-derived syngas. *Fuel*, Volume 97, pp. 428-434.
- de la Piscina P.R., H. N., 2008. Use of biofuels to produce hydrogen. *Chemical Society Reviews*, Volume 37, pp. 2459-2467.
- Dimas Rivera G.L., R. d. I. R. J. L. O. C., 2014. Desorption of furfural from bimetallic PTFE oxides/alumina catalysts. *Materials*, Volume 7, p. 527.
- Dupuis A.C., 2011. • Proton exchange membranes for fuel cells operated at medium temperatures: Materials and experimental techniques. *Progress in Materials Science*, Volume 56, pp. 289-327.
- EU Commission, 2003. *Hydrogen energy and fuel cells*, s.l.: EUR 20719 EN Special report.
- Fatehi M., K. M., 1994. Adiabatic reverse combustion in a packed bed. *Combustion and flame*, Volume 99, pp. 1-17.
- Fu Q., K. S., 2003. Gold-ceria catalysts for low-temperature water-gas shift reaction. *Chemical Engineering Journal*, Volume 93, pp. 41-53.
- Galletti C., 2009. Gold-Supported Catalysts for Medium Temperature-Water Gas Shift Reaction. *Topics in Catalysis*, Volume 52, pp. 688-692.

- Ghenciu A.F., 2002. Review of fuel processing catalysts for hydrogen production in PEM fuel cell system. *Current Opinion in Solid State & Materials*, Volume 6, pp. 389-395.
- González Carlos A., A. A. N. M. d. C. C. M. M. A. F.-Z. G., 2007. Pd/TiO₂ washcoated cordierite minimonoliths for hydrodechlorination of light organochlorinated compounds. *Industrial & Engineering Chemical Research*, Volume 46, pp. 7961-7969.
- González-Velasco J. R., G.-O. M. A. M. J. L. B. J. A. G.-M. M. P. a. B. G., 2003. Pt/Ce_{0.68}Zr_{0.32}O₂ Washcoated Monoliths for Automotive Emission Control. *Industrial & Engineering Chemistry Research*, Volume 42, pp. 311-317.
- Groppi G., G. L. T. E., 2007. Generalized Correlation for Gas/Solid Mass-Transfer Coefficients in Metallic and. *Ceramic Foams Industrial & Engineering Chemistry Research*, Volume 46, pp. 3955-3958.
- Hilaire S., W. X., 2004. A comparative study of water-gas-shift reaction over ceria-supported metallic catalysts. *Applied Catalysis A: General*, Volume 258, pp. 271-276.
- Hwang K.-R., P. J.-S., 2011. Si-modified Pt/CeO₂ catalyst for a single-stage water-gas shift reaction. *International journal of hydrogen energy*, Volume 36, pp. 9685-9693.
- Iida H., K. K., 2003. Effect of Pt precursors on catalytic activity of Pt/TiO₂ (rutile) for water gas shift reaction at low-temperature. *Catalysis Communications*, Volume 7, pp. 240-244.
- Institution Smithsonian, 2008. *Fuel Cell Basics*. [Online] Available at: <http://americanhistory.si.edu/fuelcells/basics.htm>
- Jacobs G., G. U. C. E. P. P. D. A. D. B., 2005a. Low-temperature water-gas-shift: impact of Pt promoter loading on the partial reduction of ceria and consequences for catalyst design. *Journal of catalysis*, Volume 229, pp. 499-512.
- Jacobs G., R. S. G. U. M. P. P. M. D. B. H., 2005b. Low temperature water gas shift: Type and loading of metal impacts forward decomposition of pseudo-stabilized formate over metal/ceria catalysts. *Catalysis Today*, Volume 106(1-4), pp. 259-264.
- Kalamaras C. M., P. P., 2009. Kinetic and mechanistic studies of the water-gas shift reaction on Pt/TiO₂ catalyst. *Journal of Catalysis*, Volume 264, pp. 117-129.
- Kam R., S. J., 2010. Pyrophoricity and stability of copper and platinum based water-gas shift catalysts during oxidative shut-down/start-up operation. *Chemical Engineering Science*, Volume 65, p. 6461-6470.
- Kapdan I.K., K. F., 2006. Bio-hydrogen production from waste materials. *Enzyme Microbial Technology*, Volume 38, pp. 569-573.
- Knapp R., W. S. A., 2010. Water-gas shift catalysts based on ionic liquid mediated supported Cu nanoparticles. *Journal of Catalysis*, Volume 276, pp. 280-291.

References

- Konieczny A., M. K. W. T. D. P., 2008. Catalyst development for thermocatalytic decomposition of methane to hydrogen. *International Journal of Hydrogen Energy*, Volume 33, p. 264.
- Kotay S. M., D. D., 2008. Biohydrogen as a renewable energy resource—Prospects and potentials. *International Journal of Hydrogen Energy*, Volume 33, p. 258 – 263..
- Levin D.B., P. L. L. M., 2004. Biohydrogen production: prospects and limitations to practical application. *International Journal of Hydrogen Energy*, Volume 29, pp. 173-185.
- Leyda B., 2000. *Personal communications*, s.l.: ERG Aerospace.
- Li Y., F. Q., 2000. Low-temperature water-gas shift reaction over Cu- and Ni-loaded cerium oxide catalysts. *Applied Catalysis B: Environmental*, Volume 27, pp. 179-191.
- Li Y., F. Q. F.-S. M., 2000. Low-temperature water-gas shift reaction over Cu- and Ni-loaded cerium oxide catalysts. *Applied Catalysis B: Environmental*, Volume 27, pp. 179-191.
- Liang H., Z. Y., 2009. Ceria modified three-dimensionally ordered macroporous Pt/TiO₂ catalysts for water-gas shift reaction. *Journal of rare earths*, Volume 27, pp. 425-430.
- Lim S., B. J., 2009. Study of activity and effectiveness factor of noble metal catalysts for water–gas shift reaction. *International journal of hydrogen energy*, Volume 34, pp. 870-876.
- Lin J.-H., B. P., 2010. Hydrogen production by water–gas shift reaction over bimetallic Cu–Ni catalysts supported on La-doped mesoporous ceria. *Applied Catalysis A: General*, Volume 387, pp. 87-94.
- Lin W., H. A. K. C. W. I., 2008. Probing Metal-Support Interactions under Oxidizing and Reducing Conditions: In Situ Raman and Infrared Spectroscopic and Scanning Transmission Electron Microscopic-X-ray Energy-Dispersive Spectroscopic Investigation of Supported Platinum Catalysts. *The Journal of Physical Chemistry C*, Volume 112, pp. 5942-5951.
- Lua T.J., S. H. A. M., 1998. Heat transfer in open-cell metal foams. *Acta Materialia*, Volume 46, pp. 3616-3635.
- Luengnaruemitchai A., O. S., 2003. Comparative studies of low-temperature water–gas shift reaction over Pt/CeO₂, Au/CeO₂, and Au/Fe₂O₃ catalysts. *Catalysis Communications*, Volume 4, pp. 215-221.
- Luengnaruemitchai A., O. S. G. E., 2003. Comparative studies of low-temperature water-gas shift reaction over Pt/CeO₂, Au/CeO₂ and Au/Fe₂O₃ catalysts. *Catalysis communications*, Volume 4, pp. 215-221.
- McBride J.R., G. G. P. C. W. W., 1991. Growth and characterization of reactively sputtered thin-film platinum oxides. *Journal of Applied Physics*, Volume 69, pp. 1596-1604.

- Moharana M.K., P. N. K. S. K. D., 2011. Distributed hydrogen production from ethanol in a microfuel processor: Issues and challenges. *Renewable and Sustainable Energy Reviews*, Volume 15, p. 524– 533.
- Montebelli A., V. C. G. G. T. E. K. S. V. H. J. M. R., 2014. Washcoating and chemical testing of a commercial Cu/ZnO/Al₂O₃ catalyst for the methanol synthesis over copper open-cell foams. *Applied Catalysis A: General*, Volume 481, pp. 96-103.
- Murrell L.L., T. S. A. D., 1993. Laser Raman Characterization of Surface Phase Precious Metal Oxides Formed on CeO₂ Micro Domains Generated Within an Alumina Host by Sol Synthesis. *Studies in Surface Science and Catalysis*, Volume 75, pp. 681-690.
- Navarro R.M., P. M. F. J., 2007. Hydrogen Production Reactions from Carbon Feedstocks: Fossil Fuels and Biomass. *Chem. Rev*, Volume 107, pp. 3952-3956.
- Newsome D. S., 1980. The Water-Gas Shift Reaction. *Catalysis Reviews: Science and Engineering*, Volume 21 (2), pp. 275-318.
- Ni M., L. D. L., 2007. A review on reforming bio-ethanol for hydrogen production. *International Journal of Hydrogen Energy*, Volume 32, pp. 3238-3247.
- Palma V., P. E. C. P., 2009. Structured catalytic substrates with radial configurations for the intensification of the WGS stage in H₂ production. *Catalysis Today*, Volume 147, pp. 107-112.
- Panagiotopoulou P., C. A., 2006. Particle size effects on the reducibility of titanium dioxide and its relation to the water-gas shift activity of Pt/TiO₂ catalysts. *Journal of Catalysis*, Volume 240, pp. 114-125.
- Panagiotopoulou P., K. D., 2006. Effect of the nature of the support on the catalytic performance of noble metal catalysts for the water–gas shift reaction. *Catalysis Today*, Volume 112, pp. 49-52.
- Petkovich N. D., R. S. G., 2011. Control of Heterogeneity in Nanostructured Ce_{1-x}Zr_xO₂ Binary Oxides for Enhanced Thermal Stability and Water Splitting Activity. *Journal of Physical Chemistry C*, Volume 115, p. 21022–21033.
- Petrini G., M. F. B. A. a. G. F., 1983. *Preparation and Characterization of Very Active Cu/ZnO and Cu/ZnO/Al₂O₃ LTS Catalysts Using a Single Phase Cu-Zn Precursor Compound*. Amsterdam: Elsevier.
- Pigos J. M., B. C. J., 2007. Low temperature water-gas shift: Characterization of Pt-based ZrO₂ catalyst promoted with Na discovered by combinatorial methods. *Applied Catalysis A: General*, Volume 319, pp. 47-57.
- Pouransani N., M. M. S. G. M. F., 2014. *A general methodology for energy efficiency of industrial chemical processes*. 8th International Conferences on Foundation of Computer-Aided Process Design FOCAD , s.n.
- Reay D., R. C. H. A., 2008. *Process Intensification. Engineering for Efficiency: Sustainability and Flexibility*. s.l.: Elsevier.

References

- Reina T. R., M. A. Á. I. S. A. O. J. A. C. M., 2012. Influence of Vanadium or Cobalt Oxides on the CO Oxidation Behavior of Au/MO_x/CeO₂-Al₂O₃ Systems. *ChemCatChem*, Volume 4, pp. 512-520.
- Ricote S., J. G., 2006. Low temperature water-gas shift: Characterization and testing of binary mixed oxides of ceria and zirconia promoted with Pt. *Applied catalysis A: General*, Volume 303, pp. 35-47.
- Sato Y., T. K., 2006. Marked addition effect of Re upon the water gas shift reaction over TiO₂ supported Pt, Pd and Ir catalysts,. *Catalysis Communications* , Volume 7, pp. 91-95.
- She Y., L. L., 2009. Effect of yttrium addition on water-gas shift reaction over CuO/CeO₂ catalysts. *Journal of rare earths*, 27(3), pp. 411-415.
- Sun J., Q. X., 2004. Hydrogen from steam reforming of ethanol in low and middle temperature range for fuel cell application. *International Journal of Hydrogen Energy*, Volume 29, pp. 1075-1081.
- Tabakova T., I. V., 2000. Influence of the microscopic properties of the support on the catalytic activity of Au/ZnO, Au/ZrO₂, Au/Fe₂O₃, Au/Fe₂O₃-ZnO, Au/Fe₂O₃-ZrO₂ catalysts for the WGS reaction. *Applied Catalysis A: General* , Volume 202, pp. 91-97.
- Thompson C.R., M. P. F. O. S., 2013. Evaluation of the use of ceramic foams as catalyst supports for reverse-flow combustors. *Chemical Engineering Journal*, Volume 221, pp. 44-54.
- Uchida H., I. N. O. M. H. T., 1967. The zinc oxide-copper catalyst for carbon monoxide shift conversion.I. The dependency of the catalyst activity on the chemical composition of the catalyst. *Bulletin of the Chemical Society of Japan*, Volume 40, pp. 1981-1986.
- Vaidya D., R. E., 2006. Insight into steam reforming of ethanol to produce hydrogen for fuel cells. *Chemical Engineering Journal*, Volume 117, pp. 39-49.
- Vasilchenko D., T. S. B. I. K. S., 2013. Speciation of Platinum(IV) in Nitric acid solutions. *Inorganic Chemistry*, Volume 52, pp. 10532-10541.
- Wang Y., Z. Y., 2012. Silica-encapsulated platinum catalysts for the low-temperature water-gas shift reaction. *Applied Catalysis B: Environmental* , Volume 127, pp. 342-350.
- Wu Z., L. M. H. J. M. I. H. O. S., 2010. Probing defect sites on CeO₂ nanocrystals with well-defined surface planes by Raman spectroscopy and O₂ adsorption. *Langmuir*, Volume 26, p. 16595.
- Xu W., S. R., 2012. In situ studies of CeO₂-supported Pt, Ru, and Pt-Ru alloy catalysts for the water-gas shift reaction: Active phases and reaction intermediates. *Journal of Catalysis*, Volume 219, p. 117-126.
- Yao H.C., Y. Y., 1984. Ceria in automotive exhaust catalysts. I. Oxygen storage. *Journal of Catalysis*, Volume 86, pp. 254-265.
- Zhang Y., Z. G., 2012. Ce-K-promoted Co-Mo/Al₂O₃ catalysts for the water gas shift reaction. *International journal of hydrogen energy*, Volume 37, pp. 6363-6371.

